

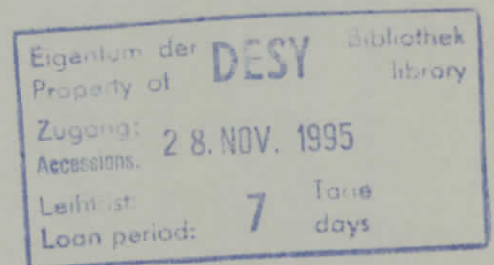
Internal Report
DESY F35D-95-11

November 1995

Study of the Photon Remnant in Resolved Photoproduction at HERA

by

B. H. Behrens



DESY behält sich alle Rechte für den Fall der Schutzrechtserteilung und für die wirtschaftliche Verwertung der in diesem Bericht enthaltenen Informationen vor.

DESY reserves all rights for commercial use of information included in this report, especially in case of filing application for or grant of patents.

**"Die Verantwortung für den Inhalt dieses
Internen Berichtes liegt ausschließlich beim Verfasser"**

STUDY OF THE PHOTON REMNANT IN RESOLVED
PHOTOPRODUCTION AT HERA

by ✓
BRUCE H. BEHRENS

A dissertation submitted in partial fulfillment of the
requirements for the degree of

Doctor of Philosophy
(Physics)

at the
UNIVERSITY OF WISCONSIN — MADISON
1995

Acknowledgements

I would like to thank:

- My advisors, Wesley Smith and Don Reeder for their help and support over the years.
- Rosario Nania, for encouraging this study, asking hard questions and pointing me toward the answers.
- Yuji Yamazaki, for checking my results and contributing his own.
- Katsuo Tokushuku and Jim Whitmore, for their significant contributions to this work, including editing the paper and ZEU'S note.
- Costas Foudas, for his friendship and instruction during my years with Wisconsin, and for the many discussions we had about this work.
- Carrie Fordham, for her advice, friendship and instruction.
- The members of the hard photoproduction group, including: P. Bussey, J. Butterworth, C. Coldewey, G. D'Agostini, K. Desch, G. Feild, L. Feld, C. Glasman, A. Levy, S. Nam, L. Sinclair, J. Terron for their help and advice.
- All members of the ZEU'S Collaboration for collecting the data upon which this dissertation is based, and for their interest in and advice on this subject.

- The DESY directorate for their strong support and encouragement.
- The HERA machine group for their remarkable achievements, which were essential for the successful completion of this work.
- The DESY computing and network services for their support.

To my mother, Abba,
and my wife, Nicole.

Abstract

Photoproduction at HERA is studied in ep collisions, using the ZEUS detector, for γp center-of-mass energies ranging from 130–270 GeV. A sample of events with two high- p_T jets ($p_T > 6$ GeV, $|\eta| < 1.6$) and a third cluster in the approximate direction of the electron beam is isolated using a clustering algorithm. These events are mostly due to resolved photoproduction. The third cluster is identified as the photon remnant. Its properties, such as the transverse and longitudinal energy flows around the axis of the cluster, are consistent with those commonly attributed to jets, and in particular with those found for the other two jets in these events. The mean value of the photon remnant p_T with respect to the beam axis, measured to be 2.1 ± 0.2 GeV, is substantial.¹

Contents

Acknowledgements	i
Abstract	iv
1 Introduction	1
1.1 Photoproduction	5
1.2 Direct and Resolved Photoproduction	7
1.3 The Photon Remnant	11
2 Experiment	14
2.1 HERA	14
2.2 The ZEUS Detector	17
2.2.1 Calorimeter	17
2.2.2 Central Tracking	25
2.2.3 Luminosity Monitor	26
2.2.4 Veto Wall	28
2.2.5 C5 VETO Counter	29
2.2.6 Experiment Trigger	30
3 Monte Carlo Simulations	34
3.1 Overview	35
3.2 PYTHIA	35

3.3	HERWIG	36
3.4	Detector Simulation	37
3.5	The Resolved Photon	38
4	Event Selection	40
4.1	Trigger	40
4.2	Off-line Data Selection	43
4.3	Jet Finding with the k_{\perp} Algorithm	45
4.4	Identification of the Photon Remnant	47
4.5	Direct and Resolved Separation	52
4.6	Comparison of the k_{\perp} and cone algorithms	55
4.6.1	The Cone Algorithm	55
4.6.2	Algorithm Comparison	56
5	Data Corrections	60
5.1	Hadron Level Kinematic Region	60
5.2	Matching	61
5.3	Measurement Resolutions	62
5.4	Data Corrections	66
5.4.1	Bin-By- Bin Corrections	68
5.4.2	Bayes' Unfolding	68
5.4.3	Simultaneous Corrections in Two Variables	69
6	Measurement Uncertainties	74
6.1	Statistical Errors	71
6.1.1	Corrections in One Variable	75

6.1.2	Corrections in Two Variables	76
6.2	Independent Confirmation	79
6.3	Systematic Uncertainties	82
6.4	Islands and Cells	85
6.5	Noise Suppression	91
6.6	Inactive Material	91
6.7	Y_{cut} studies	98
7	Photon Remnant Properties	106
7.1	External Attributes	106
7.1.1	Comparison with PYTHIA	107
7.1.2	Comparison with High- k_{\perp} PYTHIA	109
7.2	Internal Attributes	112
7.2.1	Structure of High- p_T Jets	114
7.2.2	Comparison with High- p_T Jets	116
7.2.3	Comparison with PYTHIA	118
7.3	Independent Confirmation	120
8	Conclusions	125
A	Variable Resolutions	127
A.1	PYTHIA	127
A.2	HERWIG	151
	References	

List of Figures

1.1	(a) Fluctuation of the photon into a quark antiquark pair. (b) Electron-proton deep inelastic scattering.	2
1.2	Examples of diagrams for (a) direct, (b) resolved and (c) anomalous hard photoproduction interactions.	9
1.3	(a) Incoming electron and proton in the HERA lab frame. (b) The direct event structure after an ep collision. (c) The resolved/anomalous event structure after an ep collision.	10
2.1	Orientation of the HERA ep collider.	15
2.2	Cut-away view of the ZEUS detector.	18
2.3	A cross sectional view of the ZEUS calorimeter is shown, divided into hadronic and electromagnetic cells.	19
2.4	View of a typical calorimeter trigger tower.	24
2.5	Semi-projective trigger tower arrangement.	24
2.6	Layout of the ZEUS luminosity monitor.	27
2.7	Diagram of the ZEUS three level trigger and data acquisition system.	31
4.1	Pseudorapidity distributions of clusters for the inclusive photoproduction sample.	49
4.2	Pseudorapidity distribution of the lowest $p_T^{\gamma^d}$ cluster.	51

4.3	Monte Carlo x_{γ}^{cone} distribution for direct and resolved photoproduction events.	53
4.4	Effect of the selection criteria on the x_{γ}^{cone} distribution.	54
4.5	Comparison between quantities found using the k_{\perp} and cone algorithms. (a) Pseudorapidity comparison, (b) cluster transverse energy ratio, (c) x_{γ} comparison, and (d) RCAL energy.	57
5.1	Percent hadronic energy observed, excluding particles in the angular region of the beam pipe (circles), and percent energy observed in the simulated calorimeter (triangles) as a function of E_3 , the photon remnant energy at the hadron level.	65
5.2	Energy resolution of the photon remnant as determined using the PYTHIA Monte Carlo simulation.	67
5.3	Illustration of the data correction method.	71
5.4	Illustration of the data correction method.	72
6.1	Relative size of the statistical uncertainty for the six E_{γ} bins as a function of the number of corrected distributions used in their determination.	77
6.2	Example of a calculation of the error on the mean for a distribution.	79
6.3	Comparison between Analysis A and Analysis B the uncorrected pseudorapidity distributions.	81
6.4	Percent systematic fluctuations in measurements of (a) p_{T3} , (b) η_3 and (c) E_3	83
6.5	Systematic uncertainties in the $\langle E_{\gamma} \rangle$ distribution.	86

6.6	Systematic uncertainties in the $\Sigma_i E_{i\perp}$ and $\Sigma_i E_{i\perp}^2$ distributions.	87
6.7	Systematic errors on the energy flow for (a) clusters 1 and 2 and (b) cluster 3.	88
6.8	Number of particles per island as a function of pseudorapidity.	89
6.9	Number of calorimeter islands in the lowest p_T^{cal} cluster as a function of the number of calorimeter cells.	90
6.10	Number of calorimeter islands (a) and calorimeter cells (b) in the lowest p_T^{cal} cluster as a function of the cluster energy for both the data and the Monte Carlo simulation.	91
6.11	Calorimeter cell energies before and after applying the noise suppression algorithm.	93
6.12	Comparison between the (uncorrected) data and the PYTHIA Monte Carlo simulation when the Monte Carlo cell energies within a 10° cone in the rear direction are reduced by 0, 10 and 100%.	97
6.13	Comparison between the (uncorrected) data and the PYTHIA Monte Carlo simulation when the cell energies within a 10° cone in the rear direction are reduced by 0 and 100% in both the data and the Monte Carlo simulation.	99
6.14	Comparison between the Y_{cut} distributions for different definitions of resolved and direct events.	101
6.15	Influencer on the results of using a fixed value of Y_{cut}	103
7.1	External attributes of the photon remnant. The data are corrected to the hadron level.	108

7.2	Intrinsic transverse momentum parameterizations for the conventional PYTHIA (solid line), PYTHIA High k_t A (dashed line), and PYTHIA High k_t B (dotted line).	110
7.3	Comparison between the data and two different High k_t Monte Carlo parameterizations.	111
7.4	Effect of the High k_t reweighting on the two high- p_T jets.	113
7.5	Internal attributes of high- p_T jets.	115
7.6	Comparison between the internal attributes of the photon remnant (cluster 3) and the two high- p_T jets (cluster 1,2).	117
7.7	Internal attributes of the photon remnant compared with the hadron level Monte Carlo expectations.	119
7.8	Comparison between the external attributes of the photon remnant as found by Analysis A and Analysis B, for the corrected data and for the hadron level Monte Carlo simulation.	121
7.9	Comparison between the (corrected) internal attributes of the photon remnant for Analysis A and Analysis B.	122
7.10	Comparison between Analysis A ((a) and (c)) and Analysis B ((b) and (d)). The corrected mean value of $\langle E_{i\perp}^2 \rangle$ as a function of the cluster energy for the photon remnant and for the two high- p_T jets as determined by Analysis A (a) and Analysis B (b). The corrected mean value of $\Sigma_i E_{i\perp}$ and $\Sigma_i E_{i\perp}^2$ as a function of the cluster energy for the photon remnant and for the two high- p_T jets as determined by Analysis A (c) and Analysis B (d).	123

7.11 Comparison between the corrected energy flow around the cluster axis of the photon remnant and the two high- p_T jets as measured by (a) Analysis A and (b) Analysis B.	121
A.1 Pseudorapidity resolution of the highest p_T cluster as determined using the PYTHIA Monte Carlo simulation.	130
A.2 Pseudorapidity resolution of the second highest p_T cluster as determined using the PYTHIA Monte Carlo simulation.	131
A.3 Pseudorapidity resolution of the photon remnant as determined using the PYTHIA Monte Carlo simulation.	132
A.4 Transverse momentum resolution of the highest p_T cluster as determined using the PYTHIA Monte Carlo simulation.	133
A.5 Transverse momentum resolution of the second highest p_T cluster as determined using the PYTHIA Monte Carlo simulation.	134
A.6 Transverse momentum resolution of the photon remnant as determined using the PYTHIA Monte Carlo simulation.	135
A.7 Energy resolution of the highest p_T cluster as determined using the PYTHIA Monte Carlo simulation.	136
A.8 Energy resolution of the second highest p_T cluster as determined using the PYTHIA Monte Carlo simulation.	137
A.9 The y resolution as determined using the PYTHIA Monte Carlo simulation.	138
A.10 The $\langle E_T^2 \rangle$ resolution (calculated using calorimeter islands) of the highest p_T cluster as determined using the PYTHIA Monte Carlo simulation.	139

A.11 The $\langle E_T^2 \rangle$ resolution (calculated using calorimeter islands) of the second highest p_T cluster determined using the PYTHIA Monte Carlo simulation.	140
A.12 The $\langle E_T^2 \rangle$ resolution (calculated using calorimeter islands) of the photon remnant as determined using the PYTHIA Monte Carlo simulation.	141
A.13 The $\langle E_T^2 \rangle$ resolution (calculated using calorimeter cells) of the highest p_T cluster determined using the PYTHIA Monte Carlo simulation.	142
A.14 The $\langle E_T^2 \rangle$ resolution (calculated using calorimeter cells) of the second highest p_T cluster determined using the PYTHIA Monte Carlo simulation.	143
A.15 The $\langle E_T^2 \rangle$ resolution (calculated using calorimeter cells) of the photon remnant as determined using the PYTHIA Monte Carlo simulation.	144
A.16 The $\Sigma_i E_T^2$ resolution of the highest p_T cluster as determined using the PYTHIA Monte Carlo simulation.	145
A.17 The $\Sigma_i E_T^2$ resolution of the second highest p_T cluster as determined using the PYTHIA Monte Carlo simulation.	146
A.18 The $\Sigma_i E_T^2$ resolution of the photon remnant as determined using the PYTHIA Monte Carlo simulation.	147
A.19 The $\Sigma_i E_L^2$ resolution of the highest p_T cluster as determined using the PYTHIA Monte Carlo simulation.	148
A.20 The $\Sigma_i E_L^2$ resolution of the second highest p_T cluster as determined using the PYTHIA Monte Carlo simulation.	149

A.21	The $\Sigma_i E_L^i$ resolution of the photon remnant as determined using the PYTHIA Monte Carlo simulation.	150
A.22	Pseudorapidity resolution of the highest p_T cluster as determined using the HERWIG Monte Carlo simulation.	153
A.23	Pseudorapidity resolution of the second highest p_T cluster as determined using the HERWIG Monte Carlo simulation.	154
A.24	Pseudorapidity resolution of the photon remnant as determined using the HERWIG Monte Carlo simulation.	155
A.25	Transverse momentum resolution of the highest p_T cluster as determined using the HERWIG Monte Carlo simulation.	156
A.26	Transverse momentum resolution of the second highest p_T cluster as determined using the HERWIG Monte Carlo simulation.	157
A.27	Transverse momentum resolution of the photon remnant as determined using the HERWIG Monte Carlo simulation.	158
A.28	Energy resolution of the highest p_T cluster as determined using the HERWIG Monte Carlo simulation.	159
A.29	Energy resolution of the second highest p_T cluster as determined using the HERWIG Monte Carlo simulation.	160
A.30	Energy resolution of the photon remnant as determined using the HERWIG Monte Carlo simulation.	161
A.31	The y resolution as determined using the HERWIG Monte Carlo simulation.	162
A.32	The $\langle E_T^i \rangle$ resolution (calculated using calorimeter islands) of the highest p_T cluster as determined using the HERWIG Monte Carlo simulation.	163

A.33	The $\langle E_T^i \rangle$ resolution (calculated using calorimeter islands) of the second highest p_T cluster as determined using the HERWIG Monte Carlo simulation.	164
A.34	The $\langle E_T^i \rangle$ resolution (calculated using calorimeter islands) of the photon remnant as determined using the HERWIG Monte Carlo simulation.	165
A.35	The $\langle E_T^i \rangle$ resolution (calculated using calorimeter cells) of the highest p_T cluster as determined using the HERWIG Monte Carlo simulation.	166
A.36	The $\langle E_T^i \rangle$ resolution (calculated using calorimeter cells) of the second highest p_T cluster as determined using the HERWIG Monte Carlo simulation.	167
A.37	The $\langle E_T^i \rangle$ resolution (calculated using calorimeter cells) of the photon remnant as determined using the HERWIG Monte Carlo simulation.	168
A.38	The $\Sigma_i E_T^i$ resolution of the highest p_T cluster as determined using the HERWIG Monte Carlo simulation.	169
A.39	The $\Sigma_i E_T^i$ resolution of the second highest p_T cluster as determined using the HERWIG Monte Carlo simulation.	170
A.40	The $\Sigma_i E_T^i$ resolution of the photon remnant as determined using the HERWIG Monte Carlo simulation.	171
A.41	The $\Sigma_i E_L^i$ resolution of the highest p_T cluster as determined using the HERWIG Monte Carlo simulation.	172
A.42	The $\Sigma_i E_L^i$ resolution of the second highest p_T cluster as determined using the HERWIG Monte Carlo simulation.	173

A.43 The $\Sigma_4 E_L^2$ resolution of the photon remnant as determined using the HERWIG Monte Carlo simulation.	171
--	-----

List of Tables

1.1 List of the direct, resolved and anomalous subprocesses which occur in hard photoproduction.	7
2.1 Comparison between some HERA design parameters and what was actually achieved in 1993.	16
4.1 Comparison of the number of events accepted and rejected when cuts are applied to the quantities found by the cone and k_T al- gorithms.	59
5.1 Resolution measurements for various experimentally measured quantities.	63
6.1 Example values used in calculating the error on the mean.	78
6.2 List of systematic checks included in the calculation of the sys- tematic error bars in figures 6.4 through 6.7.	84

Chapter 1

Introduction

High Energy Physics is the study of the smallest constituents of matter, and the forces by which they interact. There are three fundamental forces in nature: gravity, the strong nuclear force; and the electroweak force. Each of these forces is mediated by one or more particles: the as yet unseen graviton for gravity, gluons (g) for the strong nuclear force, and the photon (γ), W and Z bosons for the electroweak force. This dissertation is a study of the photon.

The theory which describes the interactions of the photon, as well as those of the W and Z bosons, is called quantum electrodynamics (QED). QED is arguably the most successful physics theory ever invented. It has been tested and verified over an energy range of more than 18 orders of magnitude. The extreme accuracy of QED might lead one to believe that the photon is completely understood. However, this is not the case. There are still questions about the photon which have not been answered. These questions are related to the photon's "structure".

As far as is known, the photon is truly an elementary particle, with no internal structure or extended physical size. However, since the photon couples to charged elementary particles like quarks (q) and their antiparticles, antiquarks (\bar{q}), it can briefly fluctuate into a quark-antiquark pair (Fig. 1.1a).

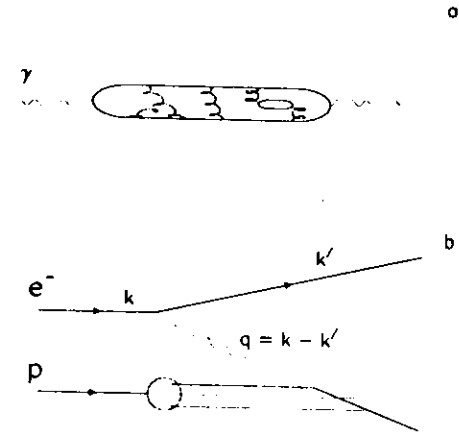


Figure 1.1: (a) Fluctuation of the photon into a quark-antiquark pair. (b) Electron-proton deep inelastic scattering. The four-momentum of the incoming electron is k . The four-momentum of the scattered electron is k' . The four-momentum of the exchanged photon is $q = k - k'$.

The quark-antiquark pair can exist for a time

$$\Delta t \leq \frac{\hbar}{\Delta E}, \quad (1.1)$$

where ΔE is the difference between the energy of the incoming photon and the energy (including the quark masses) of the quark-antiquark pair. These quark-antiquark pairs, together with the gluons that they emit, constitute the photon "structure". Quarks, antiquarks and gluons are collectively referred to as partons. Since quarks interact via the strong nuclear force in addition to the electroweak force, the photon can sometimes appear to interact as if it

were a strongly interacting “hadronic” particle.

The theory which describes the strong nuclear force, quantum chromodynamics (QCD), is quite similar to QED. In fact, QCD was developed in analogy with QED. However, there are significant differences which make the observed behavior of the strong nuclear force very different from that of the electroweak force. One difference is that QED has two electric charges (positive and negative), while QCD has three “color” charges (red, green, blue). Another difference is that photons have no electric charge, but gluons are color charged. This difference has a strong impact on the relative values of the strong and electroweak coupling constants, α_s and α_{em} .

The coupling constants, or equivalently the electric and color charges, are not actually constant. Charge screening, causes the measured value of the coupling constants to depend on the distance from which they are measured. Charge screening is caused by the same quantum mechanical processes that produce photon structure. For example, an electron can emit a photon which can then fluctuate into an electron positron pair. Because positive and negative charges attract, while like charges repel, the positron is attracted by the original electron. This results in charge screening. The closer one gets to the original electron the higher its apparent electric charge becomes. Short distances are probed with short wavelengths, which are equivalent to high energies. Therefore, the electromagnetic coupling constant grows as the energy scale at which it is measured increases.

In QCD, however, the effect of the charge screening is reversed. Because gluons carry color charge, a “red” charged quark, for example, becomes surrounded predominantly by gluons which also carry the red color charge. This

enhances the apparent color charge of the quark in QCD. Therefore, the measured value of the strong coupling constant decreases as the energy scale at which it is measured increases. At an energy scale equal to that of the mass of the W boson ($O(80\text{GeV}/c^2)$), $\alpha_s \approx 1/9$, while $\alpha_{em} \approx 1/128$.²

Calculations in QED and QCD are solved using perturbation theory. In perturbation theory, a problem is broken into an infinite sum of terms which can be solved exactly. The terms are grouped according to increasing powers of α_s and α_{em} . Therefore, the first group of terms, with the lowest power of α_s and α_{em} , tends to be the largest. Succeeding terms, with larger powers of α_s and α_{em} are suppressed. A Leading-Order (LO) calculation for a particular process includes only the terms that have the lowest powers of α_s and α_{em} which still describe the process. For example, the LO Feynman diagram for Deep Inelastic Scattering (DIS) of an electron with a proton is shown in Fig. 1.1b. The LO term contains one power of α_{em} for each of the two electromagnetic couplings ($O(\alpha_{em}^2)$); one between the photon and the electron and one between the photon and the quark. By including higher order terms, an answer can be calculated to any specified level of precision. A Next-to-Leading-Order (NLO) calculation for the diagram shown in Fig. 1.1b would include the next most significant term, which in this case would include an added power of α_s ($O(\alpha_{em}^2\alpha_s)$), corresponding to a gluon emitted by the struck quark. Since α_s is larger than α_{em} , particle interactions are much more difficult to calculate in QCD than in QED because the succeeding terms tend to diminish in significance more slowly in QCD than in QED. In fact, at low energies ($O(1\text{ GeV})$) α_s becomes so large that perturbative QCD breaks down completely. Therefore, strong interactions are not as well understood as electroweak interactions.

1.1 Photoproduction

Photoproduction refers to the production of subatomic particles in high energy collisions between photons and other subatomic particles, such as the proton. In this dissertation, hard photoproduction specifically indicates that jets of particles with large transverse energy were created in collisions between high energy photons and protons. The process by which an outgoing parton becomes a jet of particles is called fragmentation.

This dissertation studies the photon in collisions of 26.7 GeV electrons with 820 GeV protons at the HERA collider (see section 2.1). HERA is an excellent place to study photons, because in almost every ep collision the exchanged particle is a virtual photon (γ^*). The photons are called virtual because they violate energy and momentum conservation, as allowed by the Heisenberg Uncertainty Principle within the short time and distance scales probed by the interaction. The positive scalar quantity Q^2 , defined by the equation:

$$Q^2 = -q^2 = -(k - k')^2 > 0, \quad (1.2)$$

equals the momentum transferred from the scattered electron and as such, quantifies the virtuality of the exchanged photon. Here q is the four momentum of the virtual photon, as shown in fig. 1.1b. The quantity

$$k = (E_e, 0, 0, E_e), \quad (1.3)$$

is the four momentum of the incoming electron with energy, $E_e = 26.7$ GeV, and

$$k' = (E_e', 0, E_e' \sin \alpha, E_e' \cos \alpha) \quad (1.1)$$

is the four momentum of the outgoing electron with energy, E_e' , and scattering angle with respect to the electron beam direction, α . Although real photons are massless, virtual photons have an apparent mass,

$$m_{\gamma^*} = \sqrt{Q^2}, \quad (1.5)$$

which is nonzero. The further a particle's apparent mass is from its true mass, the more virtual the particle is. When Q^2 is high, which occurs at HERA when the electron is scattered back in the proton direction, the exchanged photon is said to be highly virtual. Equations 1.2, 1.3 and 1.4 show that when the electron scatters at small angles ($\alpha < 1.0^\circ$), Q^2 is very close to zero ($Q^2 < 0.2$ GeV²). This means that the photon is almost real. At HERA Q^2 can range from 0 to more than 10,000 GeV².

When Q^2 is small and the photon is essentially real, the fact that the photon was actually emitted by an electron can be ignored. In this case the events are called photoproduction events. Since the ep interaction cross section via virtual photon exchange is proportional to $\frac{1}{Q^2}$, photoproduction events are actually the most common type of ep interaction at HERA.

While the center of mass energy of electron-proton collisions at HERA is $\sqrt{s} = 297$ GeV, the center of mass energy of photon-proton collisions, $W_{\gamma p}$, ranges from less than 130 to more than 270 GeV. This is equivalent to a beam of 20 TeV photons striking stationary protons. At these energies, a photon which has fluctuated into a quark-antiquark pair can travel hundreds of proton radii without violating the Heisenberg Uncertainty Principle.

1.2 Direct and Resolved Photoproduction

The fact that the photon can travel significant distances as a hadronic particle enables photoproduction events to be classified into two distinct types; direct and resolved.³ Direct photoproduction occurs when the photon interacts directly with a quark or gluon in the proton. Resolved photoproduction occurs when the photon fluctuates into quarks before it interacts. The resolved and direct photon-proton interactions are described in LO QCD, with two different classes of Feynman diagrams. Figure 1.2a shows one of the two LO diagrams for the direct process. The electron emits a photon and is scattered at a very small angle. The high energy photon then interacts directly with a parton within the proton. The “hard scattering” of these two objects results in two outgoing partons with high transverse energy. In addition, the remaining partons from the proton continue traveling in the proton direction. One example of the eight resolved subprocesses is shown in Fig. 1.2b (Table 1.1 lists all subprocesses for direct, resolved and anomalous photoproduction). In Fig. 1.2b,

Direct	Resolved	Anomalous
$\gamma q \rightarrow qq$	$qq \rightarrow qq$	$\gamma q \rightarrow gq$
$\gamma g \rightarrow q\bar{q}$	$qq \rightarrow qq$	$\gamma q \rightarrow qq$
	$q\bar{q} \rightarrow gg$	$\gamma g \rightarrow q\bar{q}$
	$gg \rightarrow qq$	
	$gg \rightarrow gg$	
	$qq \rightarrow qq$	
	$qq \rightarrow q'q'$	
	$q\bar{q} \rightarrow q\bar{q}$	

Table 1.1: List of the direct, resolved and anomalous subprocesses which occur in hard photoproduction.

the electron also emits a photon and is scattered at a very small angle. In this case, however, the high energy photon fluctuates into a quark antiquark pair before the collision. A parton from the resolved photon interacts with a parton from the proton, resulting in two high transverse energy partons and proton debris, as in the direct process. However, there is one significant difference between the two processes. When a resolved interaction occurs, only a fraction, x_1 , of the original photon’s momentum is involved in the collision. Therefore, for resolved events, $x_1 < 1.0$, while for direct events $x_1 = 1.0$. In resolved events, the remaining photon momentum is carried away by the other parton or partons in the photon. These parton(s) continue traveling in approximately the same direction as the original photon.

The event topology for direct and resolved photoproduction in the HERA lab frame is shown in Fig. 1.3. In direct events, the outgoing partons which result from the hard scattering between the photon and a parton from the proton produce two jets of particles with high transverse momentum. In addition to the two jets, the fragmentation of the remaining partons in the proton forms a proton remnant. In addition, in resolved events, a fourth object, called the photon remnant, forms from the debris of the photon.

The virtuality of the quark antiquark pair from the photon determines whether or not perturbative QCD can be used to describe the interaction. If the virtuality of the quark-antiquark pair is above a threshold, generally taken to be about 1 GeV, then perturbative QCD can be used. However, below this threshold the fluctuation of the photon into quark antiquark pairs cannot be described by perturbative QCD. In this case, the photon is treated as a strongly interacting, hadronic particle and a parton distribution function (PDF) is used

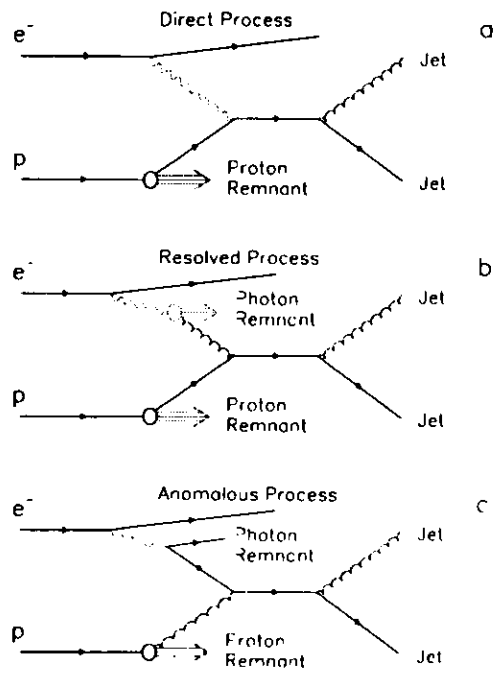


Figure 1.2: Examples of diagrams for (a) direct, (b) resolved and (c) anomalous hard photoproduction interactions.

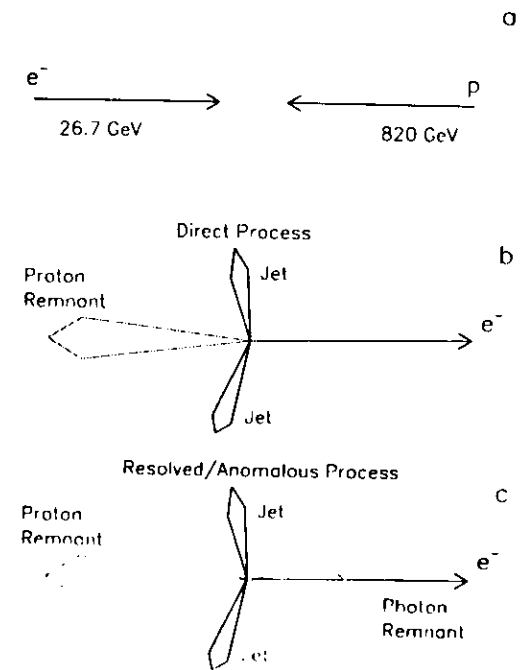


Figure 1.3: (a) Incoming electron and proton in the HERA lab frame. (b) The direct event structure after an ep collision. (c) The resolved/anomalous event structure after an ep collision.

fragmentation of the photon remnant is modeled. In addition, differences between these distributions and the distributions measured for jets of particles with large transverse momentum (high p_T jets) might be observed. Differences between the photon remnant and the Monte Carlo simulation, or between the photon remnant and the high- p_T jets, might also indicate that the structure of the photon remnant, and therefore of the photon, is different than is expected.

Chapter 2

Experiment

The data for this dissertation were collected with the ZEUS¹¹ detector, one of four experiments at the HERA¹² electron-proton collider. The HERA collider is operated by the Deutsches Elektronen Synchrotron (DESY) Laboratory located in Hamburg, Germany. The ZEUS detector was built by a collaboration of over 400 physicists, technicians and students from almost 50 institutes worldwide.

2.1 HERA

HERA stands for the Hadron Electron Ring Accelerator. HERA is the first and only electron-proton collider. It was built for the purpose of colliding electrons or positrons with protons, in order to use the electron as a probe to study the structure of the proton. The shape and dimensions of HERA are shown in Fig. 2.1. HERA has a circumference of 6.3 km and is located in an underground tunnel whose depth ranges between 10 and 25 meters. The proton ring, which uses superconducting magnets, is located above the electron ring, except at the four interaction points. The electron ring uses conventional magnets.

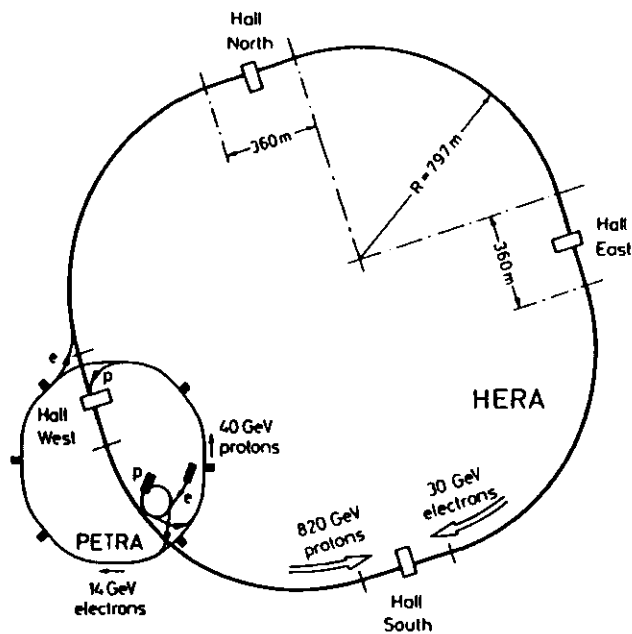


Figure 2.1: Orientation of the HERA ep collider.

In 1993, when the data for this dissertation was taken, HERA operated with a proton beam energy of 820 GeV, and an electron beam energy of 26.7 GeV. Therefore, the center of mass energy, \sqrt{s} , was 296 GeV. The HERA beams are divided into bunches of electrons and protons. HERA has the capacity for 210 colliding bunches, with each bunch crossing occurring at 96 ns intervals. The proton beam is filled first, with 10 GeV proton bunches being injected into HERA. When all of the proton bunches are in place, they are

accelerated to 820 GeV. After the protons have been successfully accelerated, the electrons are injected into HERA. The electrons are then accelerated from 14 to 26.7 GeV. After both beams have been accelerated they are brought into collision.

In 1993, HERA was operated with 84 colliding bunches. Ten additional electron and six additional proton "pilot bunches" circulated without collisions to allow direct measurements of beam-gas interactions, *i.e.* collisions between the beams and gas molecules within the beam pipe. In 1993 typical electron and proton currents were both around 10 mA and the instantaneous luminosity was around $6.0 \times 10^{29} \text{ cm}^{-2} \text{ s}^{-1}$. The total integrated luminosity delivered by HERA in 1993 was about 1 pb^{-1} . A comparison between a variety of HERA design parameters and what was actually achieved in 1993 is shown in table 2.1

HERA Parameters	Design		1993	
	electron	proton	electron	proton
Beam Energies (GeV)	30	820	26.7	820
Beam Currents (mA)	58	160	10	10
Filling Time (hours)	0.25	0.3	1	2
Lifetime (hours)	8	8	8	99
Number of Colliding Bunches	210		84	
Luminosity ($\text{cm}^{-2} \text{ s}^{-1}$)	1.5×10^{31}		0.6×10^{30}	
Integrated Luminosity (pb^{-1})	100		1	
Time Between Crossings (ns)	96		96	

Table 2.1: Comparison between some HERA design parameters and what was actually achieved in 1993.

2.2 The ZEUS Detector

The ZEUS detector was built to study ep collisions at HERA. It is located in the South Hall shown in Fig. 2.1. The general layout of the ZEUS detector is shown in Fig. 2.2. The ZEUS detector is made up of a large number of distinct components. The primary component used in this analysis is the calorimeter, in which the energy and position of particles produced in ep collisions are measured. The tracking detectors, which reconstruct charged particle tracks, and the trigger, which separates ep interactions from background events, were also important. Since a detailed description of the entire ZEUS detector already exists,¹¹ only the components used in this analysis will be described here.

2.2.1 Calorimeter

When a high energy particle collides with a dense material, a shower of secondary particles is produced. For particles that interact electromagnetically, the dominant mechanisms for producing particle showers are bremsstrahlung and electron-positron pair production. For particles that interact strongly (hadrons), inelastic collisions with nuclei result in showers of secondary hadronic particles (mostly pions). Calorimeters measure the incident particle energy by containing the particle shower, and measuring a fraction of the energy deposited by the shower. The ZEUS calorimeter¹³ is a sampling calorimeter. Sampling calorimeters are made of layers of a high density "absorber" material interspersed with "active" layers, such as scintillator. The active material "samples" the energy deposited in the entire calorimeter. The

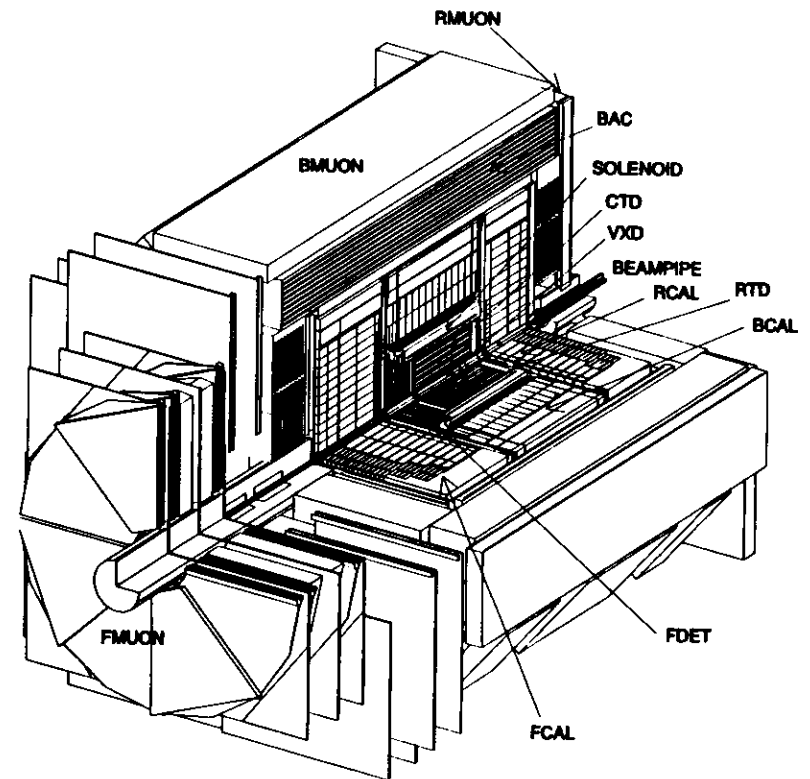


Figure 2.2: Cut-away view of the ZEUS detector.

observed energy is then proportional to the actual energy of the incident particle.

The ZEUS calorimeter is composed of alternating layers of depleted uranium and plastic scintillator. The calorimeter covers 99.7% of the total solid angle (4π). Figure 2.3 shows the structure of the ZEUS calorimeter. It

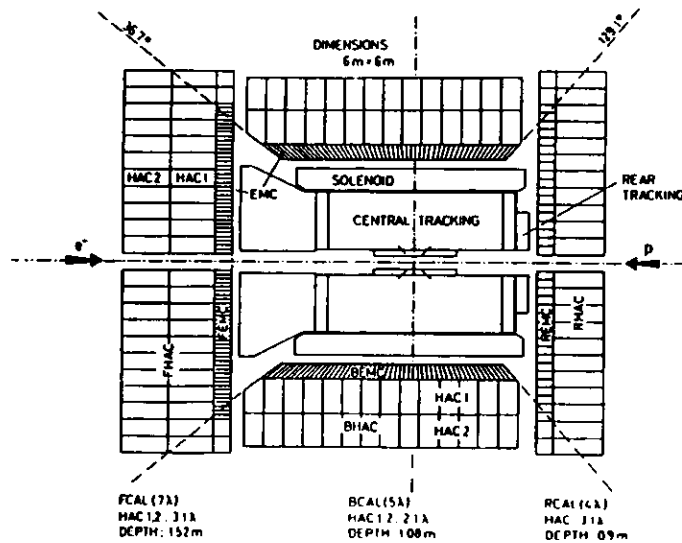


Figure 2.3: A cross sectional view of the ZEUS calorimeter is shown, divided into hadronic and electromagnetic cells.

consists of three parts: the forward calorimeter (FCAL) covering the region $2.2 < \theta < 39.9$, the barrel calorimeter (BCAL) covering the region $36.7 < \theta < 129.1$ and the rear calorimeter (RCAL) covering the region $128.1 < \theta < 176.5$. The angle θ is measured with respect to the proton beam direction. In the ZEUS coordinate system, the z axis is defined to lie along the

proton direction. The y axis points upward and the x axis points toward the center of the HERA ring. Because of the asymmetric beam energies the FCAL must be much thicker than the RCAL in order to fully contain the hadronic energy. By segmenting each of the calorimeters into many individual "cells" the position at which the energy is deposited can also be determined.

The different types of particle showers produced by electromagnetic and hadronic interactions behave differently inside the calorimeter. Electromagnetically interacting particles tend to begin showering immediately upon entering the calorimeter, and the depth to which the electromagnetic shower penetrates the calorimeter tends to be shallow. The penetration depth, for electromagnetically interacting particles, is measured in units of radiation lengths, X_0 . Hadronically interacting particles, on the other hand, tend to penetrate much deeper before they begin to shower, and the shower depth and breadth are greater. For hadronically interacting particles, the penetration depth depends on the absorption length, λ , of the material. The fact that electromagnetically interacting particles do not penetrate as deeply into the calorimeter as hadronically interacting particles is used to distinguish between showers produced by electromagnetic and hadronic particles.

The ZEUS calorimeter is divided into inner and outer layers of cells. The innermost layer of cells is called the electromagnetic calorimeter (EMC). It is thick enough (about $25 X_0$ or 22 cm) to contain essentially all of the energy deposited by electromagnetically interacting particles. The electromagnetic cells have the transverse dimensions $5 \times 20 \text{ cm}^2$ in the FCAL and BCAL. In the RCAL they are twice as large, with transverse dimensions $10 \times 20 \text{ cm}^2$. Behind the electromagnetic calorimeter is the hadronic calorimeter (HAC).

There are two layers of hadronic cells (HAC1 and HAC2) in the FCAL and BCAL, and one layer of hadronic cells in the RCAL. The hadronic cells measure $20 \times 20 \text{ cm}^2$ transversely, except in the BCAL where they are wedge shaped. One $20 \times 20 \text{ cm}^2$ calorimeter unit, made up of EMC cells and the HAC cells behind them (four EMC and two HAC cells in the FCAL and BCAL, two EMC and one HAC cell in the RCAL) is called a tower. In the FCAL and BCAL, hadronic cells are 61 cm deep, which corresponds to 3.09λ . In the RCAL, hadronic cells are 42 cm, or 2.03λ deep. The total depths of the FCAL, BCAL, and RCAL are 7, 5 and 4 λ , respectively.

In addition to the different penetration depths of electromagnetic and hadronic particles, the fraction of the total energy deposited in the active calorimeter layers is, for most sampling calorimeters, lower for hadronic particles than for electromagnetic particles. This fraction also tends to be nonlinear as a function of the energy of the incident particle. Therefore, the determination of the energy of the incident particle, or jet of particles, is a very complex problem. To avoid this problem, the ZEUS calorimeter was designed to be "compensating"; it was designed to enhance hadronic showers and suppress electromagnetic showers to compensate for the lower fraction of hadronic energy observed.¹¹ In the ZEUS calorimeter, energy is added to hadronic showers by increasing the number of neutrons produced in the hadronic showers. Although pions are produced in the greatest numbers in hadronic showers, neutrons are also produced. Neutrons tend to deposit a higher fraction of their energy in scintillator than do other particles. Therefore, increasing the number of neutrons produced in a shower (by making the

calorimeter out of depleted uranium (DU) for example) can increase the measured energy for hadronic particles. In addition, the electromagnetic response can be suppressed by increasing the thickness of the absorber material (compensating lead-scintillator calorimeters also use this method). By choosing the proper thicknesses for the depleted uranium (3.3 mm) and scintillator (2.6 mm) layers, the proper balance between enhancing the hadronic response and suppressing the electromagnetic response can be achieved so that the calorimeter response to electromagnetic and hadronic particles is equal. The response of the ZEUS calorimeter to electrons and hadrons has been measured to be equal and linear in energy to within 2% for energies above 3 GeV. In addition, the energy resolution (in GeV) achieved in test beams is $\sigma/E = 18\%/\sqrt{E}$ for electrons and $\sigma/E = 35\%/\sqrt{E}$ for hadrons.¹¹

Trigger

Trigger information from the calorimeter is provided by the Calorimeter First Level Trigger (CFLT).¹⁵ The CFLT is made up of dedicated, pipelined electronics with many programmable parameters. Energy from the calorimeter cells is summed into trigger "towers". A typical tower arrangement is shown in fig. 2.4. In general, four EMC cells and two HAC cells make up tower EMC and HAC sums, respectively. Ideally, particles produced at the interaction point only pass through the cells which make up one tower. Although the calorimeter is largely nonprojective, the sums of cells into trigger towers have been arranged to be as projective as possible. The actual trigger tower arrangement is shown in fig. 2.5. The information from each tower is used for pattern recognition, such as searching for isolated electrons or jets, and it is

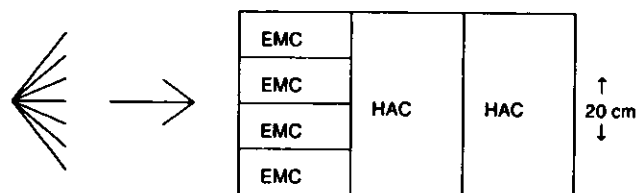


Figure 2.4: View of a typical calorimeter trigger tower.

combined into regional and global energy sums. Although all of the CFLT hardware was installed in 1993, some of the more specialized triggers, such as the isolated electron trigger, were not used until the 1991 run. Since the luminosity and trigger rates were low, only regional and global energy sums were used as calorimeter triggers in 1993. The entire trigger system is described in section 2.2.6.

Timing

The timing resolution for each calorimeter cell is $\sigma_t = 1.5/\sqrt{E} \oplus 0.5$ ns, where E (GeV) is the energy deposited in the cell.¹³ The timing information from the calorimeter is useful for removing both beam-gas and cosmic ray backgrounds. The time $t = 0$ ns is defined to be the time at which particles originating from ep collisions at the interaction point arrive at the calorimeter. When particles from beam-gas interactions which occur behind the RCAL deposit energy in the RCAL, the time at which the energy is deposited is negative. Therefore, a cut on the RCAL time can remove beam gas events. In addition, the “up-down” time difference; the difference between the time at which energy is

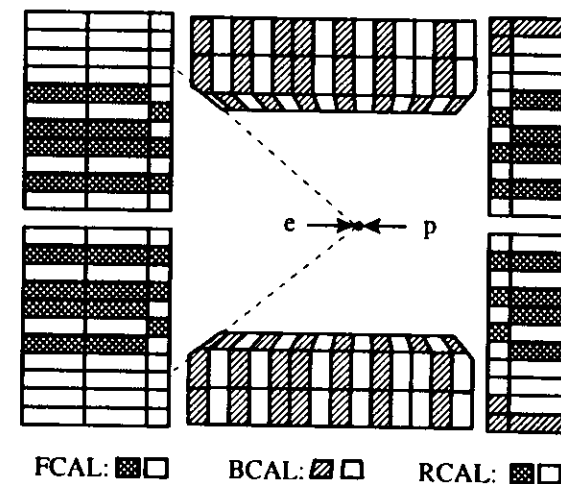


Figure 2.5: Semi-projective trigger tower arrangement.

deposited in cells at the top of the BCAL and the time at which energy is deposited in cells at the bottom of the BCAL, should be zero. However, for cosmic rays the up-down time difference will be greater than 10 ns. Therefore, cosmic ray events can also be removed with the calorimeter time information.

The vertex position along the z axis, z_{vertex} , can also be measured using calorimeter time information. The time, t , at which energy is deposited in the FCAL near the beam pipe from an ep collision will depend on the z vertex position according to the equation:

$$t = \frac{-2z_{vertex}}{c}, \quad (2.1)$$

where c is the speed of light. The correlation between the z vertex position measured using the tracking detectors (described in the next section) and the z vertex position measured using FCAL time information can also be used to

remove beam-gas interactions.

2.2.2 Central Tracking

The ZEUS tracking detectors measure the position of charged particles by observing their ionization of gas without interfering with their movement. ZEUS tracking is based on drift chambers. A simple drift chamber is made of a conducting tube filled with an easily ionized gas. A sense wire, which is held at high voltage, produces a high electric field within the gas. Charged particles which pass through the drift chamber ionize some of the gas molecules. The freed electrons then drift toward the sense wire, ionizing more gas molecules and producing a cascade of electrons which eventually reaches the sense wire. The signals detected on the sense wire are then used to measure and locate the position of the particle. Multiple measurements of a particle's position as it moves away from the interaction point, using a series of drift chambers or sense wires, are used to determine the particle's trajectory, and, within a magnetic field, its momentum. The ZEUS central tracking chamber (CTD) and vertex detector (VXD) contain numerous "cells" made up of many sense wires separated by ground wires.

The ZEUS tracking system used in this analysis consists of a vertex detector and a central tracking chamber. These components operate in a 1.43 T solenoidal magnetic field. The VXD is made of 120 radial cells with 12 sense wires each parallel to the beam direction.¹⁶ The CTD consists of 9 superlayers, with 8 layers of sense wires each.¹⁷ In this analysis the VXD and CTD were used primarily to determine the interaction vertex position. The position of the interaction vertex is measured with a resolution along the beam direction

of 0.4 cm and with a transverse resolution of 0.1 cm.

2.2.3 Luminosity Monitor

The luminosity is measured using the electron-proton bremsstrahlung process. The cross section for this process is calculable in QED and is known very accurately. In the bremsstrahlung process the incoming electron scatters intact from a proton and then loses energy by emitting a photon. The luminosity monitor¹⁸ is made up of two lead-scintillator calorimeters which detect the scattered electron and the emitted photon (Fig. 2.6). The scattered electron and photon travel in essentially the same direction as the electron beam. Bending magnets then deflect the electron beam out of the proton beam pipe. The scattered electron, which has lower energy than the beam electrons, is deflected through a window in the electron beam pipe into the electron calorimeter. The photon continues through the proton beam pipe until the beam pipe curves away. The photon then passes through a window in the proton beam pipe into the photon calorimeter. The experimental signature for an electron-proton bremsstrahlung interaction is an energy deposit in both the electron and photon calorimeters, with the total energy deposited of about 26.7 GeV. The accepted energy range is between about 6 and 17 GeV for the photon and between about 8 and 20 GeV for the electron. Therefore, the allowed energy sum ranges from 14 to 32 GeV.¹⁸

The electron calorimeter of the luminosity monitor is located 35 m from the interaction point in the electron direction from the ZEUS detector. It is made of 25 × 25 cm sheets of lead and scintillator. The lead sheets are 5.7 mm thick and scintillator sheets are 2.8 mm thick. The photon calorimeter is also

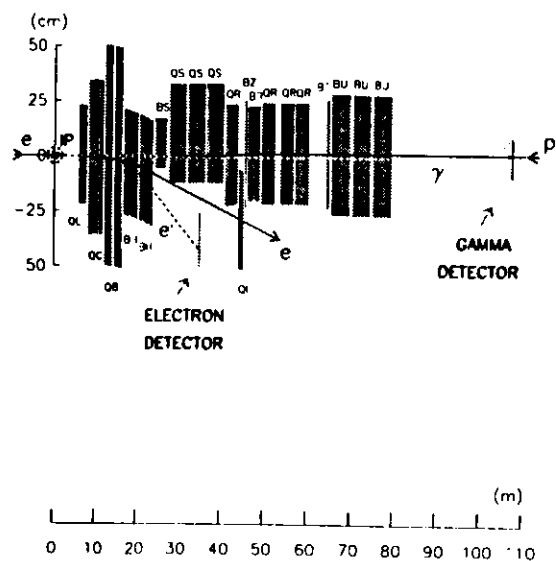


Figure 2.6: Layout of the ZEUS luminosity monitor.

made of sheets of lead and scintillator of the same thickness as the electron calorimeter. The photon calorimeter measures 18×18 cm and is located 107 m from the interaction point in the electron direction. The measured energy resolution of the two calorimeters is $\sigma/E = 18 \%/ \sqrt{E}$, where E is in GeV.

In addition to measuring the luminosity, the electron calorimeter is useful for tagging a subsample of photoproduction events. The signature for these events is an energy deposit in the electron calorimeter of the luminosity monitor with no corresponding energy deposit in the photon calorimeter. The scattered electron is detected in the electron calorimeter of the luminosity monitor in approximately 25% of all photoproduction events.

2.2.4 Veto Wall

The veto wall¹⁹ is an 87 cm thick wall of iron bricks oriented perpendicular to the beam between the ZEUS detector and the HERA tunnel. It is 800 cm wide and 907 cm high. The center of the veto wall is located at $z = -727$ cm. The beam pipe passes through a rectangular opening in the veto wall 80 cm wide and 175.5 cm high. Each side of the veto wall is covered with 48 identical scintillation counters.

The veto wall protects the central detector from the proton beam halo. These particles, which accompany the proton beam, result from beam-gas collisions upstream of the detector. Halo particles may also be produced through collisions of protons with the beam pipe wall and with the beam collimators. Sometimes the halo particles, particularly muons, pass through the veto wall. If a coincidence between the scintillation counters on each side of the wall occurs, a veto signal is generated which informs the first level trigger that the

crossing is contaminated.

2.2.5 C5 VETO Counter

The C5 VETO counter²⁰ is a small detector located at $z = -315$ cm, just downstream (in the proton direction) from the C5 collimator. It is a relatively thin detector made of two layers of scintillator (2.6 mm thick) sandwiched between three layers of lead. The lead sheets, moving away from the interaction point are 6, 3 and 4 mm thick, respectively. The C5 counter is oriented perpendicular to the beam, surrounding the beam on three sides. It is 190 mm high and 152.5 mm wide, and U-shaped so that the beam pipe can pass through it. It therefore, surrounds the beam pipe on three sides. It is divided in half, with a top and bottom section (the top of the U is in the positive x direction). The four sheets of scintillator are read out with four photomultiplier tubes.

The C5 counter detects particles outside of the beam pipe produced mainly from beam-gas interactions. The primary purpose for detecting these particles is to provide a VETO signal for the first level trigger to prevent these events from being taken as data. Because the C5 counter has good time resolution with respect to the bunch crossing time ($\sigma_t < 1$ ns), data from the C5 counter is used to determine the longitudinal distribution of the particles which make up the beams. It also provides a measure of the beam-gas background rate.

2.2.6 Experiment Trigger

The purpose of the trigger system is to distinguish interesting physics events from background events. This is necessary because beam-gas interactions occur at a rate of about 100 kHz, whereas only about five interesting $e p$ physics events occur each second. The task of separating the interesting physics events from background events is made more difficult because it must be done quickly. The trigger must be capable of making one trigger decision every 96 ns in order to keep up with the data input rate. The rate at which data can be written to tape is around five events per second, so the trigger has to remove essentially all of the background events while keeping the good physics events.

Because of the high rate of background events, the trigger was broken down into three levels.²¹ The layout of the ZEUS trigger system is shown in fig. 2.7.

Global First Level Trigger

The Global First Level Trigger (GFLT) makes a trigger decision every 96 ns, reducing the event rate by a factor of 100 to less than 1kHz. The GFLT receives pipelined trigger information from each of the component first level triggers, such as the CFLT described in section 2.2.1. The GFLT is also pipelined, with dedicated logic circuits, and programmable registers. The GFLT assembles the information from each of the components into a variety of trigger bits, and issues a trigger decision every 96 ns. The data are held in a 5 μ s pipeline while a fraction of the data for each event is processed by the component first level triggers and the GFLT. The entire first level trigger pipeline is also 5 μ s long.

In 1993, calorimeter trigger information, in conjunction with the C5 and veto wall information, was primarily used in making the GFLT decision. Six

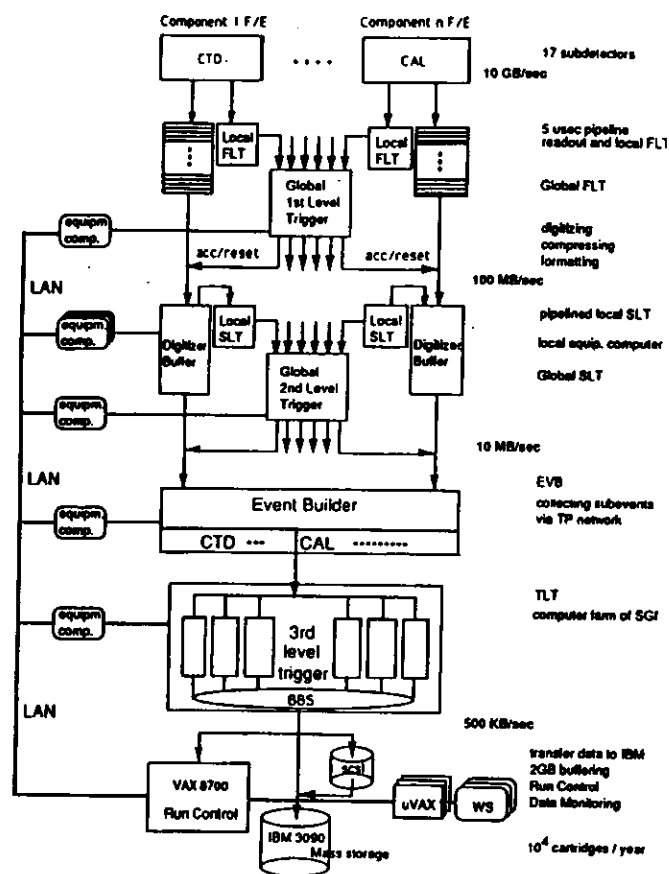


Figure 2.7: Diagram of the ZEUS three level trigger and data acquisition system.

first level triggers were used in this analysis: total calorimeter energy, total EMC energy, total transverse energy, EMC energy in the BCAL, EMC energy in the RCAL, and RCAL EMC energy excluding the first ring of towers around the RCAL beam pipe. The specific requirements are described in section 4.1. In 1993, the GFELT output rate varied between about 100 and 300 Hz, with an average of about 150 Hz.

Second Level Trigger

While the GFELT is making its decision, the data from all of the components are waiting in pipelines. After the GFELT decision is made, the data for the accepted events are digitized and passed through the individual component second level trigger processors. Much of the data available to the second level trigger is similar to that which was available to the first level trigger, but with greater precision and smaller granularity. There is also, however, additional information, such as the calorimeter time information described above. The component second level trigger processors are primarily INMOS transputers. The Global Second Level Trigger (GSLT) receives all of the second level trigger information from the individual components, as well as the trigger information from the GFELT. The GSLT then collects the information about these events and reduces the rate to less than 100 Hz. In 1993, the GSLT output rate averaged about 20 Hz. The GSLT is also made up of a network of INMOS transputers.

Third Level Trigger

If an event is accepted by the GSLT, the digitized data from all of the various components are read into the event builder. The event builder combines the data from all of the detector components and puts it into the final data format. This information is then sent to the Third Level Trigger (TLT). The TLT is a farm of 30 Silicon Graphics workstations. In the TLT, sophisticated algorithms, such as those used in off-line analyses for electron and jet finding, are used to analyze the data. The TLT reduces the event rate to about 5 Hz. Events selected by the TLT are then sent to the DESY mainframe IBM 3090 computer where they are written to tape.

Chapter 3

Monte Carlo Simulations

Monte Carlo simulations are used to model the response of the detector to particles and jets of particles over a wide energy range. In principle the detector response could be measured using particle beams. This has, in fact, been done for many detector components. In practice, however, it is impossible to put the whole ZEUS detector into a test beam to measure its response. Therefore, one important use of test beam information is to test and improve the Monte Carlo simulation of the detector components. The Monte Carlo simulation may then be used to determine the response of the complete detector. With this information, the data can be corrected for detector effects such as resolution smearing. In addition, by simulating entire physics events, rather than single particles or jets of particles, the detector acceptance for each class of events can be determined. These simulated events are also useful for determining whether different physical models actually agree with the data. For example, Monte Carlo events generated with a variety of different parton distribution functions can be compared with the data to determine which parton distribution function best describes the data.

3.1 Overview

There are three distinct steps in the creation of Monte Carlo events. First the hard scattering of partons, such as is shown in Fig. 1.2, is simulated. This results in a table of information about the outgoing partons. These “parton level” events are then passed through a hadronization model which fragments the color-charged partons into color-neutral hadrons. The fragmentation process is modeled phenomenologically since the underlying physics is not well understood. The decay of unstable hadrons is also included in the hadronization model. The result is a table of information about the outgoing “final state” hadrons. Finally, the “hadron level” events are passed through the simulated detector and trigger. The resulting events are stored in the same format as is the raw data, and are reconstructed with the same event reconstruction programs used on the data. The “detector level” Monte Carlo events may then be directly compared with the data.

3.2 PYTHIA

In this dissertation, the data are compared to Monte Carlo simulations based on the PYTHIA 5.6²² event generator. PYTHIA models both the hard parton scattering and the hadronization process. The calculation of the hard parton scattering is done using LO QCD diagrams. The scale of the hard parton scattering is determined by \hat{p}_T , the transverse momentum of each of the outgoing partons (in any event, all of the outgoing partons have equal transverse momentum). Since the calculated cross section diverges as \hat{p}_T approaches zero, a lower limit, $\hat{p}_T \geq \hat{p}_{T,min}$, is imposed. The value of $\hat{p}_{T,min}$ is chosen to be

small enough that any events generated with a lower value of \hat{p}_T would not pass the selection cuts of the analysis for which the Monte Carlo events are to be used. In this dissertation the value of $\hat{p}_{T,min}$ used in PYTHIA was set at 2.5 GeV. In PYTHIA, the photon flux produced by the electron beam is calculated using the Weizsäcker-Williams²³ approximation, and a string fragmentation model²⁴ (JETSET 7.3) is used in the hadronization process. The parton densities used were GRV LO²⁵ for the resolved photon and MRSD_L²⁶ for the proton. For comparison, the parameterization LAC1²⁷ was also used for the resolved photon parton density.

3.3 HERWIG

The HERWIG 5.7²⁸ Monte Carlo event generator was used to check the PYTHIA results. HERWIG also models both the hard parton scattering and the hadronization process. Again, the hard parton scattering is calculated using LO QCD diagrams.

Most of the HERWIG events were generated with $\hat{p}_{T,min} = 2.5$ GeV. A few events (about 4%) generated with $\hat{p}_{T,min}$ set at 5 GeV were also included in the study. The photon flux in HERWIG were also calculated using the Weizsäcker-Williams approximation, but only for resolved events. For the direct events actual electron-proton calculations were used. The parton densities used were GRV LO for the resolved photon and MRSD_L for the proton. In HERWIG a cluster algorithm was used to model the fragmentation process.

After a large sample of HERWIG events had been generated and passed through the detector simulation, a mistake was discovered in the HERWIG

event generator, which significantly enhanced the quark content of the photon. Although the kinematics of these events appear to be correct, they are only used to check the PYTHIA results. Parton fragmentation, which is important in simulating the internal features of jets, is known to be slightly different between quarks and gluons. Therefore, measurements of internal jet features made using the HERWIG Monte Carlo sample may be less reliable than those made using the PYTHIA Monte Carlo sample.

3.4 Detector Simulation

The detector simulation program is called MOZART.^{11,29} It is based on a detector simulation package called GEANT 3.13.³⁰ MOZART passes the generated particles through the simulated detector, simulating particle decays, multiple scattering, the effect of the magnetic field, energy loss in dead material such as the solenoid, and any other physical processes, as well as the output signals of the various detector components. MOZART stores the detector information from the simulated events in the same format as the raw data.

The program ZGANA^{11,31} simulates the ZEUS trigger. After the simulated events have been passed through MOZART, ZGANA determines which triggers, if any, would have fired for each individual event.

3.5 The Resolved Photon

In both PYTHIA and HERWIG, the resolved photon is modeled in the same way as hadrons. The parton content of the photon is based on a photon-parton distribution function, and the incoming partons in the photon are collinear. Since partons can move around inside a hadronic object, they can have a small amount of transverse momentum. In PYTHIA the intrinsic transverse momentum, k_t , of the partons in the photon is parameterized by the distribution,

$$dN/dk_t^2 \propto e^{-k_t^2/k_0^2}, \quad (3.1)$$

where k_0 is a parameter which determines the hardness of the k_t spectrum. The same functional form is also used for the proton k_t . The PYTHIA default value of k_0 for both the proton and the resolved photon is 0.11 GeV.²²

One would expect the photon remnant, generated with this kind of a model, to have low- p_T with respect to the beam axis. Several studies, however, have suggested that contributions from diagrams of the type shown in Fig. 1.2c may lead to a "photon remnant" which has sizable transverse momentum with respect to the photon direction.^{22, 32, 33} In this dissertation, processes like those shown in Fig. 1.2c are called anomalous. Drees has suggested increasing the average k_t of the partons in the photon as a method of approximating the anomalous component.³⁴ An option in PYTHIA allows events to be generated using different functional forms for the k_t spectrum as well as different values of k_0 . This option has been used to generate events with a harder k_t spectrum.

The generated Monte Carlo event sample was obtained by combining the resolved and direct samples in proportion to the generated Monte Carlo cross

sections (approximately 7:1 for the GRV photon-parton densities). The number of events in the PYTHIA sample used in this dissertation is just under twice the size of the data sample. The number of events in the HERWIG sample is about 30% smaller than the data sample.

Chapter 4

Event Selection

The event selection criteria choose resolved photoproduction events with two high- p_T jets and a photon remnant. In this analysis, photoproduction events are defined by requiring that the electron was scattered at a small angle and was not detected in the calorimeter. This requirement corresponds approximately to a cut of $Q^2 \leq 1 \text{ GeV}^2$ (see section 1.1). The median value of Q^2 for events of this type has been estimated to be 10^{-3} GeV^2 using simulated direct photoproduction events.⁸ The selection of these events begins with the trigger. The trigger cuts are designed to select hard scattering events at low Q^2 while removing beam-gas events. After the data are collected, additional cuts are applied to remove the remaining beam-gas, DIS, and cosmic ray backgrounds. Finally, when a clean sample of photoproduction events has been isolated, a search for jets is performed and cuts are applied to select events which contain two high p_T jets and a photon remnant.

4.1 Trigger

The ZEUS detector uses a three level trigger, as described in section 2.2.6. In the first level trigger, calorimeter cell energies were combined to define regional

and global energy sums which were required to exceed given thresholds. Since the calorimeter is the primary component used in this analysis, one or more of the following calorimeter first level trigger conditions were required:

- RCAL EMC energy above 3.75 GeV.
- RCAL EMC energy, excluding the first ring of towers around the RCAL beam pipe, greater than 2.0 GeV.
- BCAL EMC energy above 3.1 GeV.
- Total calorimeter energy greater than 15 GeV.
- Total EMC energy greater than 10 GeV.
- Total transverse energy (excluding the first ring of towers around the FCAL beam pipe) above 11.6 GeV.

The second level trigger mainly rejected beam-gas interactions using timing information from the calorimeter.

The third level trigger performed further rejection of beam-gas and cosmic ray events using information from both the calorimeter and the tracking chambers. All events were required to meet the following conditions:

- The z position of the interaction vertex, measured using the central tracking chambers, was required to be in the region $|z| < 75$ cm, to remove beam-gas events.
- Beam-gas background was also removed by requiring $E^{cal} - p_z^{cal} \geq 8$ GeV, where E^{cal} is the total energy deposited in the calorimeter and p_z^{cal} is the total longitudinal energy deposited in the calorimeter. This

requirement is derived from energy and momentum conservation. Before an ep collision occurs, the total energy of the electron-proton system is:

$$E = E_p + E_e, \quad (4.1)$$

where $E_p = 820$ GeV is the proton energy and $E_e = 26.7$ GeV is the electron energy. Likewise, the total longitudinal momentum is:

$$p_z = p_{z,p} + p_{z,e}, \quad (4.2)$$

where $p_{z,p} = 820$ GeV¹ is the proton momentum in the z direction and $p_{z,e} = -26.7$ GeV is the electron momentum in the z direction. Since $p_{x,p} = E_p$ and $p_{x,e} = -E_e$, the quantity:

$$E - p_z = (E_p + E_e) - (E_p + -E_e) = 2E_e. \quad (4.3)$$

Because these quantities are conserved, the measured value of $E^{cal} - p_z^{cal}$ after the collision will be equal to about $2E_e$. Furthermore, particles lost in the forward beam pipe do not interfere with the measurement of $E^{cal} - p_z^{cal}$ since their contribution to $E^{cal} - p_z^{cal}$ is essentially zero. Particles lost in the rear beam pipe, however, will change the measured value of $E^{cal} - p_z^{cal}$. In photoproduction events, the electron is always lost down the rear beam pipe. In this case, $E^{cal} - p_z^{cal} \approx 2E_\gamma$ where E_γ is the energy of the incoming photon. For proton-beam-gas events, where little or no energy is deposited in the RCAL, $E^{cal} - p_z^{cal} \approx 0$ since $E - p_z$ was initially zero.

¹Here and throughout the remainder of this dissertation, the units of momentum, GeV/c, will be abbreviated as GeV.

- Some beam-gas events can deposit very large energies (> 100 GeV) in the FCAL. This can result in measured values of $E^{cal} - p_z^{cal}$ larger than 8 GeV. To remove these additional beam-gas events the sample was also required to have $p_z^{cal}/E^{cal} \leq 0.91$. In beam-gas events, p_z^{cal}/E^{cal} tends to be close to unity.
- Hard scattering events were selected by requiring $E_T^{cone} \geq 12$ GeV, where E_T^{cone} is the total transverse energy in the calorimeter, excluding a cone of 10° in the forward direction.

About 470,000 triggers were collected with the above trigger conditions during the 1993 run.

4.2 Off-line Data Selection

As in previous studies of hard photoproduction,^{9,35} the following cuts were applied off-line to select the final event sample.

- The requirements on the FCAL time, t_F , and on the RCAL time, t_R , were tightened to reduce the contamination from beam-gas interactions. Events were selected by requiring $t_R \geq -6$ ns and $(t_F - t_R) \leq 6$ ns.
- Beam-gas interactions were also rejected with cuts on the correlation between the vertex position (defined by the tracking chambers) and the calorimeter timing,³⁷ as described in section 2.2.1. Events were accepted when $|t_F(c/2) + z_{vertex}| < 60$ cm, where c is the speed of light.
- The E_T^{cone} cut was raised to $E_T^{cone} \geq 15$ GeV to select hard scattering events.

- To reduce beam-gas interactions, the event was rejected if less than 10% of the tracks pointed toward the vertex.
- To remove both beam-gas and DIS events, the fraction of the initial electron energy carried by the almost real photon, $y = E_\gamma/E_e$ where E_γ is the photon energy, was measured using the Jacquet-Blondel³⁸ estimator of the Bjorken y :

$$y_{JB} = \frac{E^{cal} - p_z^{cal}}{2E_e}. \quad (4.4)$$

To reduce uranium noise, the cell energies were required to be greater than 60 MeV for the electromagnetic cells and 110 MeV for the hadronic cells. This calculation assumes that the scattered electron was not detected in the calorimeter. For DIS events in which the electron deposited energy in the calorimeter but was not identified as an electron, y_{JB} will be near unity. Therefore, the requirement $y_{JB} < 0.7$ is made to further reject DIS events. To reject proton-beam-gas interactions, $y_{JB} \geq 0.2$ was also required. This is equivalent to increasing the minimum value of $E^{cal} - p_z^{cal}$ to 10.68 GeV. These requirements on y_{JB} correspond approximately to $0.2 < y < 0.85$.

- DIS events were also removed from the sample by searching for the scattered electron in the calorimeter and calculating y using the energy, E_e' , and scattering angle, θ_e' of the electron candidate. Events with $y_e \leq 0.7$ were rejected.^{6,8} Here y_e is given by:

$$y_e = 1 - \frac{E_e'}{2E_e} (1 + \cos\theta_e'). \quad (4.5)$$

All events in which an electron candidate is found are not removed because electrons found by the electron finder are not always the scattered electron and may not be an electron at all. However, when the electron finder finds an object which is not the scattered electron, y_e tends to be near one.

- To remove charged current background and cosmic ray showers, a cut on $\cancel{p}_T/\sqrt{E_T} < 1.5 \text{ GeV}^{1/2}$ was imposed, where \cancel{p}_T is the total missing transverse momentum and E_T is the total transverse energy of the event.

After these selection cuts, a sample of 99,891 events remained, corresponding to an integrated luminosity of 0.55 pb^{-1} . For these events, the proton-beam-gas background contribution is estimated from proton pilot bunches to be about 0.4%. The contamination from DIS events is estimated by DIS Monte Carlo simulation to be 1 to 2%. The backgrounds from cosmic ray events and electron-beam-gas events, estimated from empty bunches and electron pilot bunches, respectively, are negligible.

4.3 Jet Finding with the k_{\perp} Algorithm

After a clean sample of photoproduction events has been isolated, it is searched for jets of particles. In this dissertation, jets of particles which deposit significant amounts of energy in the calorimeter are found using a clustering algorithm called the k_{\perp} algorithm.³⁹ The k_{\perp} algorithm finds jets by iteratively merging clusters. Initially, clusters are individual calorimeter cells (or groups of calorimeter cells called islands, see section 6.1). For the Monte Carlo events, the algorithm is also used to cluster generated particles (see Chapter 5). In

the merging procedure, the quantity k_{\perp} (GeV^2) is evaluated for each pair of clusters,

$$k_{\perp} = 2E_{\min}^2(1 - \cos\theta_{nm}), \quad (1.6)$$

where θ_{nm} is the angle between the two clusters n and m (the location of a calorimeter cell is given by its geometric center), and E_{\min} is the smaller of the two cluster energies E_n and E_m . In the small angle approximation, k_{\perp} is the transverse momentum squared of the lower energy cluster with respect to the higher energy cluster. To account for the fact that much of the proton debris is lost in the FCAL beam pipe, a pseudo-particle with infinite momentum along the z axis is included in the clustering procedure. The pseudo-particle acts as a seed to associate energy deposits near the FCAL beam pipe with the proton remnant. The value of k_{\perp} between the pseudo-particle and the other clusters is calculated using the same formula as above. When all of the k_{\perp} values have been calculated, the two clusters with the lowest k_{\perp} value are merged. The four-momentum of the new cluster is the sum of the four-momenta of the two merged clusters. The calculation of k_{\perp} is then repeated, replacing the two merged clusters with the new cluster. The iteration continues until the energy-angle resolution variable, Y , becomes larger than some threshold, Y_{cut} (see also sections 4.5 and 6.7). The quantity Y is a dimensionless variable related to k_{\perp} :

$$Y = \frac{k_{\perp}}{E_T^2}. \quad (1.7)$$

Here, E_T is the total event energy transverse to the beam axis. The value of Y_{cut} may be fixed for all events, or the number of clusters found may be fixed for all events. In the second case, Y_{cut} is set, on an event-by-event basis, at the minimum value of Y which returns the requested number of clusters. In

this analysis, three clusters are found in each event (see next section). This implementation of the k_{\perp} algorithm is not Lorentz invariant. The analysis is performed in the laboratory frame.

4.4 Identification of the Photon Remnant

To identify the photon remnant, an intuitive approach is used which is later justified using simulated events. As illustrated in Fig. 1.2b, resolved hard photoproduction events have a final state which includes two high- p_T jets from the hard scattering as well as photon and proton remnants. Since one expects to find three clusters (in addition to the proton remnant) in each resolved photoproduction event, the value of Y_{cut} was chosen on an event-by-event basis so that three clusters are found in addition to the proton remnant. The three clusters then, should correspond to the two clusters from the hard scattering and to the photon remnant. Since the photon remnant is expected to have low transverse momentum with respect to the beam axis, the separation between the photon remnant and the two jets from the hard scattering can be achieved, to a first approximation, by associating the photon remnant with the cluster having the smallest transverse momentum. For direct events, where a photon remnant should not be seen, the lowest transverse momentum cluster will either be part of the proton remnant or part of one of the two high transverse momentum jets. Therefore, the pseudorapidity distributions of the lowest transverse momentum clusters will be different for resolved and direct events.

In Fig. 4.1a-c, the (uncorrected) pseudorapidity distributions of the three

clusters obtained with the k_{\perp} algorithm are shown. The pseudorapidity, η , is given by equation 1.6. The superscript *cal* is used to denote uncorrected calorimeter quantities. The data (full circles) and Monte Carlo events (histogram) are shown normalized in the uncorrected pseudorapidity region $\eta^{cal} \leq 1.6$. While the two clusters with the highest uncorrected transverse momentum, p_T^{cal} , (Fig. 4.1a,b) are mostly found in the $\eta^{cal} > 0$ region, the third cluster, with the lowest p_T^{cal} , (Fig. 4.1c) is observed mostly in the $\eta^{cal} < 0$ region, *i.e.* in the photon direction. Data and Monte Carlo expectations agree for the two highest p_T^{cal} clusters except in the forward region, $\eta^{cal} > 1.6$, where the data has considerably more events. This phenomenon is similar to that already reported in previous analyses.^{9,35} Although this effect is not yet fully understood, multiple interactions (collisions in which two or more partons in the resolved photon interact with an equal number of partons in the proton) currently show the most promise in improving the Monte Carlo description of the data.³⁶

The peak observed in Fig. 4.1c, for the third cluster, in the negative pseudorapidity region is described by the Monte Carlo simulation including resolved and direct processes (full histogram). However, the Monte Carlo distribution is shifted slightly to lower values of pseudorapidity. The direct process, which does not contain a photon remnant, does not contribute to this peak as shown by the dashed line in Fig. 4.1c. Therefore, the pseudorapidity of the third cluster can be used to separate direct and resolved events. In addition, the third cluster, when it is in the negative pseudorapidity region, can be associated with the photon remnant.

In order to maximize the possibility that the two highest p_T^{cal} clusters stem

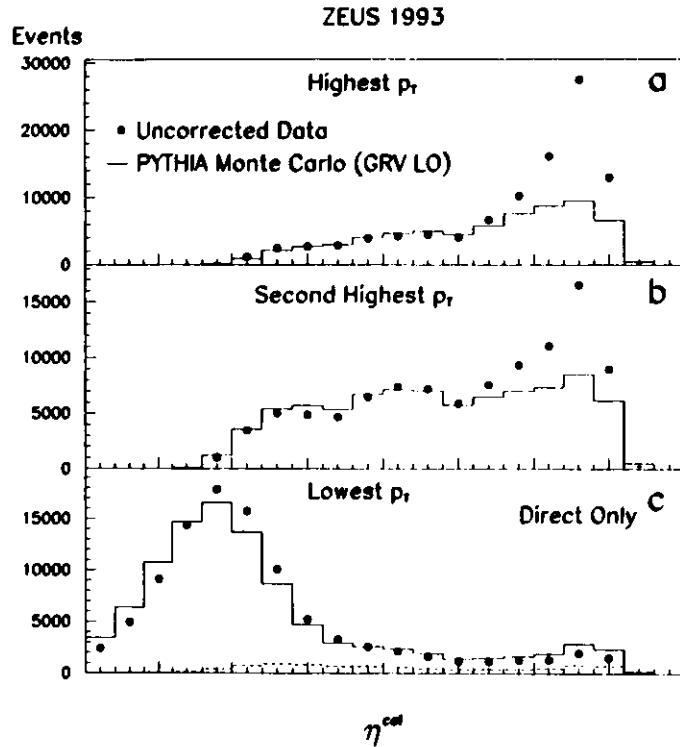


Figure 4.1: Pseudorapidity distributions of clusters for the inclusive photo-production sample. The three clusters are sorted by p_T^{cal} with (a) having the highest, (b) the second highest, and (c) the lowest p_T^{cal} . Each Monte Carlo distribution is independently normalized to the data in the region $\eta^{\text{cal}} < 1.6$. In (c) the direct contribution alone is shown as the dashed line.

from the partons in the hard scattering and to minimize the possibility that one of the two highest p_T^{cal} clusters is, in fact, part of the proton remnant, the two highest p_T^{cal} clusters are required to have high transverse momentum, $p_{T1,2}^{\text{cal}} > 5 \text{ GeV}$ (the subscripts 1, 2, and 3 correspond to the highest, second highest, and lowest p_T^{cal} cluster, respectively). They are also required to be well separated from the forward region ($\eta_{1,2}^{\text{cal}} < 1.6$), where the Monte Carlo simulation cannot reproduce the data.

The distribution of the pseudorapidity of the third cluster, η_3^{cal} , after the above cuts and the requirement $E_3^{\text{cal}} > 2 \text{ GeV}$, is shown in Fig. 4.2. The comparison with the distribution predicted for direct processes shows that the events with $\eta_3^{\text{cal}} < -1$ are almost exclusively due to resolved processes. The agreement between the data and the Monte Carlo simulation, including both the resolved and direct contributions, is not perfect; there are fewer events in the data with large negative η_3^{cal} values. This difference between the data and the Monte Carlo simulation is not improved when the photon parton parameterization LAC1 (dotted line) is used instead of GRV LO.

In summary, for the following analysis, the final resolved photoproduction event sample is selected by requiring:

- $p_{T1,2}^{\text{cal}} > 5 \text{ GeV}$
- $\eta_{1,2}^{\text{cal}} < 1.6$
- $E_3^{\text{cal}} > 2 \text{ GeV}$
- $\eta_3^{\text{cal}} < -1$

After the above selection cuts, 1370 events containing two high p_T jets and a photon remnant in the rear direction are selected.

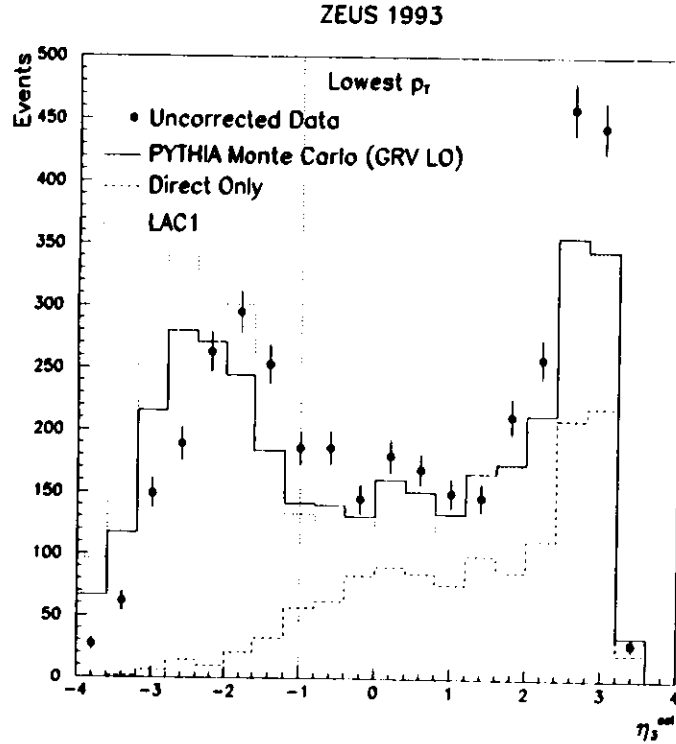


Figure 4.2: Pseudorapidity distribution of the lowest p_{T3}^{cal} cluster. The η_3^{cal} distribution (as in Fig. 4.1c) is shown again after requiring $p_{T1,2}^{cal} > 5$ GeV, $\eta_{1,2}^{cal} < 1.6$, and $E_3^{cal} > 2$ GeV. Resolved events are selected by requiring $\eta_3^{cal} < -1$ (vertical dotted line). The dotted histogram shows the Monte Carlo expectation using the LAC1 photon parton parameterization.

4.5 Direct and Resolved Separation

To further demonstrate that the simple requirement $\eta_3^{cal} < -1$ selects resolved events, the measured x_γ distribution, x_γ^{cone} is shown in Fig. 4.4. Here, x_γ^{cone} is calculated using the formula:

$$x_\gamma^{cone} = \frac{(E_1^{cal} - p_{z1}^{cal}) + (E_2^{cal} - p_{z2}^{cal})}{E^{cal} - p_z^{cal}}, \quad (4.8)$$

where E_1^{cal} and p_{z1}^{cal} are the energy and longitudinal energy of the highest E_T^{cal} jet found using a cone algorithm⁴⁰ (see section 4.6.1), and E_2^{cal} and p_{z2}^{cal} are the energy and longitudinal energy of the second highest E_T^{cal} jet found using the cone algorithm. The quantity x_γ^{cone} is the ratio of $E^{cal} - p_z^{cal}$ (described in section 4.1) for the two jets only and $E^{cal} - p_z^{cal}$ for the entire event. Since the two high- p_T jets presumably come from the hard scattering process, then the value of $E^{cal} - p_z^{cal}$, for the two jets only, provides a measure of the energy of the photon or parton within the photon which was involved in the hard scattering process. If the event was a direct event then it will only contain two jets and x_γ^{cone} will be equal to 1. However, if the event has a significant deposit of energy in the rear direction, outside of the two jets (a photon remnant), then $E^{cal} - p_z^{cal}$ for the two jets will be significantly smaller than $E^{cal} - p_z^{cal}$ for the entire event, so x_γ^{cone} will be less than 1. Measurements of x_γ^{cone} have been used in previous analyses^{8,9} to separate direct and resolved events. Figure 4.3 shows how well direct and resolved Monte Carlo events can be separated based on x_γ^{cone} . The direct events tend to have large values of x_γ^{cone} , while the resolved events are mostly at low values of x_γ^{cone} . Events with $x_\gamma^{cone} > 0.75$ are defined as direct events, while events with $x_\gamma^{cone} \leq 0.75$ are defined as resolved events. The solid line in Fig. 4.1 shows the x_γ^{cone} distribution for those events in which

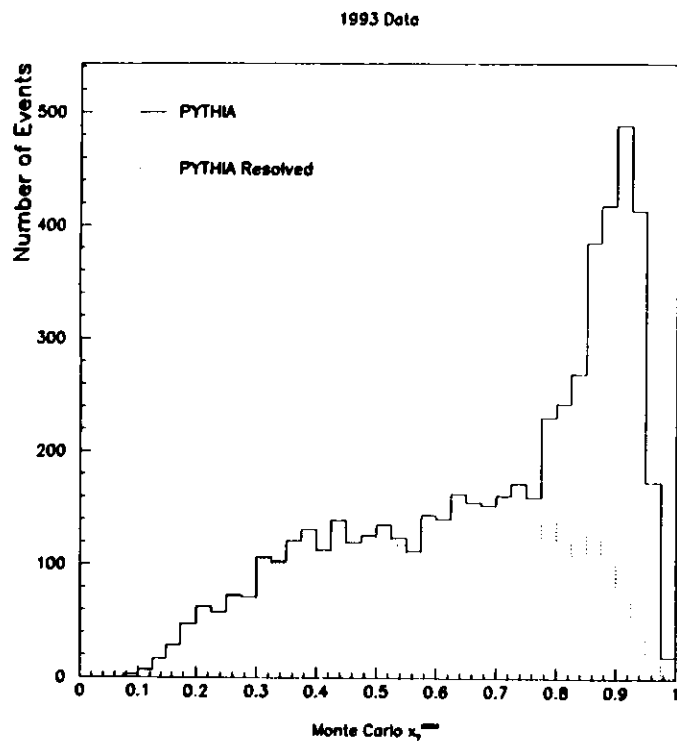


Figure 4.3: The solid line shows the Monte Carlo x_3^{cone} distribution including both direct and resolved events passing cuts applied to the quantities found with both the k_{\perp} and cone algorithms. The dotted line shows the resolved process only. Direct events are defined as events with $x_3^{\text{cone}} > 0.75$.

both the cone and k_{\perp} algorithms found two jets satisfying $\eta_{1,2}^{\text{cal}} < 1.6$, and $p_{T1,2}^{\text{cal}} > 5$ GeV. The direct events produce a peak at $x_3^{\text{cone}} = 0.9$, while the

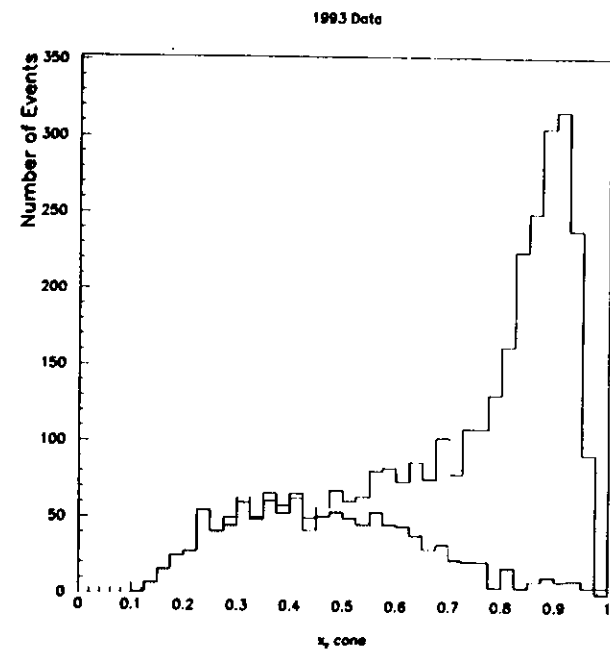


Figure 4.4: The solid histogram is the x_3^{cone} distribution for the data with cuts applied to the quantities found with both the k_{\perp} and cone algorithms. The shaded region shows the events which remain after requiring $\eta_3^{\text{cal}} < -1$.

resolved events peak at about $x_3^{\text{cone}} = 0.1$. The shaded region indicates the shape of the x_3^{cone} distribution after requiring $\eta_3^{\text{cal}} < -1$. As expected, this constraint removes almost all of the direct events while leaving the low x_3^{cone} events untouched. In Fig. 4.1, about 8% of the events have $x_3^{\text{cone}} > 0.75$. The

contribution from direct photon interactions, estimated using LO direct Monte Carlo events, is also 8%.

Additional evidence that the requirement $\eta_3^{ct} < -1$ selects resolved events is presented in section 6.7.

4.6 Comparison of the k_{\perp} and cone algorithms

Jet finding in $\eta - \phi$ space using a cone algorithm has been widely used in the analysis of ep and pp experiments. Since the use of a clustering algorithm which is not Lorentz invariant is less familiar, a comparison of the two algorithms is useful here. One implementation of the cone algorithm used by the ZEUS collaboration is called EUCCELL.

4.6.1 The Cone Algorithm

Previous analyses of photoproduction at HERA have implemented a cone algorithm to find jets.^{6,7,8,9} Cone algorithms use a cone of fixed radius in pseudorapidity and azimuthal angle space and maximize the transverse energy within this cone. The cone algorithm described in this section is called EUCCELL.

This algorithm:

1. Searches $\eta - \phi$ space for the point where the transverse energy within a cone of radius $R = \sqrt{\Delta\phi^2 + \Delta\eta^2} = 1$ is maximized.
2. If the maximum transverse energy within the cone is less than 3.5 GeV, the algorithm stops looking.

3. If the maximum transverse energy within the cone is greater than 3.5 GeV, an energy cluster is formed from the calorimeter cells located within the cone.
4. The calorimeter cells assigned to the new cluster are removed from the search and the algorithm returns to step 1.

The number of clusters found depends only on the 3.5 GeV threshold, which may be raised or lowered. The location of the cluster axis is calculated as the transverse energy-weighted mean value of the η and ϕ position of the center of the cell. To remove the proton remnant, all cells within 10° of the proton direction are removed from the search. The use of a cone in $\eta - \phi$ space makes this algorithm Lorentz invariant.

Cone algorithms are well suited to finding high transverse energy jets. The photon remnant, however, is expected to deposit energy in the electron direction with low transverse energy (see Fig. 1.3). Due to the rapid variation of pseudorapidity in this region, and to the low transverse energy, a cone algorithm cannot be used to identify the photon remnant. Therefore, the k_{\perp} clustering algorithm (see section 4.3) was used instead of a cone algorithm.

4.6.2 Algorithm Comparison

A correlation plot of the pseudorapidity of the highest p_T cluster at the detector level, as found by the two algorithms, η_1^{cone} and $\eta_1^{k_{\perp}}$ ($= \eta_1^{ct}$), is shown in figure 4.5a. The figure indicates that the cluster axis as found by the cone algorithm is, for some fraction of the events, shifted toward the proton direction by the k_{\perp} algorithm. There are several reasons why this type of effect

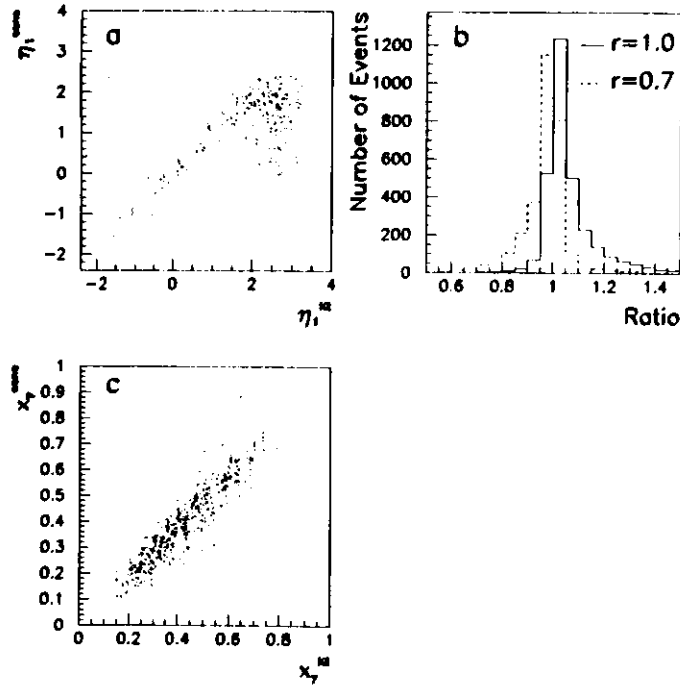


Figure 1.5: Comparison between quantities found using the k_{\perp} and cone algorithms. (a) Pseudorapidity comparison, (b) cluster transverse energy ratio, (c) x_{γ} comparison, and (d) RCAL energy.

occurs. One reason is the way in which the two algorithms deal with the proton remnant. The cone algorithm removes all cells within a 10° cone around the FCAL beam pipe before any cluster finding begins. The k_{\perp} algorithm, on the other hand, uses a pseudo-particle along the proton direction in an active attempt to find the proton remnant. In some cases this results in the k_{\perp} algorithm finding a cluster within 10° of the FCAL beam pipe. However, a good correlation between the two algorithms exists excluding events with $\eta_{1,2}^{k_{\perp}}$ above about 2. These events are excluded because of the requirement $\eta_{1,2}^{cone} < 1.6$.

Another effect which will increase the pseudorapidity (in the forward direction) of clusters found using the k_{\perp} algorithm, with respect to clusters found using the cone algorithm, is the way in which the cluster axis is determined. In the cone algorithm, transverse energy is maximized when searching for clusters, and the cluster axis is determined using transverse energy. For the k_{\perp} algorithm, energy, rather than transverse energy, is used to determine the cluster axis. Therefore, even if the clusters found by the k_{\perp} and cone algorithms are identical, the pseudorapidity found by the k_{\perp} algorithm will still tend to be slightly larger.

Figure 1.5b shows the distribution of the ratio, $p_{T1}^{k_{\perp}}/E_{T1}^{cone}$, where $p_{T1}^{k_{\perp}}$ is the transverse momentum of the highest $p_T^{k_{\perp}}$ cluster as found by the k_{\perp} algorithm, and E_{T1}^{cone} is the transverse energy of the highest E_T^{cone} cluster found by the cone algorithm. The events are required to have $\eta_1^{k_{\perp}}$ and $\eta_1^{cone} < 1.6$, and $p_{T1}^{k_{\perp}}$ and $E_{T1}^{cone} > 5$ GeV. Figure 1.5b indicates that the k_{\perp} algorithm, on average, finds less transverse energy than does the cone algorithm with a cone radius of 1.0. The dotted line shows the same ratio after reducing the cone radius to 0.7. In this case the k_{\perp} algorithm finds more transverse energy than the cone

algorithm. Therefore, the effective cone size of the k_{\perp} algorithm is between 0.7 and 1.0.

The number of events which pass the cuts on the quantities found with the two algorithms are shown in Table 4.1. Significantly fewer events pass the cuts when the k_{\perp} algorithm is used. This is primarily because of the higher average pseudorapidity and lower average transverse momenta of the clusters found by the k_{\perp} algorithm, with respect to the clusters found by the cone algorithm.

	cone algorithm	
	accepted	rejected
k_{\perp} algorithm accepted	3356	179
k_{\perp} algorithm rejected (total)	5227	—
k_{\perp} algorithm rejected ($\eta_{1,2}^{k_{\perp}} > 1.6$)	3223	
k_{\perp} algorithm rejected ($p_{T1,2}^{k_{\perp}} < 5.0$)	2569	

Table 4.1: Comparison of the number of events accepted and rejected when cuts are applied to the quantities found by the cone and k_{\perp} algorithms. Of the 5227 events which passed the cuts on the cone quantities but failed the cuts on the k_{\perp} quantities, 3223 failed at least one of the $\eta_{1,2}^{k_{\perp}}$ cuts, and 2569 failed at least one of the $p_{T1,2}^{k_{\perp}}$ cuts.

The physical quantities calculated by the two algorithms are in good agreement if the events survived the cuts for both algorithms. Figure 4.5c, for example, shows the correlation between x_5^{cone} and $x_5^{k_{\perp}}$. The quantity x_5^{cone} is given by equation 4.8. The equation for $x_5^{k_{\perp}}$ is the same as equation 4.8 except that the quantities E_1^{cal} , p_{z1}^{cal} , E_2^{cal} and p_{z2}^{cal} are now found using the k_{\perp} algorithm. The correlation between the two x_5 measurements is good.

Chapter 5

Data Corrections

In order to allow comparisons between the data and QCD calculations, the data must be corrected to remove effects related to detector acceptance and resolution. As described in Chapter 3, the Monte Carlo goes through three distinct steps in generating a fully simulated event. In the first step, the ep collision is simulated, resulting in two or more outgoing partons. The partons are then fragmented into hadronic particles. Finally, the hadronic particles are passed through the simulated detector. Ideally, one would like to correct the data completely, i.e. back to the parton level. However, correcting the data back to the parton level depends on the specific parton fragmentation model used. Therefore, to avoid making the measured data dependent on the model, the data are corrected back to the hadron level.

5.1 Hadron Level Kinematic Region

To avoid using the Monte Carlo simulation outside of the measured kinematic region, cuts are applied at the hadron level which roughly correspond to the cuts applied to the data as described in section 1.1. For the Monte Carlo events, the k_{\perp} algorithm is applied independently at both the hadron and

detector levels. In both cases the resulting clusters are sorted according to p_T . The detector level cuts in η^{ad} , p_T^{ad} , E_3^{ad} , and y_{JB} correspond approximately to two jets at the hadron level with $p_{T1,2} > 6.0$ GeV and $\eta_{1,2} < 1.6$, a remnant cluster with $\eta_3 < -1$ and $E_3 > 2$ GeV, and $0.2 < y < 0.85$. Therefore, the hadron level Monte Carlo events were required to be within this kinematic region. Therefore, the corrected photon-proton center of mass energy range is $130 < W_{\gamma p} < 270$ GeV.

5.2 Matching

Energy clusters found using particles at the hadron level should have roughly the same energy and position as the energy clusters found using calorimeter cells. However, the clusters at the hadron and detector levels are sorted independently by p_T . Therefore, the highest p_T cluster at one level is not necessarily the highest p_T cluster at the other level. This is especially true when the event contains two clusters which are well balanced in p_T . For this reason, one cannot correct the energy (or any other quantity) of the highest p_T^{ad} cluster at the detector level to the highest p_T cluster at the hadron level without considering whether or not they are in fact the same object. Therefore, the correspondence between hadron and calorimeter clusters was determined by calculating and comparing the value of k_{\perp} between each pair of hadron and calorimeter clusters. Equation 4.6 is used to calculate k_{\perp} , except that k_{\perp} is now calculated between two energy clusters, one at the hadron level and one at the detector level. Each hadron cluster is then "matched" with the calorimeter cluster with which it has the lowest value of k_{\perp} .

After all of the cuts described in this and the previous chapter are applied at both the hadron and detector levels, the highest p_T cluster (cluster 1), the second-highest p_T cluster (cluster 2) and the lowest p_T cluster (cluster 3) at the hadron level were matched to the corresponding detector level cluster in 62% of the events. The next most likely configuration (35% of the events) occurs when the two highest p_T clusters are exchanged. This exchange is irrelevant for the corrections to cluster 3 and is easily included in the correction procedure for clusters 1 and 2 by correcting the detector level cluster back to the hadron level cluster to which it corresponds. Therefore, all three clusters are appropriately matched for 97% of the Monte Carlo events. In 3% of the events, a high- p_T cluster at one level was associated with the proton remnant at the other level. In less than 0.5% of the events, the lowest p_T clusters at the hadron and calorimeter levels did not match.

5.3 Measurement Resolutions

Once the hadron level cluster which most closely corresponds to a given detector level cluster has been identified, the detector level resolution can be measured for each cluster. This has been done using both the PYTHIA and HERWIG Monte Carlo simulations. The measurement resolution of the observed quantities in this dissertation are summarized in Table 5.1. There is good agreement between the results from the PYTHIA and HERWIG Monte Carlo generators. All following Monte Carlo results refer to the PYTHIA Monte Carlo generator unless HERWIG is specifically mentioned.

The average measured value of $\eta_{1,2}^{ad}$ is shifted with respect to the hadron

Measured Quantities	PYTHIA Resolution		HERWIG Resolution	
	percent	absolute	percent	absolute
y	22.2 ± 10.0	0.13 ± 0.065	18.9 ± 9.7	0.11 ± 0.065
η_1	1.4 ± 7.7	0.0063 ± 0.061	1.3 ± 6.5	0.005 ± 0.046
η_2	2.5 ± 8.8	0.015 ± 0.07	2.1 ± 7.1	-0.0003 ± 0.06
η_3	5.9 ± 19.2	-0.073 ± 0.42	3.8 ± 16.0	-0.081 ± 0.31
p_{T1}	13.8 ± 10.6	1.4 ± 1.1	13.1 ± 10.5	1.3 ± 1.1
p_{T2}	17.2 ± 10.2	1.1 ± 0.9	15.9 ± 11.7	1.2 ± 1.0
p_{T3}	16.3 ± 33.6	0.17 ± 0.5	17.6 ± 31.5	0.13 ± 0.44
E_1	15.6 ± 12.2	2.3 ± 2.0	13.9 ± 11.1	1.9 ± 1.6
E_2	19.9 ± 12.3	2.4 ± 1.7	16.6 ± 12.7	2.0 ± 1.8
E_3	26.2 ± 18.6	2.2 ± 1.9	21.7 ± 18.2	1.8 ± 1.8
$\langle E_3^{\text{act}} \rangle_1$	-10.2 ± 31.9	-0.038 ± 0.12	2.1 ± 52.6	-0.040 ± 0.13
$\langle E_3^{\text{act}} \rangle_2$	-3.7 ± 36.3	-0.011 ± 0.13	-4.0 ± 16.2	-0.016 ± 0.12
$\langle E_3^{\text{act}} \rangle_3$	11.9 ± 29.2	0.042 ± 0.10	16.7 ± 32.4	-0.016 ± 0.11
$\Sigma_i E_{i1}^-$	8.3 ± 27.3	0.19 ± 1.1	-1.3 ± 42.9	-0.036 ± 0.98
$\Sigma_i E_{i2}^-$	13.6 ± 27.0	0.31 ± 0.95	8.2 ± 33.5	0.18 ± 1.1
$\Sigma_i E_{i3}^-$	21.3 ± 25.8	0.51 ± 0.80	17.7 ± 22.9	0.33 ± 0.63
$\Sigma_i E_{i1}^{\text{act}}$	18.1 ± 11.1	2.2 ± 1.9	15.0 ± 9.4	2.0 ± 1.6
$\Sigma_i E_{i2}^{\text{act}}$	20.3 ± 11.6	2.2 ± 1.5	17.3 ± 11.3	2.0 ± 1.5
$\Sigma_i E_{i3}^{\text{act}}$	26.6 ± 17.2	1.9 ± 1.5	24.7 ± 17.2	1.8 ± 1.8

Table 5.1: Resolution measurements for various experimentally measured quantities. The actual value of y , for example, is 22% larger, on average, than the measured value, y_{th} .

level, by -0.02 units and has a resolution of 0.07 units. The average measured value of η_3^{act} is shifted, with respect to the hadron level, by 0.08 units and has a resolution of 0.43 units. The measured transverse momentum with respect to the beam, $p_{T1,2}^{\text{act}}$, is reduced on average, by 15% and has a resolution of 11% . The value of y is reconstructed with an average shift of -0.14 units and a resolution of 10% . In general, the detector level measurements of energy within the calorimeter, as well as quantities derived from the calorimeter energy, are about 20% smaller than the same quantities measured at the hadron level. This is due primarily to energy loss in inactive material in front of the calorimeter. The inactive material includes the magnetic solenoid, and the beam pipe, as well as various support structures and instrumentation.

On average, the third cluster with $\eta_3^{\text{act}} < -1$ and $E_3^{\text{act}} > 2$ GeV contains $75 \pm 20\%$ of the photon remnant energy, as defined by the third cluster energy at the hadron level. Figure 5.1 shows the energy losses which occur for the third cluster as a function of the third cluster energy. The triangles show the average value of E_3^{act}/E_3^- , as a function of the photon remnant energy at the hadron level, E_3^- . The losses due to the beam pipe are found by removing those hadronic particles whose direction of travel is within the angular region of the beam pipe. After removing those particles, the clustering is redone. Here E_3^- denotes the energy of the third cluster at the hadron level after the particles in the beam pipe region are removed. The quantity E_3^{act}/E_3^- is plotted as the black circles. If the third cluster at the hadron level, after the removal of the beam particles, is no longer in the region $\eta_3 < -1$, then all of the hadron level energy is considered lost. This happens for about 3% of the resolved Monte Carlo events.

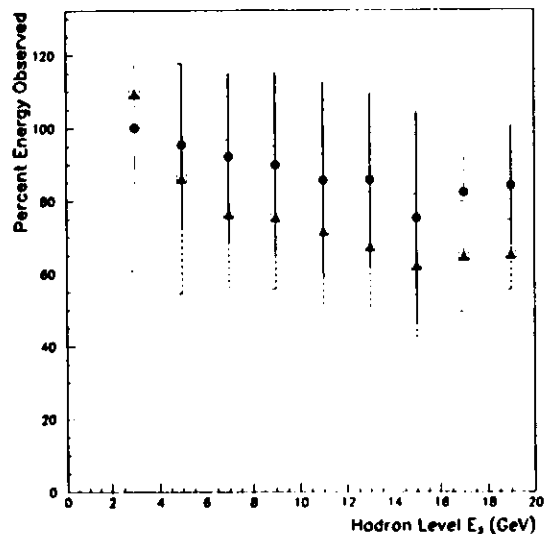


Figure 5.1: Percent hadronic energy observed excluding particles in the angular region of the beam pipe (circles), and percent energy observed in the simulated calorimeter (triangles) as a function of E_3 , the photon remnant energy at the hadron level. The error bars denote the spread of the distribution in each bin, not the error on the mean.

Inactive material in front of the calorimeter results in an energy measurement that is approximately 20% lower than the hadron level energy excluding those particles lost down the beam pipe. This is true for all but the lowest energy bins, where the clustering at the hadron and detector levels are less likely to produce the same object. Particles lost in the beam pipe account for the rest of the energy loss. This effect increases with cluster energy, becoming comparable to the detector effects at measured energies above 10 GeV.

The energy resolution is shown in Fig 5.2. Figure 5.2a shows the correlation between E_3^{cal} and E_3 . Matching between the hadron level and detector level clusters, as described in the previous section, is required. Figure 5.2b shows the resolution in percent ($\frac{E_3 - E_3^{cal}}{E_3} \times 100$) and Fig. 5.2c shows the absolute resolution in GeV ($E_3 - E_3^{cal}$). The figures which correspond to Fig. 5.2 for the other measured quantities listed in Table 5.1 are shown in Appendix A.

5.4 Data Corrections

Two methods have been used to correct the data for detector acceptance and resolution smearing. First, the contamination from events outside the kinematic range was estimated using Monte Carlo events and was subtracted bin-by-bin from the measured distributions. The resulting distributions were then corrected with an unfolding algorithm based on Bayes' Theorem⁴¹ (see section 5.4.2). The corrections include acceptance corrections for the trigger as described in section 4.1 as well as for the selection cuts described in sections 4.2 and 4.4. The corrections also include the effect of particles lost down the beam pipe, which can result in significant event migrations between bins.

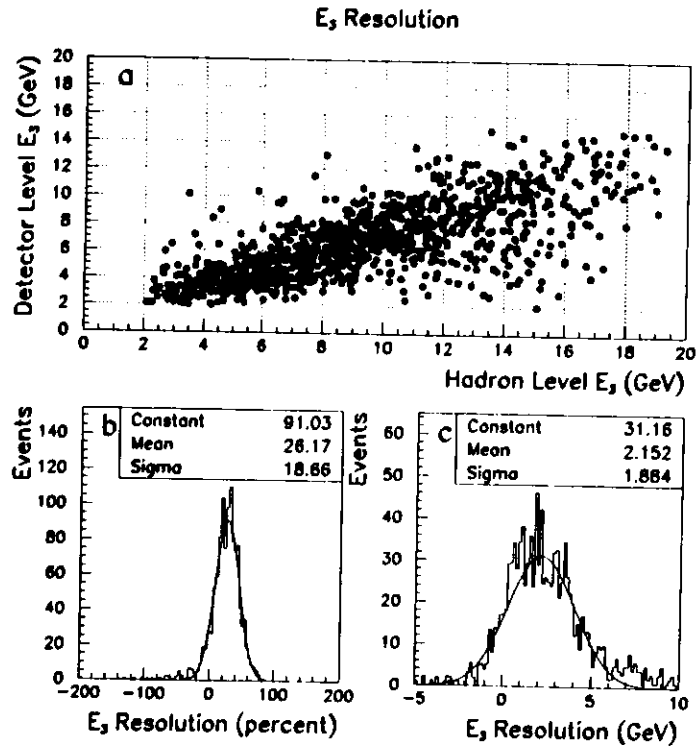


Figure 5.2: Energy resolution of the photon remnant as determined using the PYTHIA Monte Carlo simulation. (a) Correlation between the detector and hadron level photon remnant energy. (b) Energy resolution in percent. (c) Absolute energy resolution in GeV. The constant, mean and sigma in (b) and (c) are determined from the fit.

5.4.1 Bin-By-Bin Corrections

In this analysis, bin-by-bin corrections are used primarily to remove background events which enter the detector level distributions from outside the hadron level kinematic region. This method is also used when it is impractical to use the unfolding procedure (see section 7.2.3). The bin-by-bin correction factors are found by dividing the number of Monte Carlo events falling into each bin of the hadron level distribution by the number of Monte Carlo events falling into the same bin of the detector level variable. Each bin of the data is then multiplied by the corresponding correction factor to determine the hadron level distribution. This method does not take into account migrations from one hadron level bin to different detector level bins.

5.4.2 Bayes' Unfolding

Since the photon remnant tends to deposit energy near the RCAL beam pipe, significant amounts of energy may be lost down the beam pipe. As a result, the migrations between the hadron level and detector level bins can be large. The smearing matrix for the photon remnant energy, obtained from Monte Carlo events, has already been shown in Fig. 5.2a (the smearing matrices for the photon remnant transverse momentum and pseudorapidity are shown in Figs. A.6 and A.3, respectively). Since there are significant migrations between hadron level and detector level bins for these physical variables, an unfolding procedure which takes these migrations into account is more appropriate than bin-by-bin corrections. Therefore, an unfolding algorithm based on Bayes' Theorem was used to correct the data.

Bayes' Theorem states that the probability that an effect, E_j , (such as an event falling into bin j in a detector level distribution) will result from a given cause, C_i , (such as an event originating in bin i of the hadron level distribution) is proportional to the probability of the cause occurring times the probability that the cause will result in the observed effect. For the purpose of unfolding a hadron level distribution from a detector level distribution, Bayes' Theorem can be written as follows:

$$\hat{n}_{k+1}(C_i) = \frac{1}{\epsilon_i} \sum_{j=1}^{bins} n(E_j) P_k(C_i|E_j), \quad (5.1)$$

where $\hat{n}_{k+1}(C_i)$ is the number of entries in bin i of the hadron level distribution, ϵ_i is the efficiency of detecting cause i in any observable effect, $n(E_j)$ is the number of entries in bin j of the detector level distribution, and $P_k(C_i|E_j)$ is the probability that cause i will occur and will result in effect j . $P_k(C_i|E_j)$ is a function of $\hat{n}_k(C_i)$ and the smearing matrix, $S(C_i|E_j)$:

$$P_k(C_i|E_j) = \left(\frac{S(C_i|E_j)}{\sum_j S(C_i|E_j)} \right) \left(\frac{\hat{n}_k(C_i)}{\sum_i \hat{n}_k(C_i)} \right). \quad (5.2)$$

The hadron level distribution is determined by first estimating $\hat{n}_0(C_i)$, such as the hadron level distribution from the Monte Carlo simulation, and calculating $\hat{n}_1(C_i)$ using equation 5.1. The new estimate, $\hat{n}_1(C_i)$, is then used to determine $\hat{n}_2(C_i)$. This procedure is iterated until the change in χ^2 calculated between $\hat{n}_k(C_i)$ and $\hat{n}_{k+1}(C_i)$ is less than 1%. The photon remnant pseudorapidity, transverse momentum and energy are corrected using this method.

5.4.3 Simultaneous Corrections in Two Variables

To correct a distribution such as the energy, it is only necessary to know the detector level and hadron level distributions for that single physical variable.

To correct a measurement such as the average energy transverse to the cluster axis per particle, $\langle E_T^2 \rangle$, as a function of cluster energy (see section 7.2.3), however, it is necessary to do unfolding in two physical variables simultaneously.

Unfolding in two physical variables simultaneously is actually performed in exactly the same way as is unfolding in one physical variable. The difference is in the structure of the detector level and hadron level distributions, and in the structure of the smearing matrix. The process of unfolding in two physical variables simultaneously is illustrated by Fig. 5.3. Figure 5.3a shows the uncorrected data, where the mean value of variable 2 is plotted as a function of variable 1. Figure 5.3b shows the number of entries in bins of variable 2 and variable 1 from which Fig. 5.3a was constructed. Figure 5.3b is plotted again in Fig. 5.3c as a histogram. The first bin in Fig. 5.3c corresponds to the bin in the lower left corner of Fig. 5.3b. The second bin in Fig. 5.3c corresponds to the next bin up (the same bin in variable 1, but the second bin in variable 2). The uncorrected data is shown in Fig. 5.3c and the hadron level Monte Carlo simulation is shown in Fig. 5.3d. The smearing matrix (Fig. 5.4a) is determined using the correlation between the detector level Monte Carlo distribution (Monte Carlo equivalent of Fig. 5.3c) and the hadron level Monte Carlo distribution shown in Fig. 5.3d. The unfolding procedure is then performed in the same way as for a single variable using the uncorrected data of Fig. 5.3c and the smearing matrix of Fig. 5.4a. The resulting corrected distribution (Fig. 5.4b) is then used to reconstruct the correlation between the corrected variables (Fig. 5.4c). Finally, the corrected mean value of variable 2 is plotted as a function of the corrected value of variable 1 (Fig. 5.4d).

The quantities $\langle E_T^2 \rangle$, $\Sigma_i E_i^2$ and $\Sigma_i E_i^2$ are corrected as a function of the

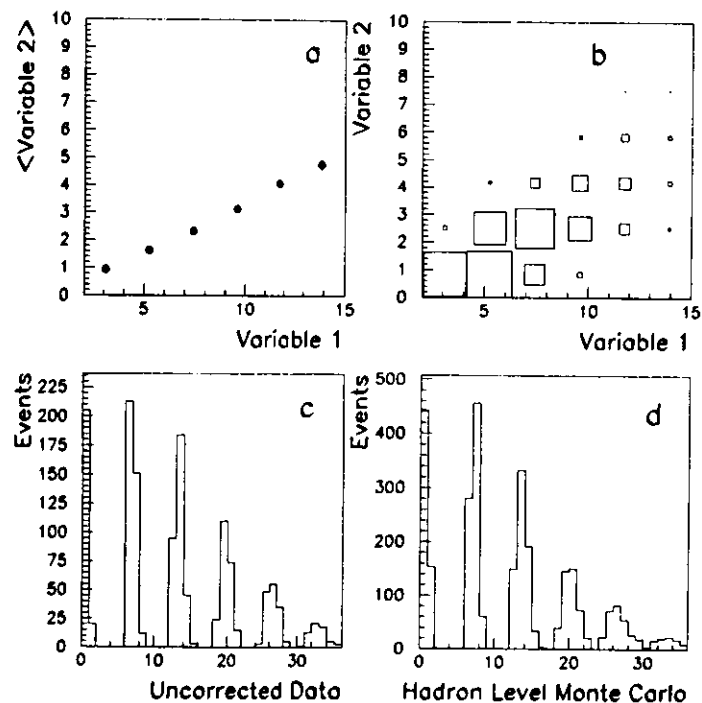


Figure 5.3: Data corrections in two physical variables are carried out as illustrated above and in Fig. 5.4. First a distribution in two variables (a) is drawn as a box plot (b). Each energy bin in (b) is then plotted as a histogram in (c). The hadron level distribution analogous to (c) is shown in (d).

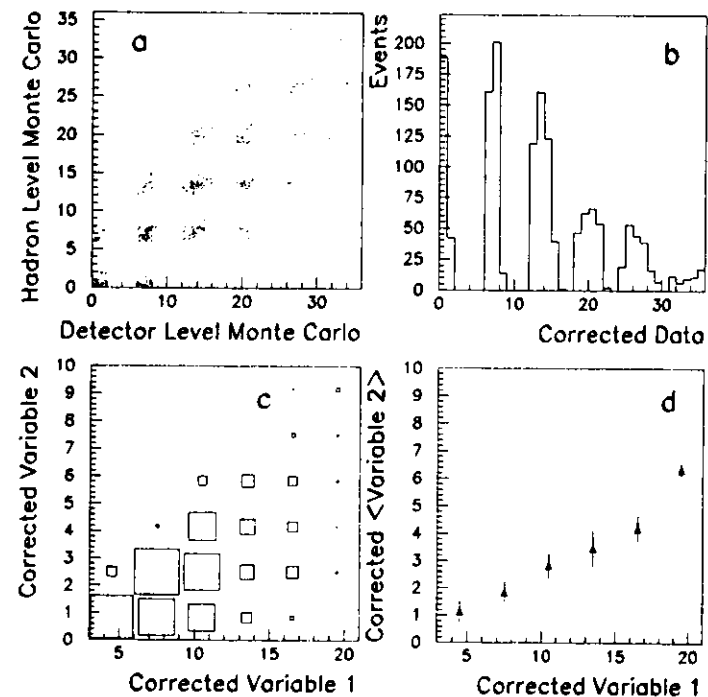


Figure 5.4: Data corrections in two physical variables are carried out as illustrated above and in Fig. 5.3. The correlation (smearing matrix) between the detector and hadron level is plotted in (a). The data are then corrected in the same manner as before resulting in (b). The corrected distribution is then reconstructed (c) and (d).

remnant energy, E_3 , using this method. The quantities are corrected in thirty-six bins, corresponding to six bins in E_3 and six bins in the other variable.

Chapter 6

Measurement Uncertainties

6.1 Statistical Errors

For the variables corrected bin-by-bin, the calculation of the statistical uncertainty is straightforward. The statistical errors for both the uncorrected data and the Monte Carlo distributions are calculated as the root mean squared deviation from the mean in each bin. The statistical uncertainties of the corrected data are then determined using standard error propagation calculations. However, most of the data are corrected using the Bayes' algorithm described in section 5.4.2. The calculation of the statistical uncertainties, including the effects of bin to bin migrations in an iterative unfolding procedure, is a difficult problem. The unfolding algorithm based on Bayes' Theorem does include a feature to calculate the statistical errors. It cannot correctly calculate the statistical uncertainties when background events are subtracted before beginning the unfolding procedure. Therefore, the statistical uncertainties are determined as described below.

6.1.1 Corrections in One Variable

When the data are corrected for smearing in a single variable using the unfolding procedure, the statistical errors, which include the effects of bin migrations, are calculated by varying the data (before background subtraction) and the Monte Carlo smearing matrix within their statistical errors and measuring the effect on the corrected distribution. This is done because the corrected distribution depends only on the detector level (measured) data and on the Monte Carlo smearing matrix (see section 5.1.2).

To vary the data and the Monte Carlo smearing matrix, a (pseudo)random number generator is used. The random number generator generates random numbers according to a Gaussian distribution with mean value, x , and variance, σ^2 . Each bin in the data and in the Monte Carlo smearing matrix is varied separately by setting both x and σ^2 equal to the number of entries in the bin. A random number is generated, within the statistical errors on x . This number taken as the new number of entries in the bin. In this calculation, a Gaussian distribution is always assumed. Technically, a Poisson distribution is more appropriate for bins which contain fewer than about 5 entries,¹² which can occur in the smearing matrices. The Gaussian uncertainty, however, is a relatively good estimate of the Poisson uncertainty for fewer events as well. The number of events in each bin is always greater than or equal to zero, and the variance is always greater than or equal to one. After the number of entries in each bin has been varied, the unfolding procedure is carried out to produce a corrected distribution which is smeared within the statistical errors. This procedure is repeated one hundred times to produce one hundred different corrected distributions, whose only difference is a variation within the statistical

errors in each bin. The statistical errors are then calculated from the root mean squared deviation in each bin of the one hundred corrected values.

To demonstrate that one hundred different corrected distributions are sufficient to obtain a good estimate of the size of the error bars, the calculated size of the error bars is shown in Fig. 6.1 as a function of the number of corrected distributions used in their determination. The six figures shown correspond to each of the six bins of the E_3 distribution. The dotted line indicates the size of the error bars found using one thousand corrected distributions. When the number of corrected distributions used is small, the error bars tend to be large. As the number of corrected distributions increases, the size of the error bars converges rapidly, leveling off near eighty corrected distributions. The size of the error bars found using one hundred corrected distributions tends to be greater than or equal to the size of the error bars found using one thousand corrected distributions. In addition, the error bars calculated using this method are also significantly larger than the error bars given by the unfolding algorithm for test distributions where no background subtraction is performed. Therefore, this method is adequate in estimating the statistical uncertainties.

6.1.2 Corrections in Two Variables

Calculating the statistical uncertainties when the data are corrected in two physical variables simultaneously (as described in section 5.1.3) requires another calculation in addition to those described above. When the data are corrected for smearing in two physical variables simultaneously, the mean value of one variable is plotted as a function of the other variable. An additional calculation is needed to determine the statistical uncertainties on the mean

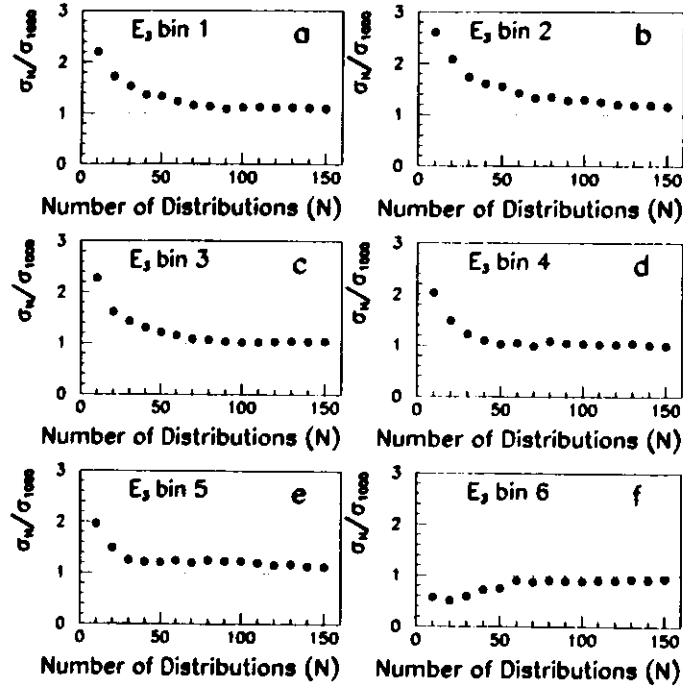


Figure 6.1: Relative size of the statistical uncertainty for the six E_3 bins as a function of the number of corrected distributions used in their determination. The dotted line indicates the size of the statistical uncertainty found using one thousand corrected distributions.

value. In Fig. 5.4b, for example, the six distributions correspond to the total transverse energy ($\Sigma_i E_T^i$) distribution in each energy bin. The statistical uncertainties in each bin of the six distributions are calculated by varying the data and the Monte Carlo smearing matrix as described in the previous section (the error bars are not shown). The statistical uncertainties on the mean value of each of the six distributions are then calculated from:

$$\sigma_{stat} = \frac{\sqrt{\sum_j \sigma_j^2 (x_j - h)^2 + N_j^2 b^2 / 12}}{\sum_j N_j}, \quad (6.1)$$

where the sum is over the six bins, j , in each energy bin and σ_j is the statistical error on each bin, as calculated using one hundred corrected distributions (as described in the previous section). The quantity x_j is the position of the center of bin j , h is the mean value of the distribution in the energy bin, N_j is the number of events in bin j , and b is the width of each bin. In equation 6.1, the first term in the summation corresponds to the root mean squared deviation in each bin. The second term accounts for the finite bin size. An example of this calculation is shown in Fig. 6.2. In Fig. 6.2, the mean value, h (shown

j	1	2	3	4	5	6
N_j	1.0	10.0	17.0	24.0	13.0	4.0
σ_j	1.0	7.0	11.0	19.0	12.0	3.0
x_j	0.5	1.5	2.5	3.5	4.5	5.5

Table 6.1: Example values used in calculating the error on the mean. In Fig. 6.2 $h = 3.225$ and $b = 1.0$. Therefore $\sigma_{stat} = 0.36$.

as the closed circle), is 3.225, and the bin width, b , is 1.0. The rest of the numbers used in the calculation of σ_{stat} for Fig. 6.2 are shown in table 6.1. The calculated uncertainty in the mean value of σ_{stat} is 0.36. Even with large

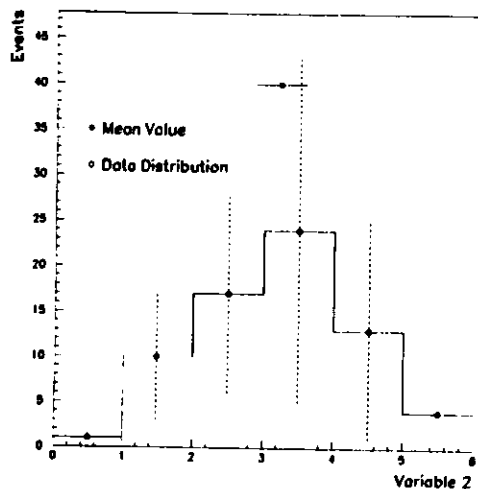


Figure 6.2: Example of a calculation of the error on the mean for a distribution. The histogram shows the distribution of variable 2 in a single bin of variable 1, as described in section 5.4.3.

statistical uncertainties in each bin, the error on the mean is relatively small.

6.2 Independent Confirmation

Two independent analysis were performed in order to check the consistency of the results.⁴³ The analysis described in this dissertation will be referred to as Analysis A. The other analysis will be referred to as Analysis B. The trigger requirements for both analyses are identical and are described in section 4.1. The cuts applied off line (see section 4.2) are done separately for

the two analyses, but the quantities the cuts are applied to (y_{jB} , for example) are calculated in the same way. Both analyses use the same electron finding routine, and the k_{\perp} algorithm is used in both analyses. Both analyses require three clusters to be found in each event. After applying selection cuts identical to those described in section 4.1, 1370 (Analysis A) and 1402 (Analysis B) events are selected. The integrated luminosities used in the two analyses are slightly different because slightly different initial event samples were used. Therefore, the final samples contain slightly different numbers of events. The selected events are the same when a common data sample is used. The Monte Carlo event sample was also different for the two analyses. In both analyses, the data are corrected using the unfolding algorithm based on Bayes' Theorem described in section 5.4.2. The same detector level and hadron level binning is used in both analyses.

Figure 6.3 compares the uncorrected pseudorapidity distributions of the two analyses. The pseudorapidity distributions on the left (Fig. 6.3a,c,e and g) are from Analysis A. They are identical to the distributions shown in Figs. 4.1 and 4.2. The pseudorapidity distributions on the right (Fig. 6.3b,d,f and h) are from Analysis B. Figure 6.3a and b are the highest p_T^{cal} cluster, c and d are the second highest p_T^{cal} cluster, and e and f are the lowest p_T^{cal} cluster. Figure 6.3g and h are the lowest p_T^{cal} cluster after requiring $p_{T1,2}^{cal} > 5$ GeV and $\eta_{1,2}^{cal} < 1.6$. The two analyses are in excellent agreement.

A full comparison between the two analyses with the corrected data is presented in section 7.3. The differences between the two independent analyses are also included in the calculation of the systematic uncertainties which are discussed in the next section.

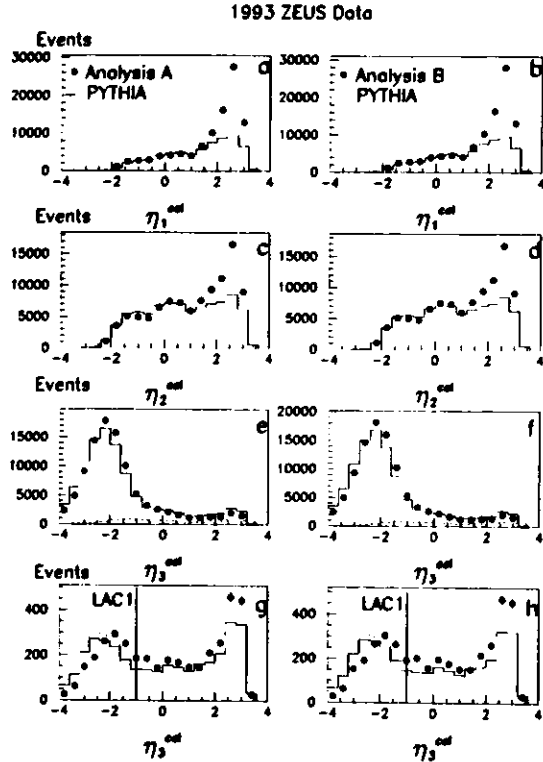


Figure 6.3: Comparison between Analysis A ((a),(c),(e) and (g)) and Analysis B ((b),(d),(f) and (h)) for the uncorrected pseudorapidity distributions. (a) and (b): The highest p_T^{cal} cluster. (c) and (d): The second highest p_T^{cal} cluster. (e) and (f): The lowest p_T^{cal} cluster. (g) and (h): The lowest p_T^{cal} cluster after requiring $p_T^{\text{cal}} > 5 \text{ GeV}$ and $\eta_{1,2}^{\text{cal}} < 1.6$.

6.3 Systematic Uncertainties

To estimate the systematic uncertainties, the analysis is repeated with a variety of modifications described below and summarized in table 6.2. The variation of each of these different results is then used to determine the size of the systematic errors. Figure 6.4 shows the systematic fluctuations in the measurement of η_3 , E_3 and p_{T3} . The fluctuations are measured in percent. The error bars denote the size of the statistical errors. The x axis is in units of p_{T3} , η_3 and E_3 respectively. There are seven p_{T3} bins, eight η_3 bins, and six E_3 bins with eleven points apiece showing the systematic fluctuations. The leftmost point in each bin corresponds to the corrected data point shown in the next chapter (analysis A). The next point to the right is from analysis B. The third point is corrected using an expanded y_{JB} range for the data and reconstructed Monte Carlo ($0.15 < y_{JB} < 0.85$). The fourth point is corrected using a relaxed p_T cut on the two highest p_T jets ($p_{T1,2}^{\text{cal}} > 1.5 \text{ GeV}$). The fifth point is corrected using a relaxed η^{cal} range for jets 1 and 2 of $\eta_{1,2}^{\text{cal}} < 1.8$. The sixth point is corrected after relaxing the η_3^{cal} cut to $\eta_3^{\text{cal}} < -0.8$ (in the η_3 plot this cut is not applied so the point is set to zero). The seventh point is generated using a factor of 3 more direct events than expected. For the eighth point the events are reweighted using the LACI photon-parton parameterization. The ninth point is corrected using Monte Carlo events where the calorimeter energies were all increased by 5%. The tenth point is corrected using HERWIG. The eleventh point shows the analysis redone using clusters made up of calorimeter islands (see section 6.1) instead of cells (except in the case of $\langle E_T^2 \rangle$). This information is summarized in Table 6.2.

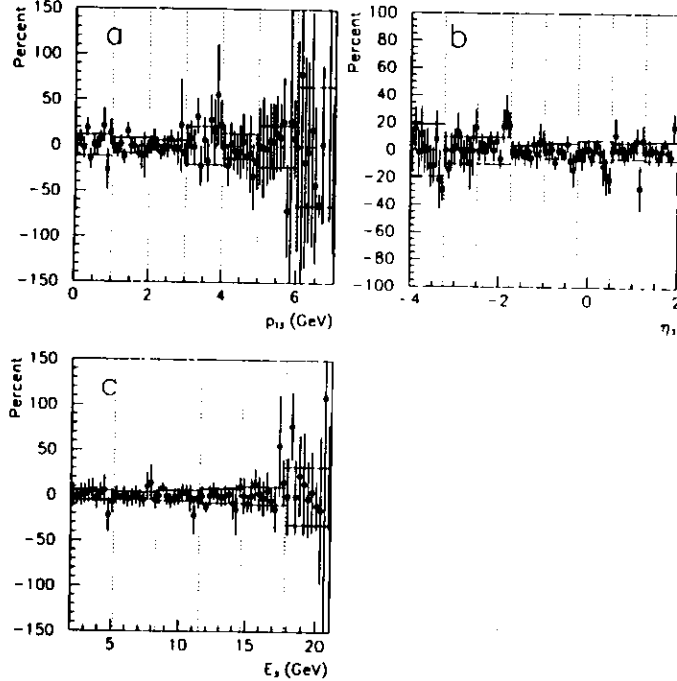


Figure 6.1: Percent systematic fluctuations in measurements of (a) p_{T3} , (b) η_3 and (c) E_3 as described in table 6.7. The error bars on the points are the statistical errors. The horizontal lines indicate the size of the systematic uncertainties calculated in each bin. In (b), the fifth point is identically zero since the η_3^{cut} cut was not applied for this measurement. Therefore, the fifth point is not included in the calculation of the systematic errors.

Data Point	Modification	Excludes
1	None	
2	Analysis A \rightarrow Analysis B	
3	$0.20 < y_{JB} < 0.70 \rightarrow 0.15 < y_{JB} < 0.85$	
4	$p_{T1,2}^{cal} > 5.0 \text{ GeV} \rightarrow p_{T1,2}^{cal} > 4.5 \text{ GeV}$	
5	$\eta_{1,2}^{cal} < 1.6 \rightarrow \eta_{1,2}^{cal} < 1.8$	
6	$\eta_3^{cal} < -1.0 \rightarrow \eta_3^{cal} < -0.8$	η_3
7	Direct \rightarrow $3 \times$ Direct	
8	GRV LO \rightarrow LAC1	
9	Monte Carlo cell energies increased by 5%	
10	PYTHIA \rightarrow HERWIG	
11	Cells \leftrightarrow Islands	$\langle E_T^3 \rangle$

Table 6.2: List of systematic checks included in the calculation of the systematic error bars in figures 6.4 through 6.7.

The systematic errors, σ_{sys} , denoted by the horizontal lines in Fig. 6.1, are calculated from the formula:

$$\sigma_{sys} = \sqrt{\frac{\sum_{i=2}^{11} \frac{1}{\sigma_i^2} (d_i - d_1)^2}{\sum_{i=2}^{11} \frac{1}{\sigma_i^2}}}, \quad (6.2)$$

where d_i is the percent difference shown in the figure for point i ($d_1 \equiv 0$), and σ_i is the statistical error on the data point. The sum is over all points, excluding the first point, as well as those points for which the systematic study cannot be done (the exceptions are noted in table 6.2).

In general, the systematic variations are approximately of the same size as the statistical uncertainties. Switching from PYTHIA to HERWIG produces the largest systematic variations. However, HERWIG also has larger statistical uncertainties.

Figure 6.5 shows the systematic fluctuations in the measurement of $\langle E_T^3 \rangle$ (as calculated using both calorimeter islands and calorimeter cells, see next

section). Excluding the rightmost point in each bin, which is discussed in the next section, the agreement between the various systematic variations is good. Figure 6.6 shows the systematic fluctuations in the measurements of $\Sigma_i E_{iL}^{\pm}$ and $\Sigma_i E_{iT}^{\pm}$. The systematic uncertainties in the calculation of $\Sigma_i E_{iL}^{\pm}$ are small in comparison to the statistical uncertainties. This is due to the relatively large bin size (3 GeV) along the $\Sigma_i E_{iL}^{\pm}$ axis. The systematic fluctuations in $\Sigma_i E_{iT}^{\pm}$ are also comparable to the statistical uncertainties. Figure 6.7 shows the systematic fluctuations in the energy flow measurements. Again, the agreement is rather good, with the exception of the points found using HERWIG. HERWIG tends to produce somewhat broader jets than PYTHIA.

6.4 Islands and Cells

Since there was no tracking in the rear direction in 1993, the measurement of the transverse energy per particle, $\langle E_T^{\pm} \rangle$, was done using "islands" of calorimeter cells. Calorimeter islands are found by calculating the energy deposited in each calorimeter tower (see section 2.2.1). Towers which have more energy than any neighboring towers (side by side, or corner to corner) are defined as local maxima. Calorimeter cells in towers which neighbor a local maxima are then assigned to that local maxima. If one tower neighbors two local maxima, its cells are assigned to the local maxima with the greatest energy.⁴⁴ In general, there are about three calorimeter cells per island. Figure 6.8 shows the average number of final-state hadronic particles generated in the Monte Carlo per island measured in the simulated calorimeter as a function of pseudorapidity. The black circles are calculated using only the events which passed the

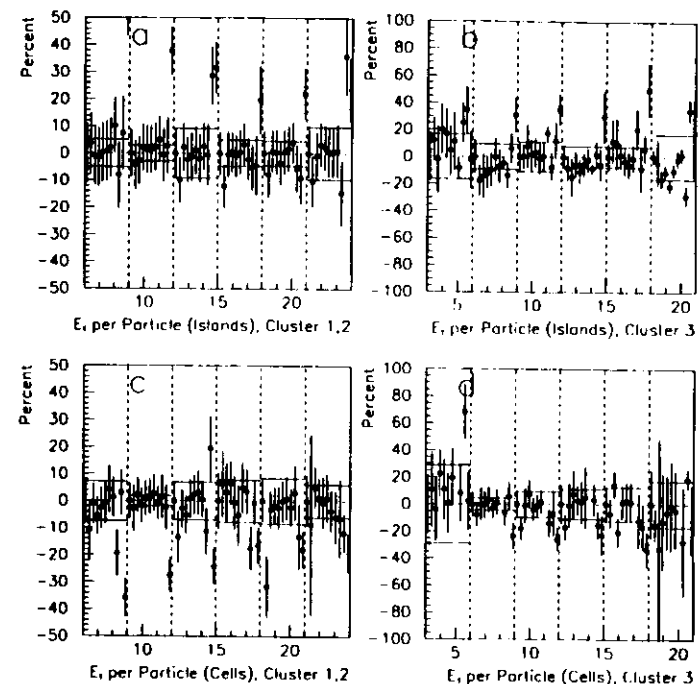


Figure 6.5: Systematic effect on the $\langle E_T^{\pm} \rangle$ distribution determined by varying the cuts as described in Table 6.2. In (a) and (b) all points are calculated using calorimeter islands excluding the rightmost point in each bin, which is calculated using calorimeter cells. In (c) and (d) all points are calculated using calorimeter cells excluding the rightmost point in each bin, which is calculated using calorimeter islands.

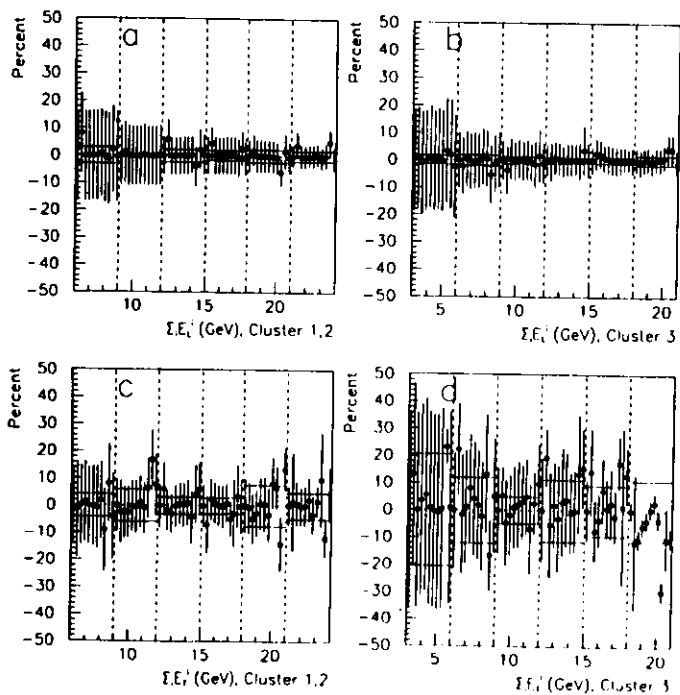


Figure 6.6: Systematic errors for (a) $\Sigma_i E_L^i$ for clusters 1 and 2, (b) $\Sigma_i E_L^i$ for cluster 3, (c) $\Sigma_i E_T^i$ for clusters 1 and 2, (d) $\Sigma_i E_T^i$ for cluster 3.

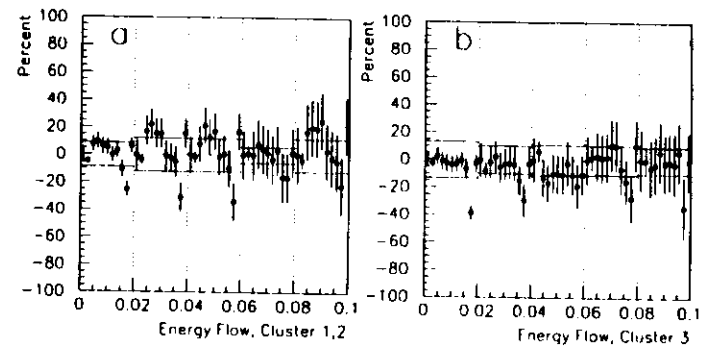


Figure 6.7: Systematic errors on the energy flow for (a) clusters 1 and 2 and (b) cluster 3.

cuts. The open circles correspond to all events generated. On average, there is a good correspondence between particles and islands in the η region between -3 and 2 . Therefore, islands may be roughly associated with particles. There are, on the other hand, generally three times as many cells as there are particles. For this reason, islands were used in the calculation of $\langle E_T^i \rangle$, instead of calorimeter cells.

Calorimeter cells, however, were used to check the results of the $\langle E_T^i \rangle$ calculation. When this was done, a significant discrepancy was found between the $\langle E_T^i \rangle$ values found using calorimeter cells and those found using calorimeter islands. This discrepancy can best be seen in Fig. 6.5. In Fig. 6.5a and b, all of the points were calculated using calorimeter islands, except for the rightmost point in each bin. The rightmost point was calculated using calorimeter cells

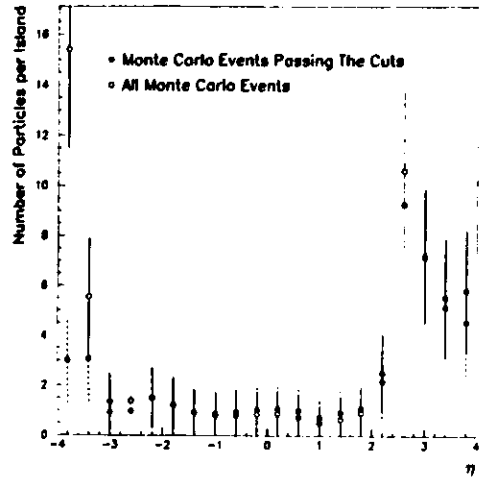


Figure 6.8: Number of particles per island as a function of pseudorapidity. The open circles include all generated events, while the closed circles include only those events which passed the cuts described in Chapter 4

and tends to be much higher in all bins. In Fig 6.5c and d, the points were all calculated using calorimeter cells, except for the rightmost point, which was calculated using calorimeter islands. Here the rightmost point tends to be low. Because of this difference, the rightmost point was included separately in the systematic errors. The difference between the points calculated using calorimeter cells and calorimeter islands in each bin is added in quadrature to the upper systematic error bars of the corrected total transverse energy per particle ($\langle E_T^i \rangle$) data (see section 7.2.3).

The disagreement between the $\langle E_T^i \rangle$ values found using calorimeter cells

and calorimeter islands is caused by a less than adequate Monte Carlo description of the calorimeter cell energies (see next section).

Since the calculation of $\langle E_T^i \rangle$ varies depending on whether calorimeter cells or calorimeter islands are used, it is interesting to compare the average number of calorimeter islands per cluster as a function of the number of calorimeter cells in the cluster. This is shown in Fig. 6.9. There tend to be fewer calorime-

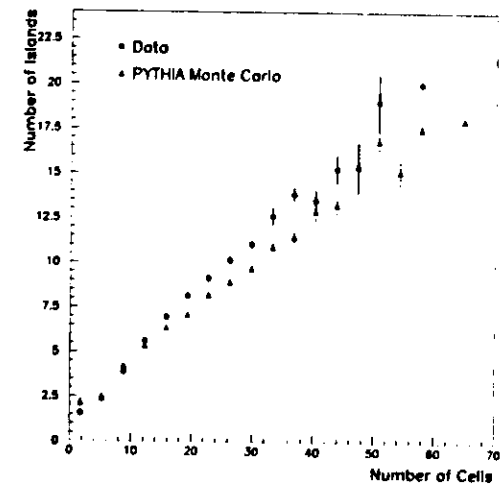


Figure 6.9: Number of calorimeter islands in the lowest p_T^{cal} cluster as a function of the number of calorimeter cells.

ter islands for the same number of calorimeter cells in the Monte Carlo simulation. In figure 6.10 the average number of (a) calorimeter islands and (b) calorimeter cells per cluster as a function of the energy of the cluster is shown for the third cluster. The Monte Carlo tends to have more calorimeter cells at

all energies, but fewer calorimeter islands. This is also true for clusters 1 and 2 (not shown). These differences result in large systematic uncertainties between the data corrected using calorimeter cells and the data corrected using calorimeter islands, as described above.

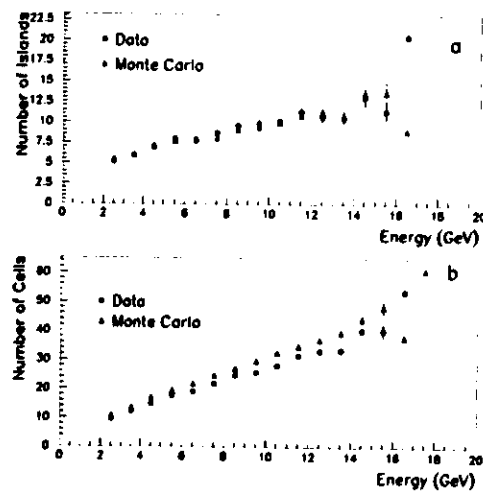


Figure 6.10: Number of calorimeter islands (a) and calorimeter cells (b) in the lowest p_T^{cal} cluster as a function of the cluster energy for both the data and the Monte Carlo simulation.

6.5 Noise Suppression

One possible explanation for the differences in the number of calorimeter cells and calorimeter islands is calorimeter noise. If there is calorimeter noise above the minimum energy threshold (60 MeV for EMC and 110 MeV for HAC cells),

which is not included in the Monte Carlo simulation, then there will be more isolated calorimeter cells and therefore more calorimeter islands (made up of single cells) as well. The removal of this noise would reduce both the number of calorimeter cells and the number of calorimeter islands. Since there are fewer calorimeter islands than calorimeter cells in each cluster, removing the isolated calorimeter cells would result in a proportionately larger reduction in the number of calorimeter islands than in the number of calorimeter cells. This might bring the two calculations of $\langle E_T \rangle$ into better agreement.

For the data shown up to this point, calorimeter noise is removed by the minimum energy thresholds of 60 MeV for EMC cells and 110 MeV for HAC cells. For the following study, additional calorimeter noise was removed using the noise suppression algorithm.⁴⁴ This algorithm removes single calorimeter cells which are isolated, and have an energy below 80 MeV for EMC cells and below 140 MeV for HAC cells. A cell is considered isolated if none of the calorimeter cells with which it shares a common edge are active.

The effect of the noise suppression is shown in Fig. 6.11. The event selection criteria are the same as those described in section 4.4. All calorimeter cells are included in the study. The calorimeter cell energy distribution for the data is shown before and after noise suppression in Fig. 6.11a. Noise suppression has the largest effect at low energies. The same plot for the PYTHIA Monte Carlo simulation is shown in Fig. 6.11b. The Monte Carlo distribution shows the same trend as the data, although fewer calorimeter cells are removed. Figure 6.11c shows the data and the Monte Carlo simulation together, after noise suppression. The data and the Monte Carlo simulation still do not agree. In fact, the disagreement extends well beyond the region which is significantly

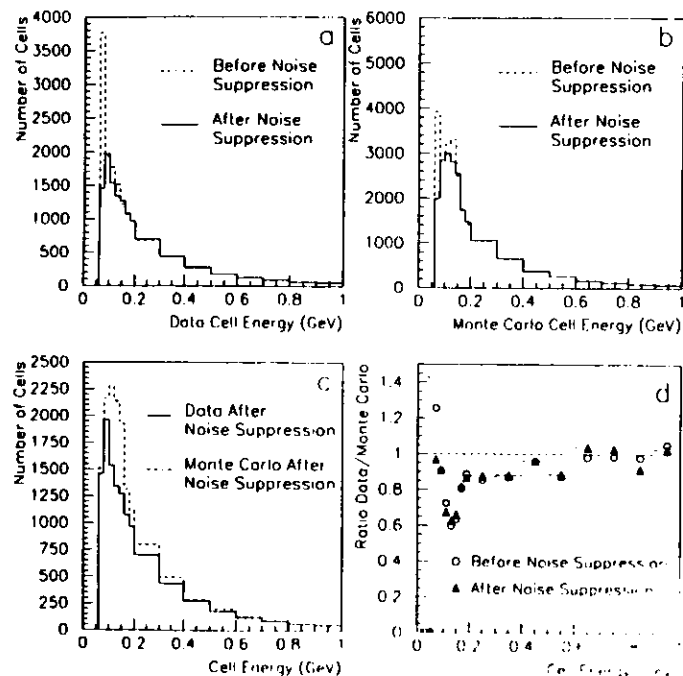


Figure 6.11: *Calorimeter Cell Energies.* (a) Calorimeter cell energies for the data before and after applying the noise suppression algorithm. (b) Monte Carlo calorimeter cell energies before and after applying the noise suppression algorithm. (c) Comparison between the data and the Monte Carlo calorimeter cell energies after applying the noise suppression algorithm. (d) Number of calorimeter cells with a given energy in the data divided by the number of calorimeter cells with the same energy in the Monte Carlo simulation.

affected by the noise suppression algorithm. Figure 6.11d shows the number of calorimeter cells in the data divided by the number of calorimeter cells in the Monte Carlo simulation as a function of the calorimeter cell energy. This ratio is shown both with and without noise suppression. The ratio differs only in the first few bins. Above 140 MeV, which is the noise suppression threshold, the ratio rises with calorimeter cell energy and, of course, is not influenced by noise suppression. In addition, the discrepancy between the data and the Monte Carlo simulation, shown in Fig. 6.10 before noise suppression, is still present after noise suppression (not shown). Clearly, the calorimeter cell energies are not well described by the Monte Carlo simulation. This results in the differences between the number of calorimeter cells and calorimeter islands in the data and in the Monte Carlo simulation. Since noise suppression did not improve the agreement between the data and the Monte Carlo simulation, it was not used in this analysis.

6.6 Inactive Material

Since the conclusions of this dissertation rely on energy measurements around the RCAL beam pipe, it is important to consider what effect an incorrect description of the Monte Carlo calorimeter energy response in this region would have on the conclusions. One factor which could influence the Monte Carlo description of the calorimeter energy response is inactive material. If the Monte Carlo simulation does not include the correct amount of inactive material then the Monte Carlo simulation will overestimate the energy deposited in the calorimeter.

There is evidence that the Monte Carlo description of the detector is incomplete around the RCAL beam pipe. The average electron energy in DIS data events in the 1993 sample, for example, was about 5% lower than the Monte Carlo events.⁴⁵ A study with the small rear tracking detector (SRTD), with 1994 data, showed that the energy deposited in the SRTD is larger than that predicted by the Monte Carlo simulation.⁴⁶ This indicates that the electron shower is beginning earlier than predicted by the Monte Carlo simulation, probably as a result of additional inactive material in front of the calorimeter which is not included in the Monte Carlo simulation. The data and the Monte Carlo simulation can be brought into agreement by correcting the electron energy using the information from the SRTD. These results suggest that some inactive material around the rear beam pipe is missing from the Monte Carlo simulation. Therefore, it is likely that the simulated calorimeter energy response is too large.

Since the SRTD was not operational in 1993, it cannot be used to make corrections. The DIS electron energy corrections cannot be used either, since the photon remnant is a hadronic object. The effect of missing inactive material in the Monte Carlo simulation, however, can be approximated by reducing the measured calorimeter energy in the rear direction.

Two methods are used:

- **Method A:** The calorimeter cell energies within 10° of the rear beam pipe were reduced by 10% in the Monte Carlo simulation.
- **Method B:** All calorimeter cell energies in the Monte Carlo simulation were set to zero within 10° of the rear beam pipe direction.

In both methods, the correct (not reduced or zeroed) calorimeter cell energies were used for electron finding, since the electron energy is known to be correct to within 4%.⁴⁵ Figure 6.12 shows the results of Method A and Method B as compared to the conventional PYTHIA Monte Carlo simulation and to the ZEUS data. All figures are presented at the detector level. The standard cuts from section 4.4 are applied except in figs. 6.12a and 6.13a, where no requirements are made on the energy or position of the third cluster. The Monte Carlo event samples are the same and the distributions are not normalized to the number of events in the data, so that the effect of the two methods can be seen. Instead, the number of events in the data is normalized to the number of events in the standard PYTHIA Monte Carlo.

In Fig. 6.12a, the p_{T3}^{cut} distribution of the third cluster is shown. There is no significant difference between the conventional Monte Carlo simulation and the Monte Carlo simulation using Method A. In fact, even when Method B is used in the Monte Carlo simulation, the data still has higher transverse momentum than the Monte Carlo simulation does. The transverse momentum of the third cluster in the rear direction cannot be explained even by excluding all calorimeter cells within 10° of the RCAL beam pipe.

Figure 6.12b shows the η_3^{cut} distribution of the third cluster. Again, the Monte Carlo simulation with Method A is essentially indistinguishable from the conventional Monte Carlo simulation. The Monte Carlo simulation using Method B, however, is actually in relatively good agreement with the data. The energy distribution of the third cluster is shown in Fig. 6.12c. A slight difference between the standard and Method A Monte Carlo simulations is apparent in the lowest energy bin. Of course, the Monte Carlo simulations with

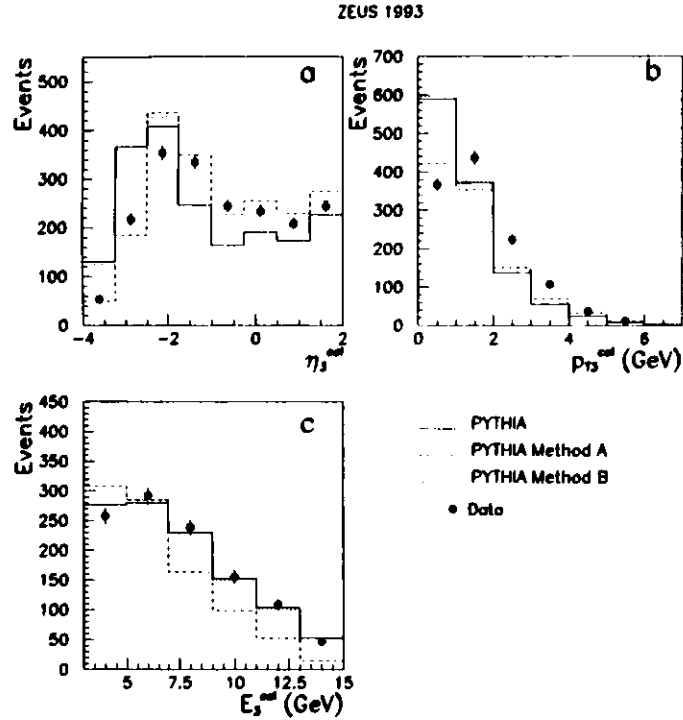


Figure 6.12: Comparison between the (uncorrected) data and the PYTHIA Monte Carlo simulation. The η_3^{cal} (a), p_{T3}^{cal} (b) and E_3^{cal} (c) distributions are shown for the cases when the energy within a 10° cone in the rear direction is reduced, in the Monte Carlo simulation, by 0 (solid line), 10 (dashed line-Method A) and 100% (dotted line-Method B).

reduced energies in the rear direction will have more events at lower energy. However, the Monte Carlo simulation with Method B is completely incompatible with the data. However, both methods A and B are very unlikely. The energies near the beam pipe are not zeroed, and it is quite unlikely that the description of the detector near the RCAL beam pipe in the Monte Carlo simulation is wrong by even 10% as assumed in Method A. Therefore, it is very unlikely that the differences between the η_3^{cal} and p_{T3}^{cal} distributions in the data and in the PYTHIA Monte Carlo simulation are due to an incorrect Monte Carlo description of the detector around the RCAL beam pipe.

Method B can also be used to determine whether or not the data and the Monte Carlo simulation would agree if the calorimeter was completely inactive within 10° of the RCAL beam pipe. In Fig. 6.13, Method B was applied to both the data and to the Monte Carlo simulation. Figure 6.13a shows the p_{T3}^{cal} distribution. The average value of p_{T3}^{cal} is still larger in the data than it is in the Monte Carlo simulation. In Fig. 6.13b the η_3^{cal} distribution is shown. Again, the data is significantly different from the Monte Carlo simulation, indicating that inactive material in the rear direction is not responsible for the discrepancy between the data and the Monte Carlo simulation.

6.7 Y_{cut} studies

While cone algorithms search for energy within a cone in $\eta-\phi$ space, clustering algorithms isolate energy deposits based on some measure of the “distance” between them. This “distance” is generally described by a dimensionless number, Y ($Y = k_\perp/E_T^2$, see section 4.3). Clustering has traditionally been done

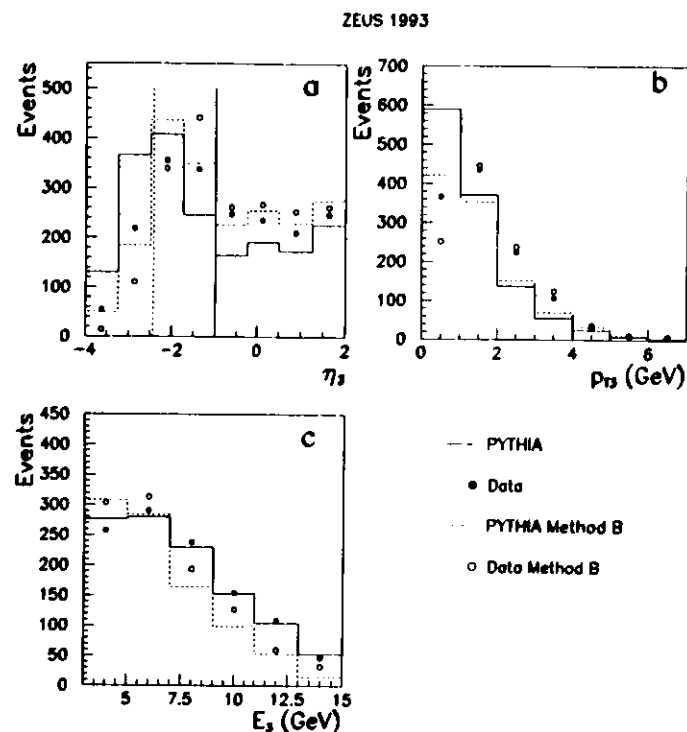


Figure 6.13: Comparison between the uncorrected data and the PYTHIA Monte Carlo simulation. The η_3^{cal} (a), p_{T3}^{cal} (b) and E_3^{cal} (c) distributions are shown as in Fig. 6.12 except that in this case, Method A is not shown, and Method B is applied to both the data and the Monte Carlo simulation to compare the data outside of the 10° cone in the rear direction. For Method B, all calorimeter cell energies are set to zero to the left of the dashed vertical line in (a) near $\eta_3^{\text{cal}} = -2.5$.

by choosing some value, Y_{cut} , beyond which no further clustering is done. The value chosen for Y_{cut} determines the number of clusters which are found. Alternatively, one may fix the number clusters to be found. The value of Y_{cut} , then, varies on an event-by-event basis. In this case, for any one event, a value of Y_{cut} can be chosen which is in the Y range which will result in the requested number of clusters being found. When the number of clusters to be found is fixed, the k_{\perp} algorithm sets Y_{cut} at the smallest value of Y which produces the requested number of clusters. In this analysis, the number of clusters found by the k_{\perp} algorithm is fixed at three, in addition to the proton remnant.

It is instructive to look at the value of Y_{cut} determined for direct and resolved events. The larger the value of Y when three clusters are found (Y_{cut}), the clearer the separation between the three clusters. Figure 6.14a shows the value of Y_{cut} when three clusters are found for the resolved (solid histogram) and direct (dashed histogram) Monte Carlo events. The events are required to have $\eta_{1,2}^{\text{cal}} < 1.6$ and $p_{T1,2}^{\text{cal}} > 5$ GeV. The value of Y_{cut} tends to be smaller for direct events than it is for resolved events because direct events lack a third cluster in the rear direction. The third cluster found in direct events is generally made up either of part of one of the two high p_T jets, or of part of the proton remnant. Therefore, the "distance" between three clusters in direct events tends to be smaller than for resolved events, which have a well separated energy deposit in the rear direction.

Figure 6.14b shows the distribution of Y_{cut} for the data with $\eta_3^{\text{cal}} < -1$ (full circles) and $\eta_3^{\text{cal}} > -1$ (open circles). The histograms are the Monte Carlo expectations for the events with $\eta_3^{\text{cal}} < -1$ (solid) and $\eta_3^{\text{cal}} > -1$ (dashed). The

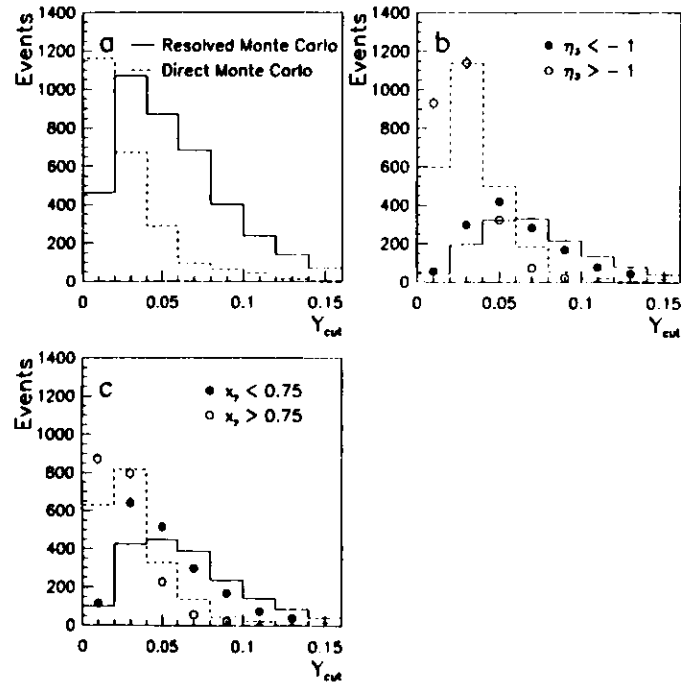


Figure 6.11: Comparison between the Y_{cut} distributions for different definitions of resolved and direct events. (a) Y_{cut} distribution of Leading order resolved and direct Monte Carlo events. (b) Y_{cut} distributions for resolved and direct events defined by the value of η_3^{atl} . (c) Y_{cut} distributions for resolved and direct events defined by the value of x_3^{conr} (see section 4.5). For all figures, the solid lines and solid points signify resolved events.

events are required to have $\eta_{1,2}^{atl} < 1.6$ and $p_{T_{1,2}}^{atl} > 5$ GeV. The Monte Carlo distributions are normalized to the number of events in the data. Both the data and the Monte Carlo events are likely to have higher values of Y_{cut} for events with $\eta_3^{atl} < -1$. For the data at high η_3^{atl} , the mean value of Y_{cut} is 0.028. For the low η_3^{atl} data, the mean value of Y_{cut} is 0.063. This result suggests that the high η_3^{atl} events contain a significant number of direct, two-jet events, for which the clustering procedure has been prematurely stopped. For the sample of events with $\eta_3^{atl} < -1$, however, the separation between the three clusters is quite distinct. The average value of Y_{cut} for the data with $\eta_3^{atl} < -1$ is lower than the Monte Carlo expectation. This may be due to the fact that the Monte Carlo simulation does not properly describe the E_T^{atl} distribution of the data (Y is inversely proportional to E_T^{atl}). The separation between direct and resolved events can also be based on x_3^{conr} . Figure 6.11c shows the value of Y_{cut} for the data with $x_3^{conr} < 0.75$ (full circles) and $x_3^{conr} > 0.75$ (open circles). Again, both the data and the Monte Carlo simulation have higher average values of Y_{cut} for resolved (defined as $x_3^{conr} < 0.75$) events.

Since the value of Y_{cut} is chosen on an event-by-event basis, it is interesting to determine if a fixed value of Y_{cut} for all events would change the results. Figure 6.15a shows the number of events (out of 1370) which contain three clusters with $\eta_{1,2}^{atl} < 1.6$, $p_{T_{1,2}}^{atl} > 5$ GeV, $\eta_3^{atl} < -1$ and $E_3^{atl} > 2$ GeV, when the value of Y_{cut} is fixed for all events. The value of Y_{cut} is fixed at 0.01, 0.03, 0.05, 0.07, 0.09, 0.11, 0.13 and 0.15, as indicated by the black circles. Since a range of Y values, in any given event, can result in three clusters being found (for example, for some events fixing Y_{cut} at 0.03 and 0.05 might both result in three clusters being found), the integrated number of events in Fig. 6.15a can

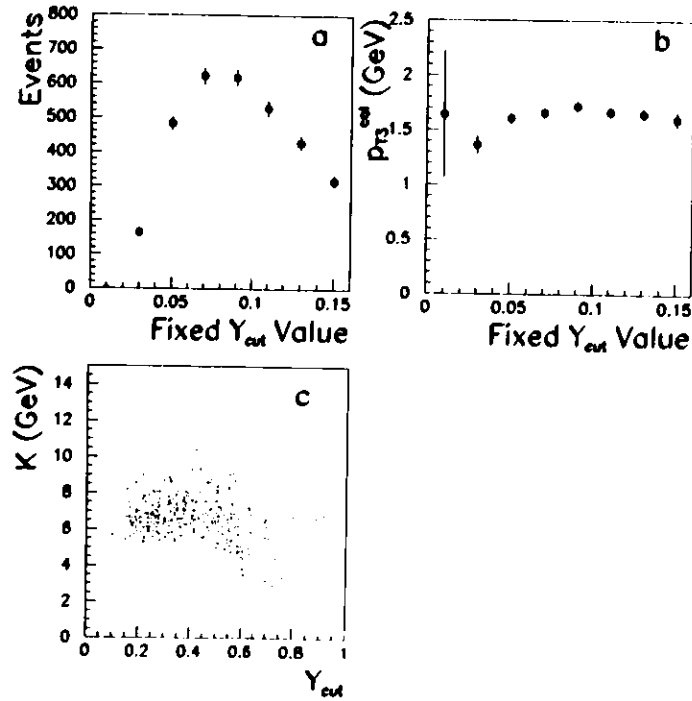


Figure 6.15: (a) Number of events which contain three clusters which satisfy: $p_{T1,2}^{cut} > 5$ GeV, $\eta_{1,2}^{cut} < 1.6$, $\eta_3^{cut} < -1$, and $E_3^{cut} > 2$ GeV for Y_{cut} fixed at 0.01, 0.03, 0.05, 0.07, 0.09, 0.11, 0.13 and 0.15. (b) Mean value of p_{T3}^{cut} at fixed values of Y_{cut} for the events shown in (a). (c) Correlation between $K = \sqrt{k_{\perp}}$ and Y_{cut} when three clusters are found in each event.

be greater than 1370. From Fig. 6.15a it is apparent that about half of the events in the final sample are also selected if Y_{cut} is fixed between 0.06 and 0.1. Therefore, one significant effect of choosing the value of Y_{cut} on an event-by-event basis is that the number of events in the final sample is approximately doubled.

Figure 6.15b, shows the mean value of p_{T3}^{cut} for the events in the fixed Y_{cut} bins of Fig. 6.15a. One might expect p_{T3}^{cut} to depend on Y_{cut} , since clusters with large p_{T3}^{cut} , in the rear direction, tend to have larger angles with respect to the beam axis, and therefore, smaller values of k_{\perp} with respect to clusters one and two (which are usually in the forward direction). In fact, p_{T3}^{cut} is independent of the value of Y_{cut} . The reason p_{T3}^{cut} is independent of the value of Y_{cut} is that if the clustering procedure were continued, and two of the three (plus one for the proton remnant) clusters were merged so that only two clusters remained, the third cluster would generally not be involved in the merger. Instead of the third cluster being combined with one of the two high p_T clusters, as one would expect for direct events, it is more likely that one of the two high p_T clusters would be combined with the proton remnant. For example, Fig. 6.15c shows the relationship between $K = \sqrt{k_{\perp}}$ (measured in GeV) and x_3^{cut} . The value of K tends to be smaller in high- x_3^{cut} events, whereas, in most cases K is larger than 5 GeV in low- x_3^{cut} events. The lower bound at about 5 GeV on low x_3^{cut} events comes from the selection criterion $p_{T1,2}^{cut} > 5$, since k_{\perp} is (in the small angle approximation) equal to the transverse momentum of the lower energy cluster with respect to the higher energy cluster. In this case, the higher energy cluster is the pseudo-particle in the proton direction, and $K \approx p_T^{cut}$. For these low x_3^{cut} events there is a clear

3 cluster structure.

Chapter 7

Photon Remnant Properties

In section 4.4 it was shown that the photon remnant can be isolated as a third, low- p_T cluster found by the k_{\perp} algorithm in the region $\eta_3^{cal} < -1$. In this chapter the physical properties of the photon remnant, corrected to the hadron level, are studied.

7.1 External Attributes

The external attributes of the photon remnant are the measurable quantities which are independent of its internal structure. The pseudorapidity distribution is one example. Since the pseudorapidity of a cluster only depends on the location of the cluster axis, and not, for example, on the number of particles in the cluster, two clusters can have very different internal structures and still have the same pseudorapidities. Likewise, two clusters can have the same energy or transverse momentum and still be very different objects. Therefore, the external attributes of the photon remnant are useful in studying how the photon remnant behaves as an object irrespective of its internal structure.

7.1.1 Comparison with PYTHIA

Figure 7.1, shows the pseudorapidity (η_3), transverse momentum (p_{T3}) and energy (E_3) distributions of the photon remnant, corrected back to the hadron level. To show the effect of the requirement that η_3 be less than -1 , the full η_3 distribution is shown. Photon remnant events are, by definition, those events with $\eta_3 < -1$. In the energy and transverse momentum distributions, η_3 is required to be less than -1 . Figure 7.1a shows the η_3 distribution. The inner solid error bars are the statistical errors. The thin outer error bars are the statistical and systematic errors added in quadrature. The calculation of the error bars was described in the previous chapter. The corrected data and the PYTHIA Monte Carlo events (solid histogram) disagree in the negative η_3 region, as previously observed in the uncorrected η_3^{cl} distribution (Fig. 4.1d). The peak in the data is located at higher values of η_3 than it is in the PYTHIA Monte Carlo prediction. A similar effect occurs in the transverse momentum distribution (Fig. 7.1b). Here also, the data show a higher average value than the Monte Carlo. The mean value of the photon remnant p_T at the hadron level is measured to be $\langle p_{T3} \rangle = 2.1 \pm 0.2$ GeV, whereas the Monte Carlo expectation is $\langle p_{T3} \rangle = 1.44 \pm 0.02$ GeV. In the energy distribution, however, (Fig. 7.1c), the Monte Carlo expectation agrees with the data, except in the lowest energy bin.

The most likely explanation of the lower average values of p_{T3} and η_3 in the Monte Carlo simulation is that the Monte Carlo simulation does not include the anomalous process, as discussed in section 1.2. The correction factors applied to the uncorrected data in the p_{T3} , η_3 and E_3 distributions tend

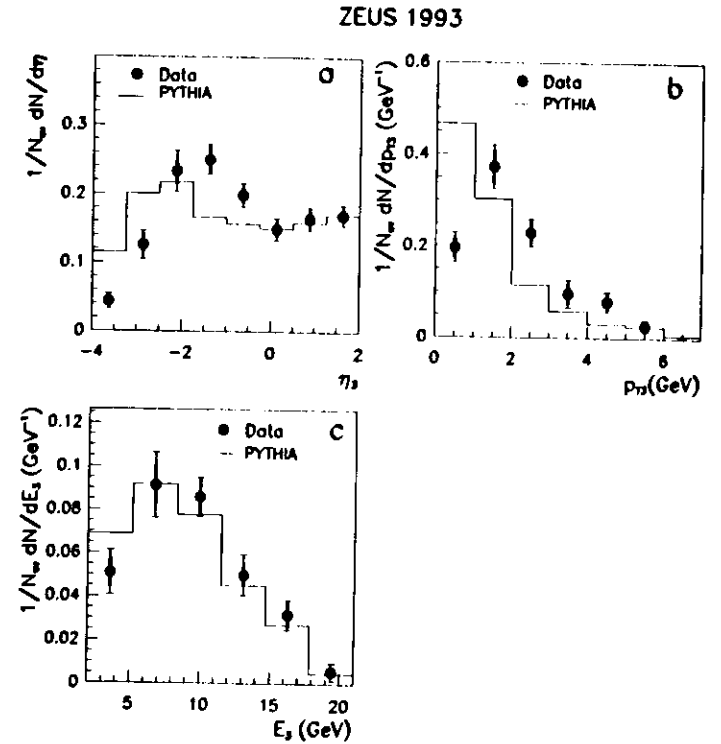


Figure 7.1: (a) Pseudorapidity (η_3) distribution of the photon remnant corrected back to the hadron level. (b) Corrected transverse momentum (p_{T3}) distribution. (c) Corrected energy (E_3) distribution. In (b) and (c) $\eta_3 < -1$ is required. The solid histograms are the hadron level distributions given by PYTHIA with default parameters (including $k_0 = 0.11$ GeV in equation 7.2). The inner solid error bars are the statistical errors. The thin outer error bars are the statistical and systematic errors added in quadrature.

to be small (typically around 1.2) and are approximately constant. Therefore, the disagreement is not created by correcting the data to the hadron level. Although it is conceivable that an incorrect Monte Carlo description of the detector could result in this type of an effect, this explanation has been demonstrated to be incompatible with the data (see section 6.6).

7.1.2 Comparison with High- k_t PYTHIA

Motivated by the poor description of the data by the conventional Monte Carlo simulation, the data are also compared with Monte Carlo events generated with a harder intrinsic transverse momentum (k_t) spectrum for the partons in the photon. The new parameterization which we call PYTHIA High k_t A,

$$dN/dk_t^2 \propto 1/(k_t^2 + k_0^2), \quad (7.1)$$

was suggested by Drees³⁴ to partially account for the anomalous contribution as discussed in section 1.2. This distribution is shown as the dashed line in Fig. 7.2. The parameterization used in the analysis discussed in the previous section is:

$$dN/dk_t^2 \propto e^{-k_t^2/k_0^2}, \quad (7.2)$$

with $k_0 = 0.41$ GeV, (shown as the solid line in Fig. 7.2). The parameter k_0 for the PYTHIA high- k_t A parameterization is determined by minimizing the χ^2 between the Monte Carlo hadron level and the corrected data p_{T3} distributions. The best fit occurs when $k_0 = 0.66 \pm 0.22$ GeV. This corresponds to an average value of k_t of about 1.7 GeV, as compared to 0.4 GeV for PYTHIA with the default parameters (the values of k_0 used cannot be compared directly because they are not the same quantity in the different parameterizations).

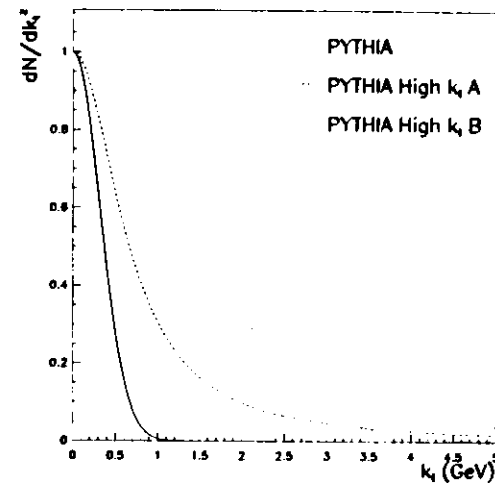


Figure 7.2: *Intrinsic transverse momentum parameterizations for the conventional PYTHIA (solid line), PYTHIA High k_t A, (dashed line), and PYTHIA High k_t B (dotted line).*

The PYTHIA High k_t A results are shown as the dotted histograms in Fig. 7.3. The Monte Carlo description of the data is considerably improved for the η_3 and p_{T3} distributions, while the E_3 distribution is essentially unchanged. Equally good agreement between the data and the Monte Carlo simulation has been achieved by using the default k_t parameterization of equation 7.2, with k_0 raised from $k_0 = 0.41$ GeV to $k_0 = 1.90 \pm 0.21$ GeV. We call this parameterization PYTHIA High k_t B. It is shown as the dashed line in Fig. 7.3. This PYTHIA High k_t B distribution is also shown in Fig. 7.2. The (uncorrected) η_{12}^{a1} and p_{T12}^{ca1} distributions for the two high p_T clusters (Fig. 7.1) are also

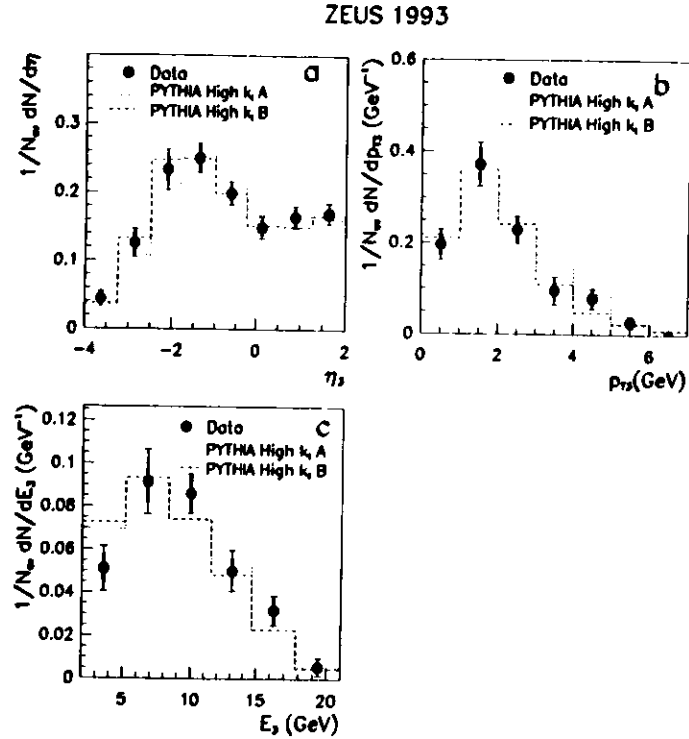


Figure 7.3: Comparison between the data and two different High k_t Monte Carlo parameterizations. The dotted line, "PYTHIA High k_t A" corresponds to equation 7.1 with $k_0 = 0.66$ GeV. The dashed line, "PYTHIA High k_t B" corresponds to the default k_t parameterization (equation 7.2) with $k_0 = 1.90$ GeV. Figure (a) shows the η_3 distribution. Figure (b) shows the p_{T3} distribution, and figure (c) shows the E_3 distribution. In (b) and (c) $\eta_3 < -1$ is required.

essentially unchanged.

The fact that the Monte Carlo simulation can be easily brought into agreement with the data, by increasing the average k_t , is encouraging. Although the average value of k_t needs to be increased substantially in order to bring the Monte Carlo simulation into agreement with the data, this is not surprising. Since the anomalous contribution is perturbative, it necessarily has significant ($O(1$ GeV)) p_T . Perhaps the inclusion of the anomalous contribution, which inspired the use of the High k_t Monte Carlo simulation, will bring the Monte Carlo simulation into good agreement with the data. Future studies with Monte Carlo simulations which include the anomalous contribution are necessary to demonstrate that it is, in fact, sufficient to describe the data.

7.2 Internal Attributes

The internal attributes of the photon remnant are measured with respect to the cluster axis. Although two energy clusters can have very different internal structures and still have the same energy, the internal structure of a cluster may not be totally independent of its energy. Jets of particles, for example, tend to fragment into more particles as the jet energy increases. However, the average transverse energy of each of those particles with respect to the jet axis tends to be on the order of a few hundred MeV, and tends to rise slowly with jet energy. Behavior of this type is a distinctive signature of particle jets. One interesting question is whether or not the photon remnant also exhibits this type of behavior. Because of the possible energy dependence, all of the figures in this section are plotted either as a function of energy, or in a limited energy

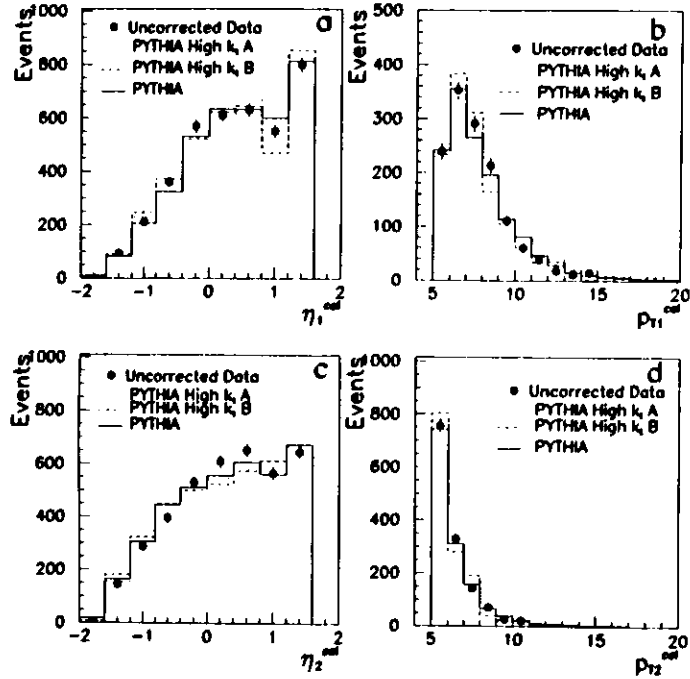


Figure 7.4: Effect of the High k_i reweighting on the two high- p_T jets. (a) Pseudorapidity distributions for the highest p_T^{cal} jet for the uncorrected data and for the standard PYTHIA, PYTHIA High k_i A, and PYTHIA High k_i B Monte Carlo simulations. (b) Transverse momentum distributions for the highest p_T^{cal} jet. (c) Pseudorapidity distributions for the second highest p_T^{cal} jet. (d) Transverse momentum distributions for the second highest p_T^{cal} jet.

range.

7.2.1 Structure of High- p_T Jets

The internal attributes of the two high- p_T jets are shown in Fig. 7.5. Figure 7.5a shows the mean value of the average energy transverse to the cluster axis per particle, $\langle E_T^i \rangle$, as a function of the jet energy (the data from the two high- p_T jets are combined in this figure). The mean value of $\langle E_T^i \rangle$ starts near 250 MeV, and slowly increases with the jet energy, while the total energy increases from 6 to 24 GeV. This is the type of behavior one expects to see for particle jets. The hadron level Monte Carlo simulation is in good agreement with the data. Figure 7.5b shows the corrected mean values of the total transverse ($\Sigma_i E_T^i$) and total longitudinal ($\Sigma_i E_L^i$) energy of the two high- p_T jets, with respect to the jet axis. The quantities $\Sigma_i E_T^i$ and $\Sigma_i E_L^i$ are plotted as a function of the jet energy. The longitudinal component increases rapidly, while the transverse component increases only slowly, demonstrating that the jet energy is primarily along the jet axis. The Monte Carlo simulation is in excellent agreement with the data.

Figure 7.5c shows the corrected energy flow of jets 1 and 2 as a function of $1 - \cos\Theta$. Here, Θ is the angle of the jet particle with respect to the jet axis. This figure is effectively a plot of the energy deposited in rings of fixed area centered on the jet axis. Because a simple correspondence between particles and calorimeter cells does not exist, it is difficult to construct a correlation matrix between the generated (hadron energy) and experimental (calorimeter cell energy) quantities. Therefore, these distributions are corrected back to the hadron level bin-by-bin, as described in section 5.4.1. The statistical errors are

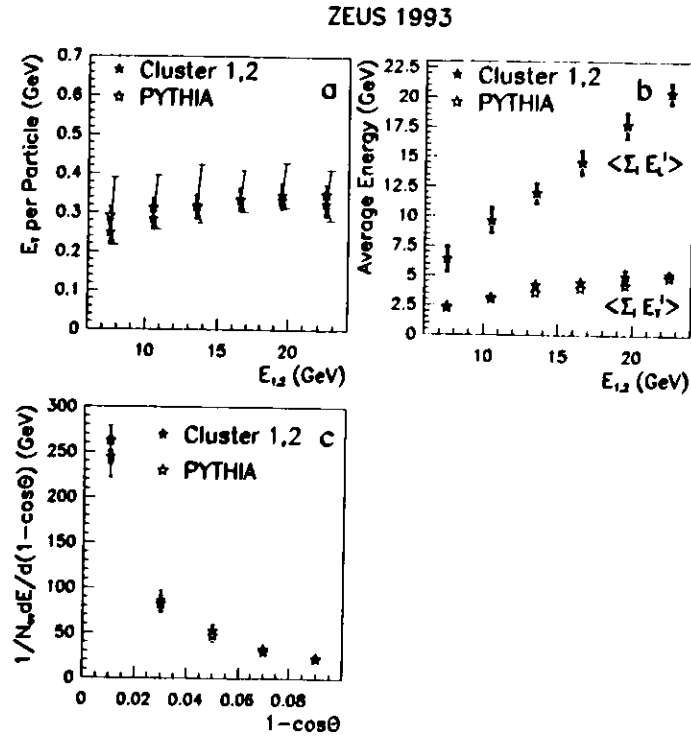


Figure 7.5: Internal attributes of high- p_T jets. The corrected data are compared with the hadron level Monte Carlo expectations. (a) The mean value of $\langle E_T^i \rangle$, the average energy transverse to the cluster axis per particle, as a function of the cluster energy. (b) The average values of the total transverse ($\langle \sum_i E_T^i \rangle$) and total longitudinal ($\langle \sum_i E_L^i \rangle$) energy. (c) The flow of energy around the cluster axis.

the error on the mean in each bin. In Fig. 7.5c, the detector level jet energies are required to be between 8 and 14 GeV and the hadron level jet energies are required to be between 8 and 15 GeV. The energy distribution for the data is quite collimated. The Monte Carlo simulation models this distribution very well.

7.2.2 Comparison with High- p_T Jets

The photon remnant is now compared with the two high p_T jets originating from parton hard scattering. The comparison of these two types of jets is of interest because one is the debris of the photon and is a low- p_T jet, with p_T typically well below 6 GeV, while the other two jets come from the hard scattering of the partons in the photon and proton and are high- p_T jets, with a minimum p_T of 6 GeV. Therefore, it is not obvious that these objects should have the same internal structure. In fact, the photon remnant may originally have been made up of many partons, whereas high p_T jets most likely originate from a single parton.

In Fig. 7.6a the results of this comparison are shown for the mean value of $\langle E_T^i \rangle$, the average transverse energy with respect to the cluster axis per particle, as a function of the cluster energy. In the region where the remnant and high- p_T jet energies overlap, the photon remnant data are very similar to the data from the two high- p_T jets. Figure 7.6b shows the total transverse ($\langle \sum_i E_T^i \rangle$) and total longitudinal ($\langle \sum_i E_L^i \rangle$) energy with respect to the cluster axis as a function of the cluster energy, and Fig. 7.6c shows the cluster energy deposited as a function of $1 - \cos\theta$. In Fig. 7.6c, the reconstructed (uncorrected) jet energies are again required to be between 8 and 11 GeV, and the

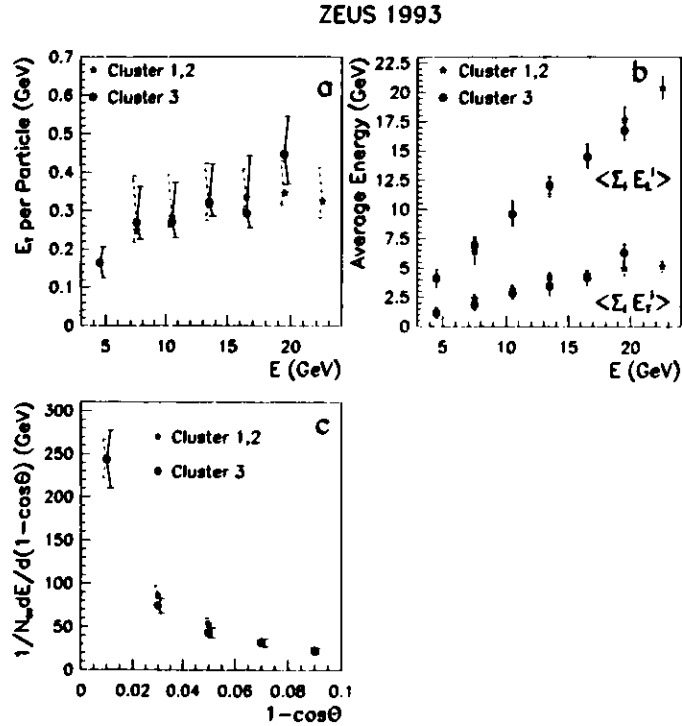


Figure 7.6: Comparison between the photon remnant (cluster 3) and the two high- p_T jets (cluster 1,2). (a) The mean value of $\langle E_T^i \rangle$ as a function of the cluster energy. (b) The average values of $\langle \Sigma_i E_T^i \rangle$ and $\langle \Sigma_i E_L^i \rangle$ as a function of the cluster energy. (c) The flow of energy around the cluster axis. The error bars show the systematic and statistical errors added in quadrature.

hadron level jet energies are required to be between 8 and 15 GeV. These requirements are especially important for this figure so that jets of approximately equal energies can be compared. In all figures, good agreement between the photon remnant and the two high- p_T jets is observed. Therefore, in the kinematic region and for the variables studied, the low- p_T photon remnant exhibits the same hadronization characteristics as the high- p_T jets originating from the hard scattering process.

7.2.3 Comparison with PYTHIA

Finally, it is interesting to compare the data with the conventional Monte Carlo simulation. Figure 7.7a shows the mean value of the average energy transverse to the cluster axis per particle, $\langle E_T^i \rangle$, versus the photon remnant energy, both for the data after correction and for the hadron level Monte Carlo simulation. The Monte Carlo simulation is in good agreement with the data. The Monte Carlo simulation is also in good agreement with the data in Fig. 7.7b, which shows the mean values of the corrected total transverse ($\langle \Sigma_i E_T^i \rangle$) and total longitudinal ($\langle \Sigma_i E_L^i \rangle$) energy of the photon remnant, with respect to the cluster axis, as a function of the energy of the cluster. Figure 7.7c shows the corrected energy flow of the photon remnant as a function of $1 - \cos\theta$ for both the data and the Monte Carlo simulation. As was previously the case, the uncorrected jet energies are required to be between 8 and 14 GeV and the hadron level jet energies are required to be between 8 and 15 GeV. The Monte Carlo simulation agrees very well with the data in all figures. This indicates that the fragmentation of the photon remnant is understood. Since the fragmentation of the photon remnant should not depend on the intrinsic

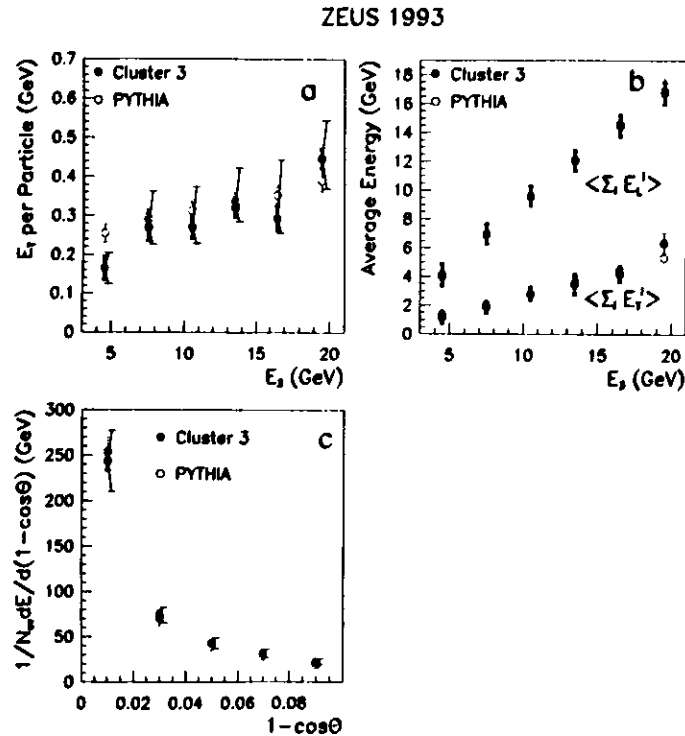


Figure 7.7: Internal attributes of the photon remnant. The corrected data are compared with the hadron level Monte Carlo expectations. (a) The mean value of $\langle E_T \rangle$, the average energy transverse to the cluster axis per particle, as a function of the cluster energy. (b) The average values of the total transverse ($\langle \Sigma_i E_{T_i} \rangle$) and total longitudinal ($\langle \Sigma_i E_{L_i} \rangle$) energy. (c) The flow of energy around the cluster axis.

transverse momentum of the partons in the photon, it is not surprising that the data and the conventional Monte Carlo simulation agree.

7.3 Independent Confirmation

As described in section 6.2, the results of this analysis ("Analysis A") were confirmed independently by another analysis ("Analysis B"). Figures 7.8-7.11 compare the results of the two analyses for the figures previously shown in this Chapter. Figure 7.8 shows the results of the two analyses for the η_s , p_{T3} , and E_s distributions. Both the corrected data and the conventional PYTHIA hadron level Monte Carlo simulation are shown. The agreement is good in all quantities. Figure 7.9 compares the results of the two analyses for the $\langle E_T^2 \rangle$, $\Sigma_i E_{L_i}^2$ and $\Sigma_i E_{T_i}^2$ and energy flow figures. Both the data and the hadron level Monte Carlo simulation are in good agreement between the two analyses.

In Figs. 7.10 the comparison between the two high p_T jets and the photon remnant is shown for the two analyses. The two analyses are in good agreement. Last, Fig. 7.11 compares the results of the two analyses for the energy flow figures. The comparison between the two high p_T jets and the photon remnant are in good agreement. From these figures it is clear that both analyses report very similar results.

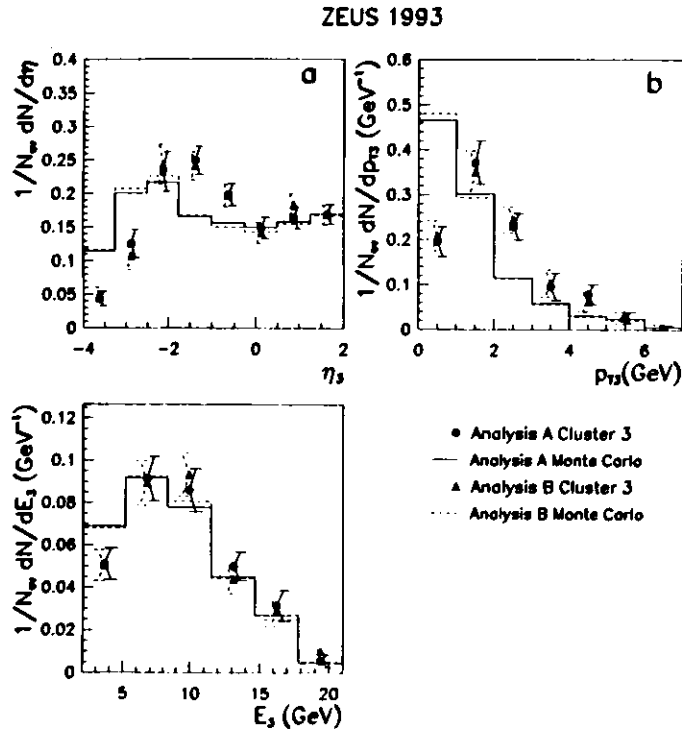


Figure 7.8: Comparison of the results of Analysis A and Analysis B for the corrected data and for the hadron level Monte Carlo simulation. (a) Pseudorapidity (η_s) distribution of the photon remnant corrected back to the hadron level. (b) Corrected transverse momentum (p_{T3}) distribution. (c) Corrected energy (E_s) distribution. In (b) and (c) $\eta_s < -1$ is required. The solid histograms are the hadron level distributions given by PYTHIA with default parameters (including $k_0 = 0.41$ GeV in equation 7.2).

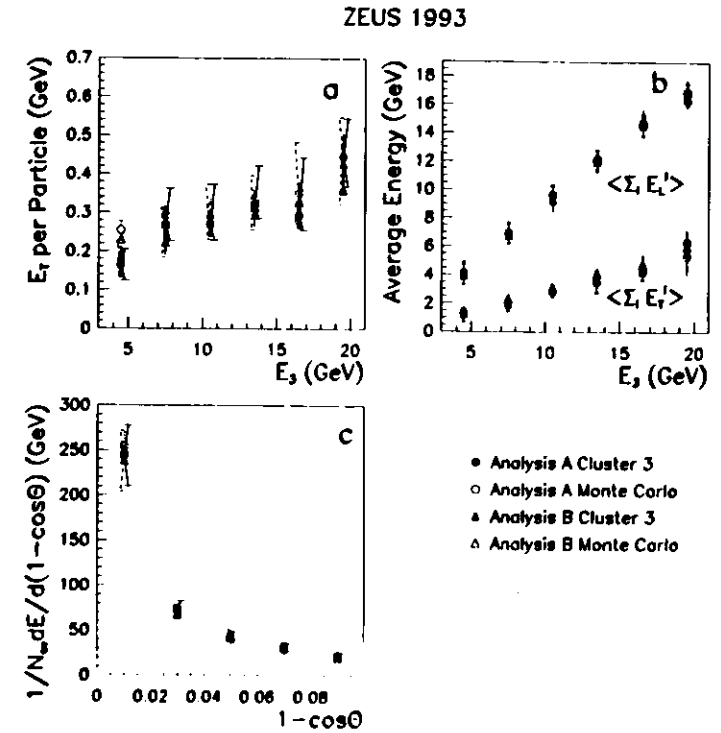


Figure 7.9: Comparison between the (corrected) internal attributes of the photon remnant for Analysis A (solid circles) and Analysis B (solid triangles). The hadron level Monte Carlo expectations are also shown for Analysis A (open circles) and Analysis B (open triangles). (a) The mean value of $\langle E_T^2 \rangle$ as a function of the cluster energy. (b) The average values of $\Sigma_i E_{T_i}^2$ and $\Sigma_i E_{T_i}'$ as a function of the cluster energy. (c) The flow of energy around the cluster axis. The error bars show the systematic and statistical errors added in quadrature.

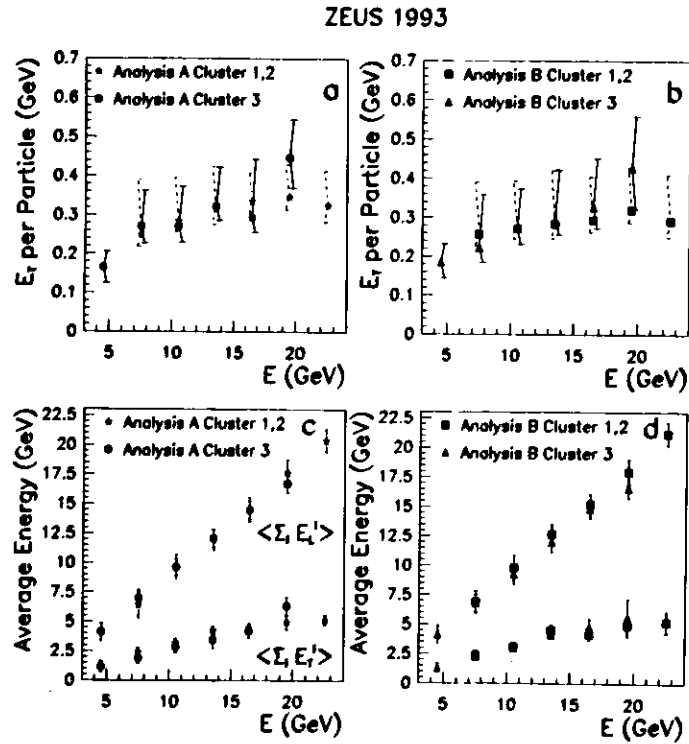


Figure 7.10: Comparison between Analysis A ((a) and (c)) and Analysis B ((b) and (d)). The corrected mean value of $\langle E_T^1 \rangle$ as a function of the cluster energy for the photon remnant and for the two high- p_T jets as determined by Analysis A (a) and Analysis B (b). The corrected mean value of $\Sigma_i E_i^1$ and $\Sigma_i E_i^2$ as a function of the cluster energy for the photon remnant and for the two high- p_T jets as determined by Analysis A (c) and Analysis B (d).

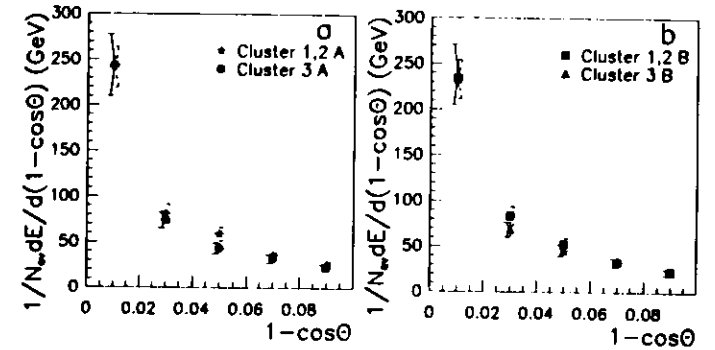


Figure 7.11: Comparison between the corrected energy flow around the cluster axis of the photon remnant and the two high p_T jets as measured by (a) Analysis A and (b) Analysis B.

Chapter 8

Conclusions

For the first time, in a sample of quasi-real photon-proton collisions, the photon remnant produced in resolved photon interactions has been isolated. The selected events contain two high- p_T jets with $p_T > 6$ GeV and $\eta < 1.6$. The photon-proton center of mass energy, $W_{\gamma,p}$, for these events ranges from 130 to 270 GeV. The properties of the photon remnant, as defined by a cluster with $\eta_3 < -1$ and $E_3 > 2$ GeV, are studied. The photon remnant exhibits collimated energy flow with limited transverse energy with respect to the cluster axis, features characteristic of particle jet structure.

The leading order QCD Monte Carlo simulation, with default parameters, does not reproduce the pseudorapidity distribution or the transverse momentum distribution (with respect to the incident photon) of the photon remnant. The mean value of p_T for the photon remnant, 2.1 ± 0.2 GeV, is substantially larger than the Monte Carlo expectation of 1.44 ± 0.02 GeV. Better agreement with the data can be obtained by increasing the average intrinsic transverse momenta (k_t) of the partons in the photon in the Monte Carlo simulation. The best agreement with the data occurs when the mean value of k_t is increased from 0.4 GeV to about 1.7 GeV. These results are in qualitative agreement with theoretical expectations which predict substantial mean transverse momenta

for the photon remnant, arising, in part, from the anomalous contribution.

The photon remnant has also been compared, in the laboratory frame, with the two high- p_T jets originating from the parton hard scattering. Although the origins of these two types of jets may be quite different, within the present statistics and in the kinematic range studied, they exhibit similar properties. The photon remnant mean transverse energy per particle with respect to the jet axis, the total transverse and total longitudinal energy with respect to the jet axis, and the energy flow around the jet axis are all quite similar to those of the high- p_T jets.

Appendix A

Variable Resolutions

In this appendix, the detector level resolution with respect to the hadron level is shown for all variables used in this study. The figures shown here have been used to determine the numbers quoted in table 5.1. This appendix is broken into two sections. The first section shows figures produced using the PYTHIA Monte Carlo simulation. The second section shows figures produced using the HERWIG Monte Carlo simulation.

In all figures, the events are required to pass the cuts at both the detector level (as described in section 4.4) and at the hadron level (as described in section 5.1). Matching between the hadron and detector level clusters (as described in section 5.2) is also required. All figures in this appendix follow the format of Fig. 5.2.

A.1 PYTHIA

Figures A.1–A.3 show the resolution of the pseudorapidity measurement for all three clusters obtained with the k_{\perp} algorithm, as determined using the

PYTHIA Monte Carlo simulation. In each of the figures, (a) shows the correlation (smearing matrix) between the detector level and hadron level pseudorapidity distributions; (b) shows the resolution in percent ($\frac{\eta_n - \eta_n^{had}}{\eta_n} \times 100$ where $n = 1, 2$ or 3) and (c) shows the absolute resolution ($\eta_n - \eta_n^{had}$). The pseudorapidity resolution is excellent for the two high- p_T clusters. For the photon remnant, the pseudorapidity resolution is best near $\eta_3 = -1$, and becomes worse as the jet axis of the photon remnant gets closer and closer to the RCAL beam pipe. This effect is probably caused by particles lost in the beam pipe.

Figures A.4–A.6 show the resolution of the transverse momentum measurement for all three clusters. The correlation between the detector level and hadron level transverse momentum is good, although not as good as for the pseudorapidity. Figure A.6 is interesting because the mean photon remnant transverse momenta is measured to be significantly higher than predicted by the PYTHIA Monte Carlo simulation. In Fig. A.6b, the percent transverse momentum resolution of the photon remnant, a long tail toward negative values can be seen. Although, on average, the photon remnant transverse momentum measured at the detector level tends to be smaller than it is at the hadron level, in some cases the photon remnant transverse momentum can be significantly overestimated. This effect is included in the correction procedure.

The energy resolutions for clusters 1 and 2 are shown in Figs. A.7 and A.8 respectively. The energy resolution is quite good, and is consistent between the two objects.

The resolution in $y_{J,B}$ is given in Fig. A.9. The resolution and systematic shift seen here is in agreement with the results from other analysis.¹⁷

Figures A.10, A.11 and A.12 show the correlation between the transverse energy per island and the transverse energy per particle. For these figures the resolution is rather poor. The systematic shift from the detector to the hadron level, however, is small. For comparison, Figs. A.13, A.14 and A.15 show the correlation between the transverse energy per cell and the transverse energy per particle. Here, again, the resolution is poor. In this case, however, there is a significant systematic shift from the detector to the hadron level, due to the fact that there are, on average, three cells per particle.

Figures A.16, A.17 and A.18 show the measurement resolution of the total transverse energy with respect to the cluster axis, and Figs. A.19, A.20 and A.21 show the measurement resolution of the total longitudinal energy with respect to the cluster axis. In general, the longitudinal component is measured with higher resolution than is the transverse component.

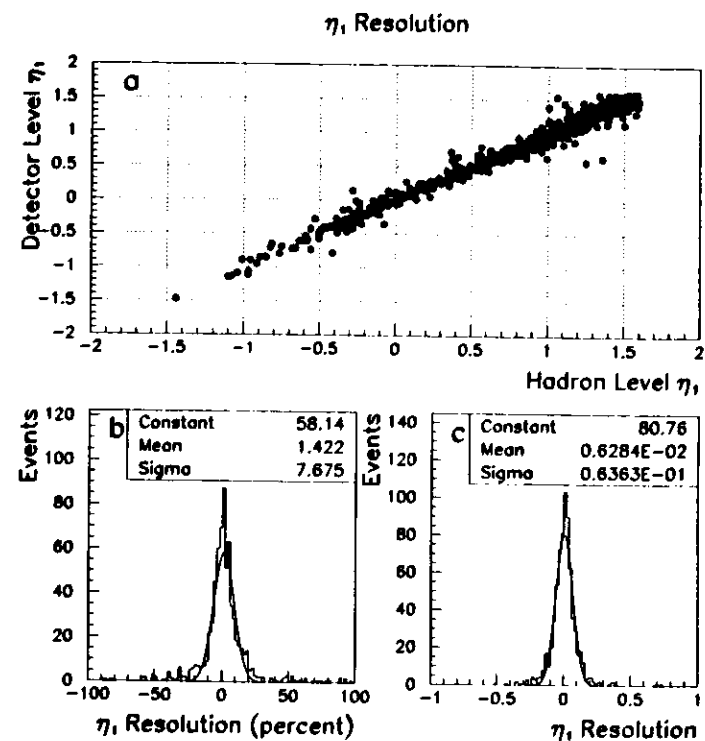


Figure A.1: Pseudorapidity resolution of the highest p_T cluster as determined using the PYTHIA Monte Carlo simulation. (a) Correlation between the detector and hadron level pseudorapidity. (b) Pseudorapidity resolution in percent. (c) Absolute pseudorapidity resolution. The constant, mean and sigma in (b) and (c) are determined from the fit.

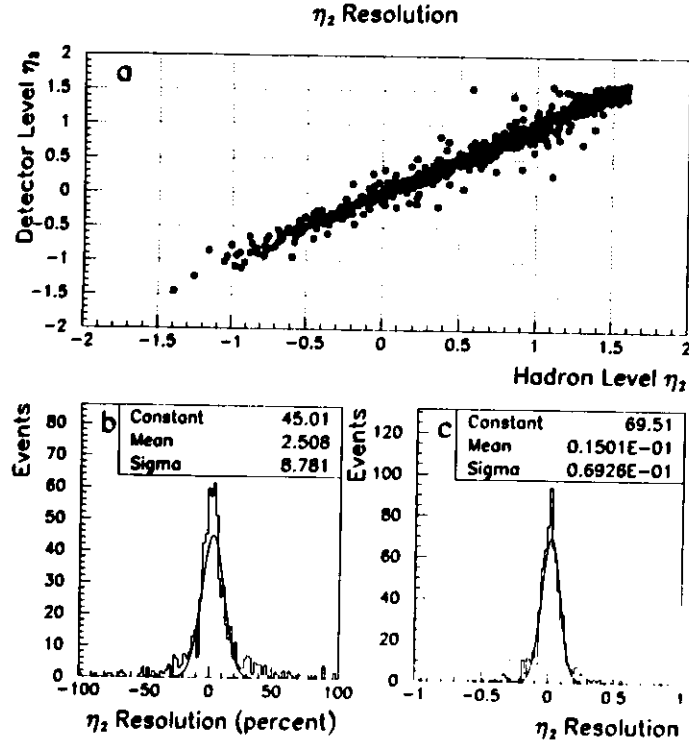


Figure A.2: Pseudorapidity resolution of the second highest p_T cluster as determined using the PYTHIA Monte Carlo simulation. (a) Correlation between the detector and hadron level pseudorapidity. (b) Pseudorapidity resolution in percent. (c) Absolute pseudorapidity resolution. The constant, mean and sigma in (b) and (c) are determined from the fit.

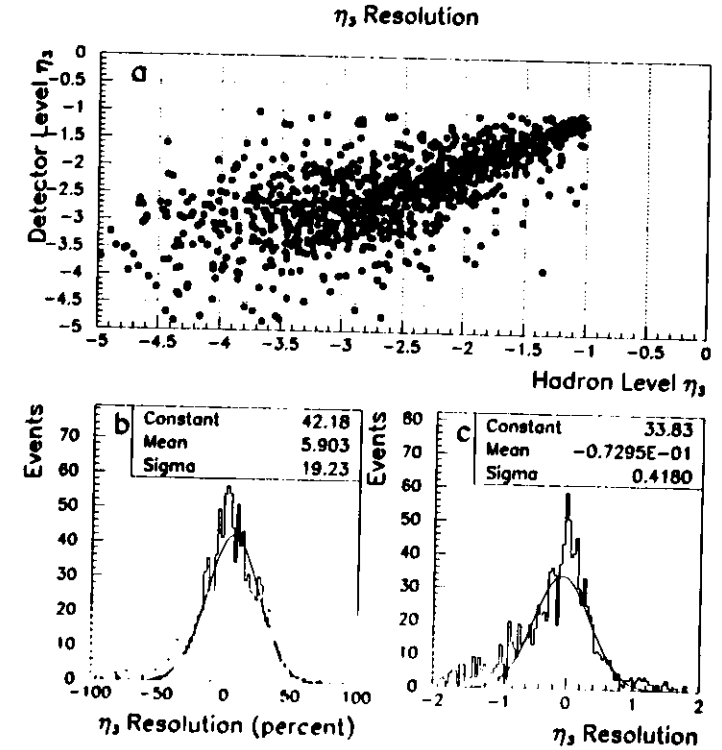


Figure A.3: Pseudorapidity resolution of the photon remnant as determined using the PYTHIA Monte Carlo simulation. (a) Correlation between the detector and hadron level pseudorapidity. (b) Pseudorapidity resolution in percent. (c) Absolute pseudorapidity resolution. The constant, mean and sigma in (b) and (c) are determined from the fit.

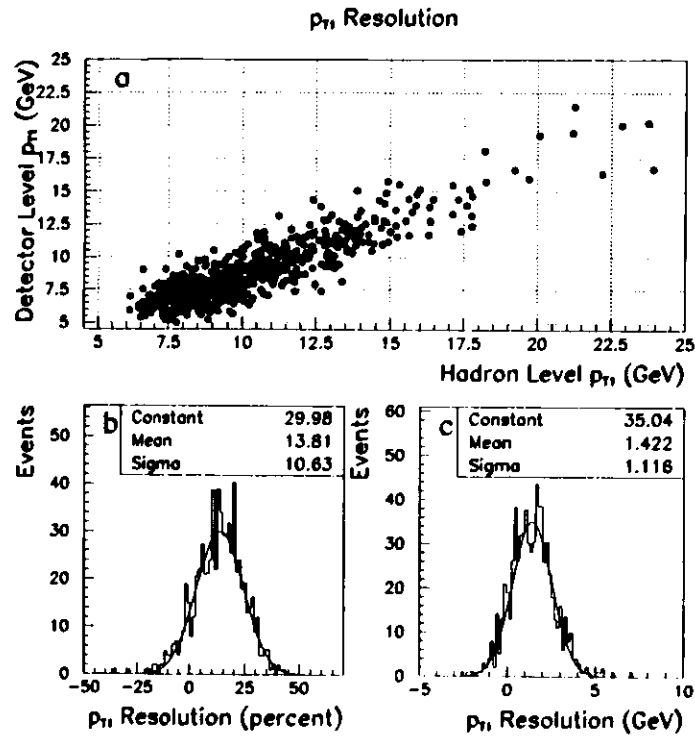


Figure A.4: Transverse momentum resolution of the highest p_T cluster as determined using the PYTHIA Monte Carlo simulation. (a) Correlation between the detector and hadron level transverse momentum. (b) Transverse momentum resolution in percent. (c) Absolute transverse momentum resolution in GeV. The constant, mean and sigma in (b) and (c) are determined from the fit.

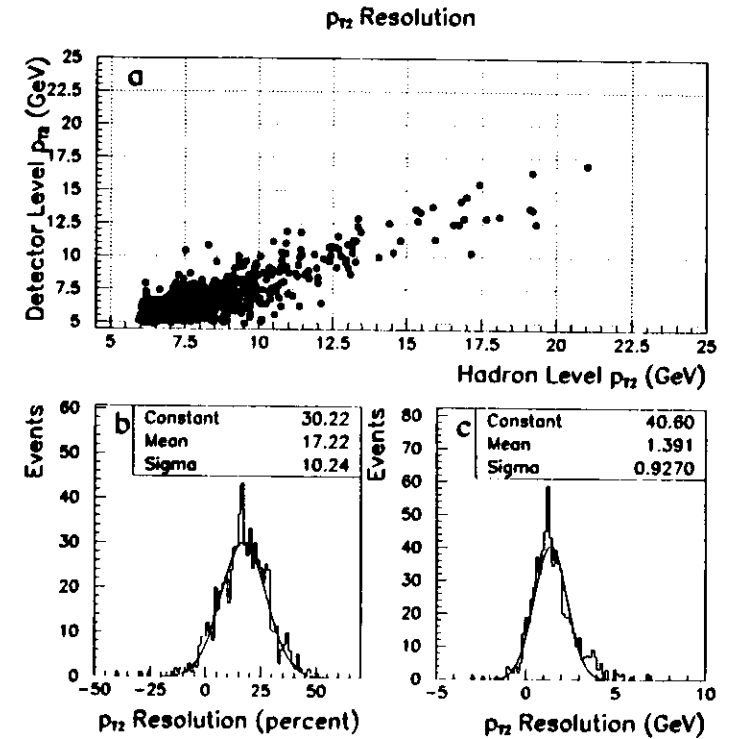


Figure A.5: Transverse momentum resolution of the second highest p_T cluster as determined using the PYTHIA Monte Carlo simulation. (a) Correlation between the detector and hadron level transverse momentum. (b) Transverse momentum resolution in percent. (c) Absolute transverse momentum resolution in GeV. The constant, mean and sigma in (b) and (c) are determined from the fit.

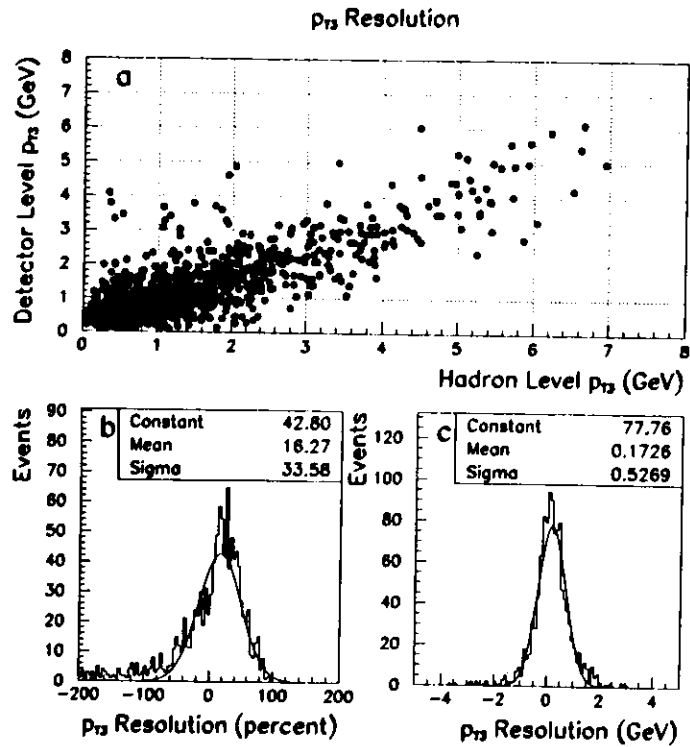


Figure A.6: Transverse momentum resolution of the photon remnant as determined using the PYTHIA Monte Carlo simulation. (a) Correlation between the detector and hadron level transverse momentum. (b) Transverse momentum resolution in percent. (c) Absolute transverse momentum resolution in GeV. The constant, mean and sigma in (b) and (c) are determined from the fit.

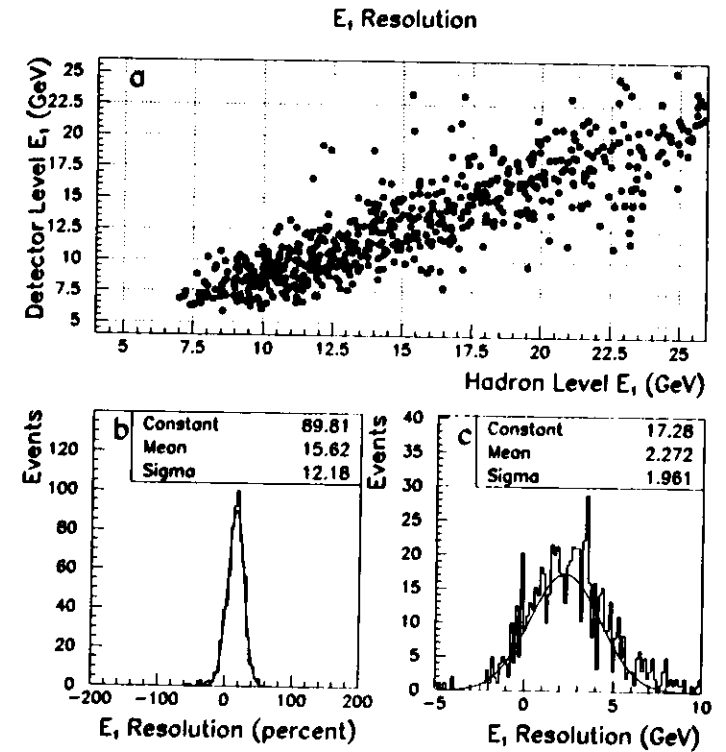


Figure A.7: Energy resolution of the highest p_T cluster as determined using the PYTHIA Monte Carlo simulation. (a) Correlation between the detector and hadron level energy. (b) Energy resolution in percent. (c) Absolute energy resolution in GeV. The constant, mean and sigma in (b) and (c) are determined from the fit.

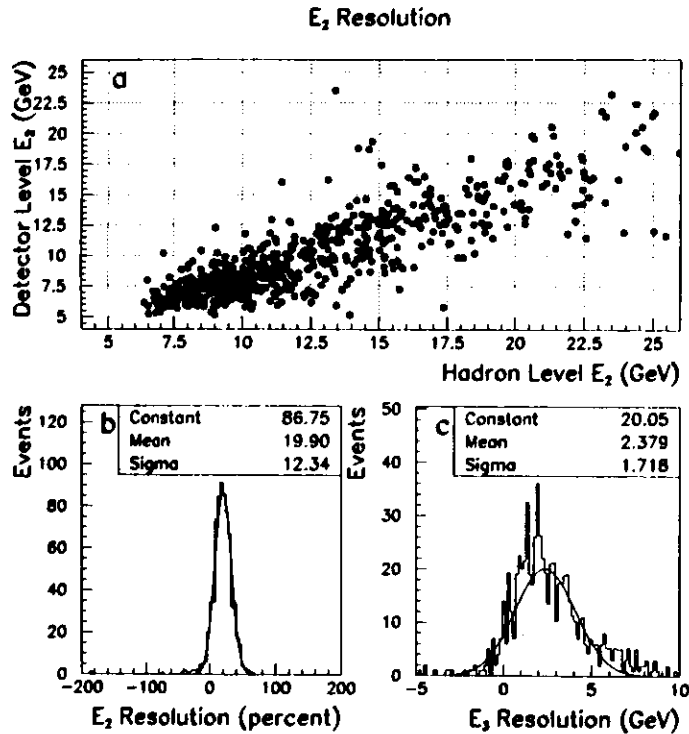


Figure A.8: Energy resolution of the second highest p_T cluster as determined using the PYTHIA Monte Carlo simulation. (a) Correlation between the detector and hadron level energy. (b) Energy resolution in percent. (c) Absolute energy resolution in GeV. The constant, mean and sigma in (b) and (c) are determined from the fit.

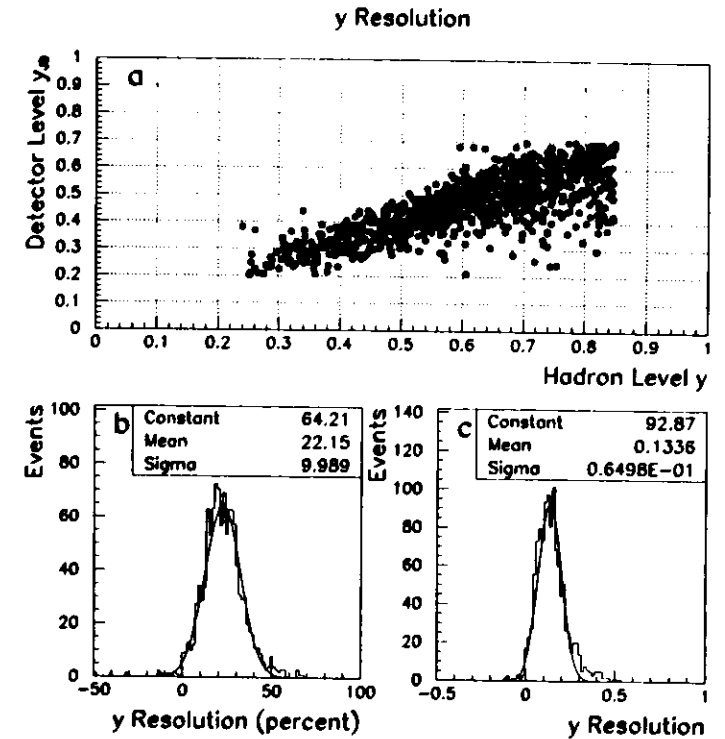


Figure A.9: The y resolution as determined using the PYTHIA Monte Carlo simulation. (a) Correlation between the detector and hadron level y . (b) y resolution in percent. (c) Absolute y resolution. The constant, mean and sigma in (b) and (c) are determined from the fit.

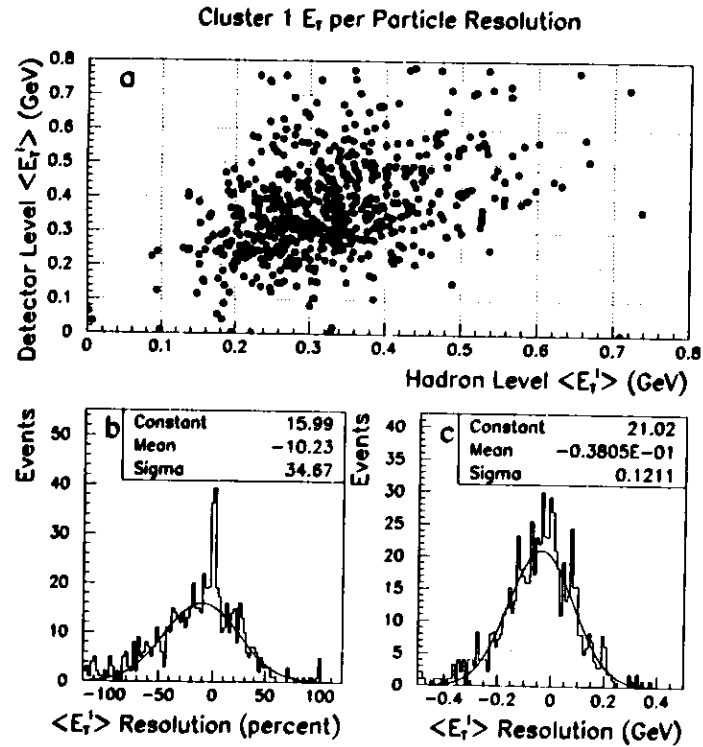


Figure A.10: The $\langle E_T \rangle$ resolution (calculated using calorimeter islands) of the highest p_T cluster determined using the PYTHIA Monte Carlo simulation. (a) Correlation between the detector and hadron level $\langle E_T \rangle$. (b) $\langle E_T \rangle$ resolution in percent. (c) Absolute $\langle E_T \rangle$ resolution in GeV. The constant, mean and sigma in (b) and (c) are determined from the fit.

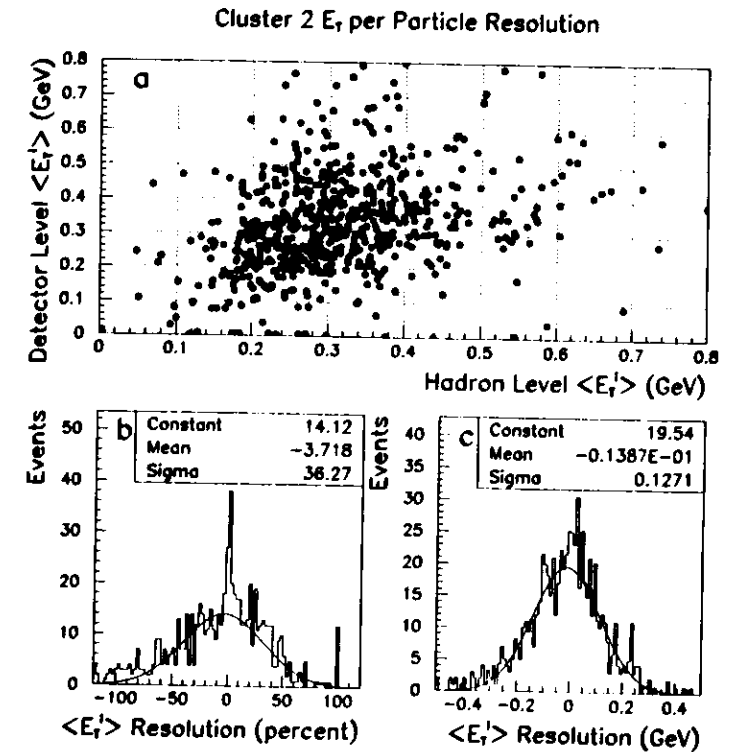


Figure A.11: The $\langle E_T \rangle$ resolution (calculated using calorimeter islands) of the second highest p_T cluster as determined using the PYTHIA Monte Carlo simulation. (a) Correlation between the detector and hadron level $\langle E_T \rangle$. (b) $\langle E_T \rangle$ resolution in percent. (c) Absolute $\langle E_T \rangle$ resolution in GeV. The constant, mean and sigma in (b) and (c) are determined from the fit.

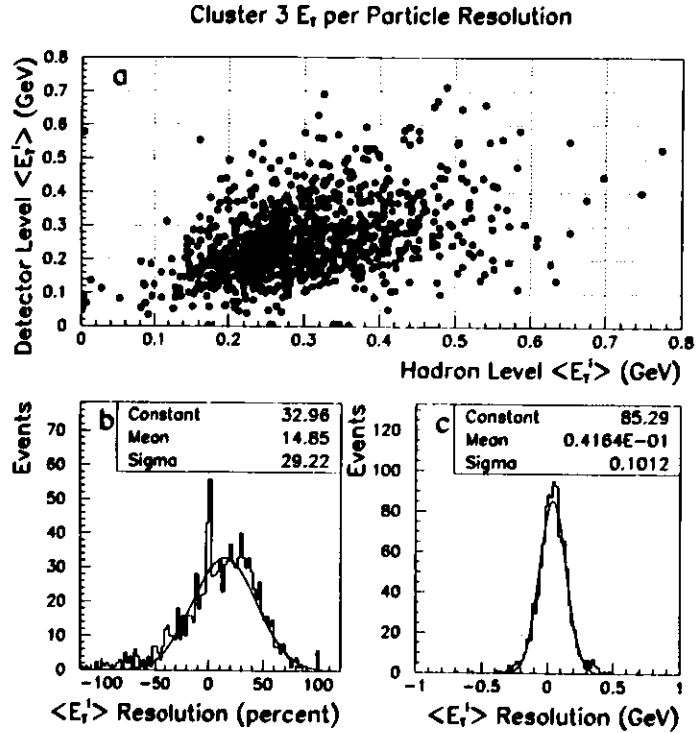


Figure A.12: The $\langle E_T^i \rangle$ resolution (calculated using calorimeter islands) of the photon remnant as determined using the PYTHIA Monte Carlo simulation. (a) Correlation between the detector and hadron level $\langle E_T^i \rangle$. (b) $\langle E_T^i \rangle$ resolution in percent. (c) Absolute $\langle E_T^i \rangle$ resolution in GeV. The constant, mean and sigma in (b) and (c) are determined from the fit.

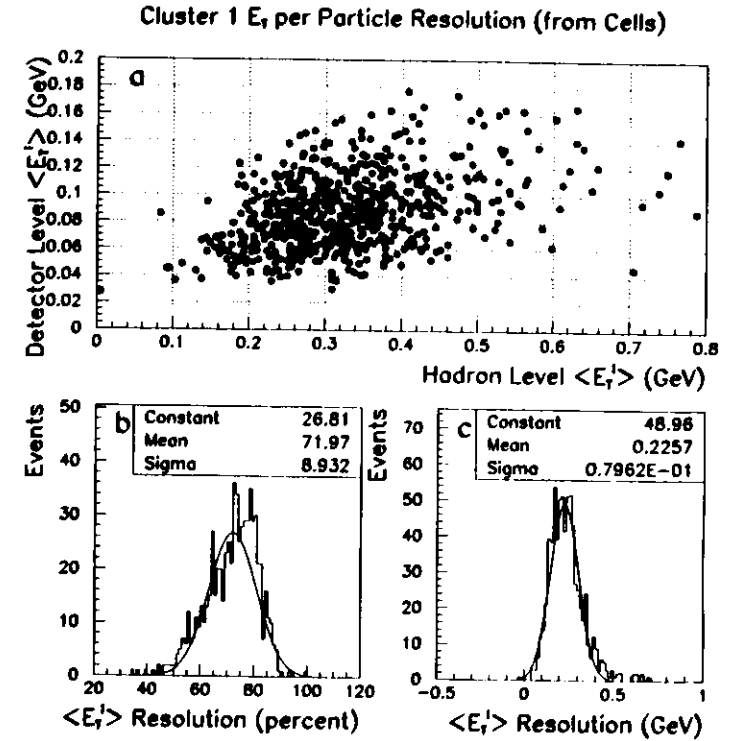


Figure A.13: The $\langle E_T^i \rangle$ resolution (calculated using calorimeter cells) of the highest p_T cluster as determined using the PYTHIA Monte Carlo simulation. (a) Correlation between the detector and hadron level $\langle E_T^i \rangle$. (b) $\langle E_T^i \rangle$ resolution in percent. (c) Absolute $\langle E_T^i \rangle$ resolution in GeV. The constant, mean and sigma in (b) and (c) are determined from the fit.

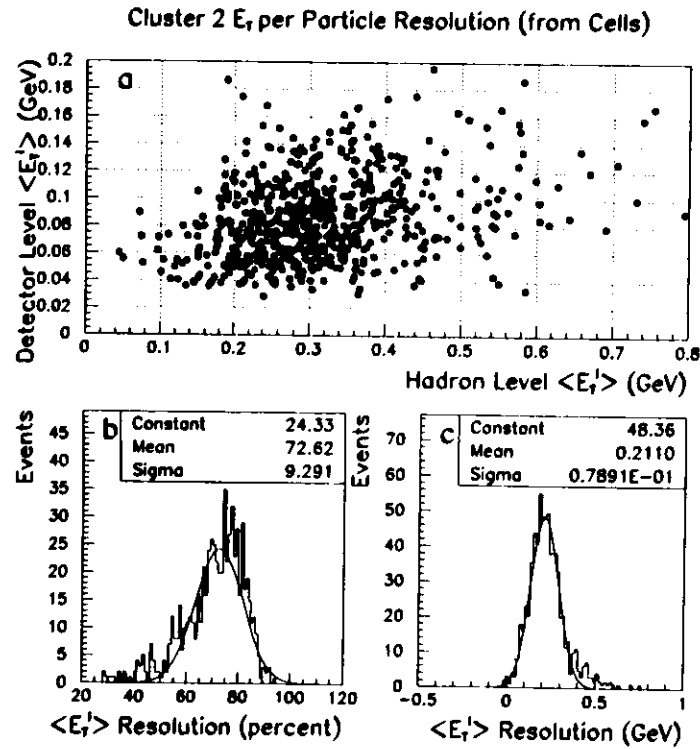


Figure A.14: The $\langle E_T \rangle$ resolution (calculated using calorimeter cells) of the second highest p_T cluster as determined using the PYTHIA Monte Carlo simulation. (a) Correlation between the detector and hadron level $\langle E_T \rangle$. (b) $\langle E_T \rangle$ resolution in percent. (c) Absolute $\langle E_T \rangle$ resolution in GeV. The constant, mean and sigma in (b) and (c) are determined from the fit.

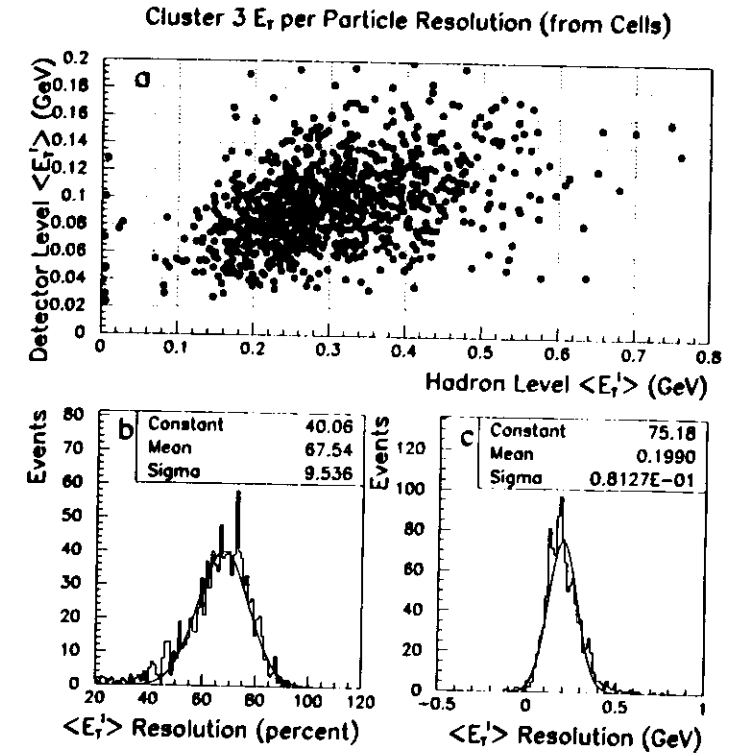


Figure A.15: The $\langle E_T \rangle$ resolution (calculated using calorimeter cells) of the photon remnant as determined using the PYTHIA Monte Carlo simulation. (a) Correlation between the detector and hadron level $\langle E_T \rangle$. (b) $\langle E_T \rangle$ resolution in percent. (c) Absolute $\langle E_T \rangle$ resolution in GeV. The constant, mean and sigma in (b) and (c) are determined from the fit.

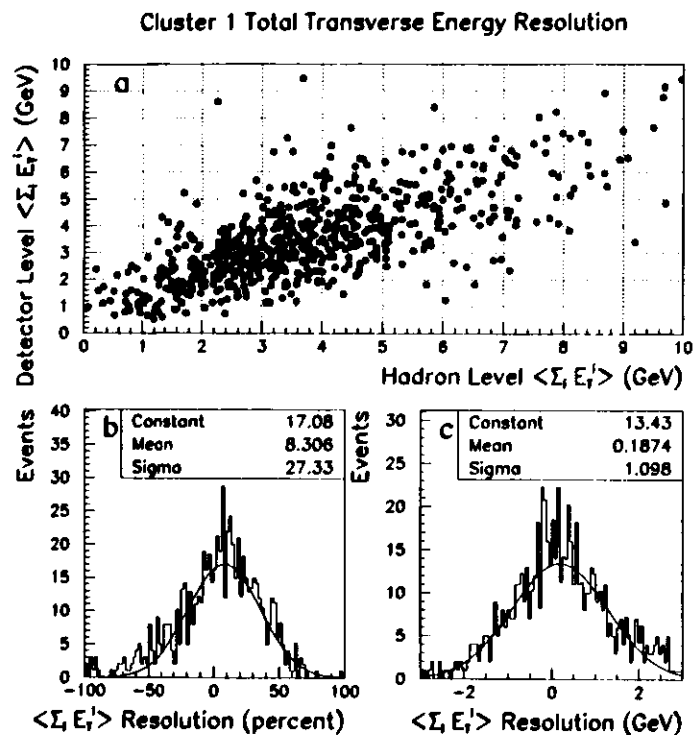


Figure A.16: The $\Sigma_i E_{T,i}$ resolution of the highest p_T cluster as determined using the PYTHIA Monte Carlo simulation. (a) Correlation between the detector and hadron level $\Sigma_i E_{T,i}$. (b) $\Sigma_i E_{T,i}$ resolution in percent. (c) Absolute $\Sigma_i E_{T,i}$ resolution in GeV. The constant, mean and sigma in (b) and (c) are determined from the fit.

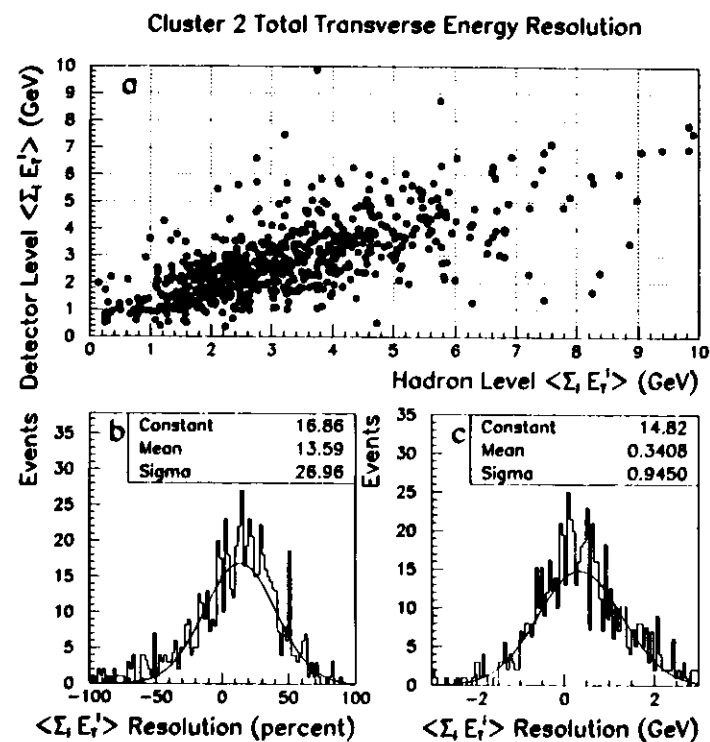


Figure A.17: The $\Sigma_i E_{T,i}$ resolution of the second highest p_T cluster as determined using the PYTHIA Monte Carlo simulation. (a) Correlation between the detector and hadron level $\Sigma_i E_{T,i}$. (b) $\Sigma_i E_{T,i}$ resolution in percent. (c) Absolute $\Sigma_i E_{T,i}$ resolution in GeV. The constant, mean and sigma in (b) and (c) are determined from the fit.

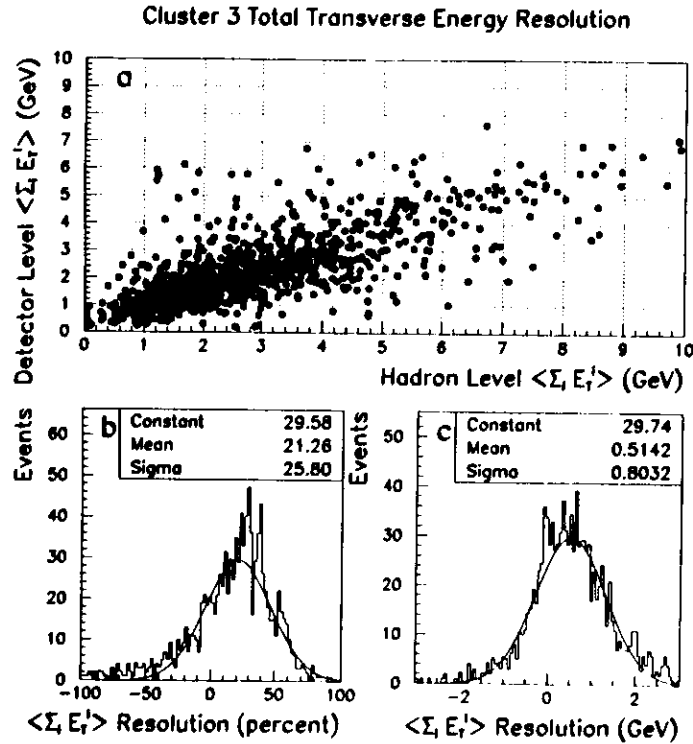


Figure A.18: The $\Sigma_i E_{T_i}$ resolution of the photon remnant as determined using the PYTHIA Monte Carlo simulation. (a) Correlation between the detector and hadron level $\Sigma_i E_{T_i}$. (b) $\Sigma_i E_{T_i}$ resolution in percent. (c) Absolute $\Sigma_i E_{T_i}$ resolution in GeV. The constant, mean and sigma in (b) and (c) are determined from the fit.

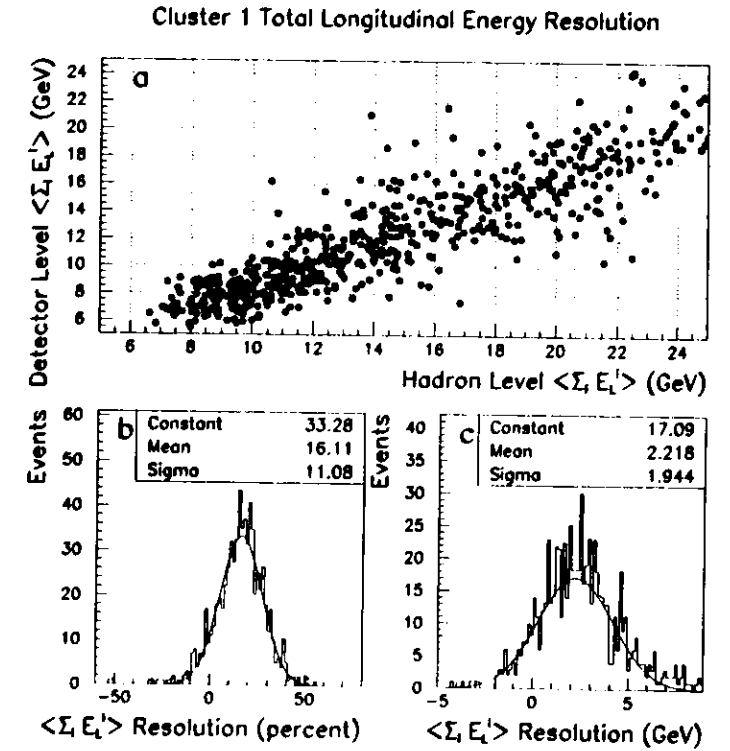


Figure A.19: The $\Sigma_i E_{L_i}$ resolution of the highest p_T cluster as determined using the PYTHIA Monte Carlo simulation. (a) Correlation between the detector and hadron level $\Sigma_i E_{L_i}$. (b) $\Sigma_i E_{L_i}$ resolution in percent. (c) Absolute $\Sigma_i E_{L_i}$ resolution in GeV. The constant, mean and sigma in (b) and (c) are determined from the fit.

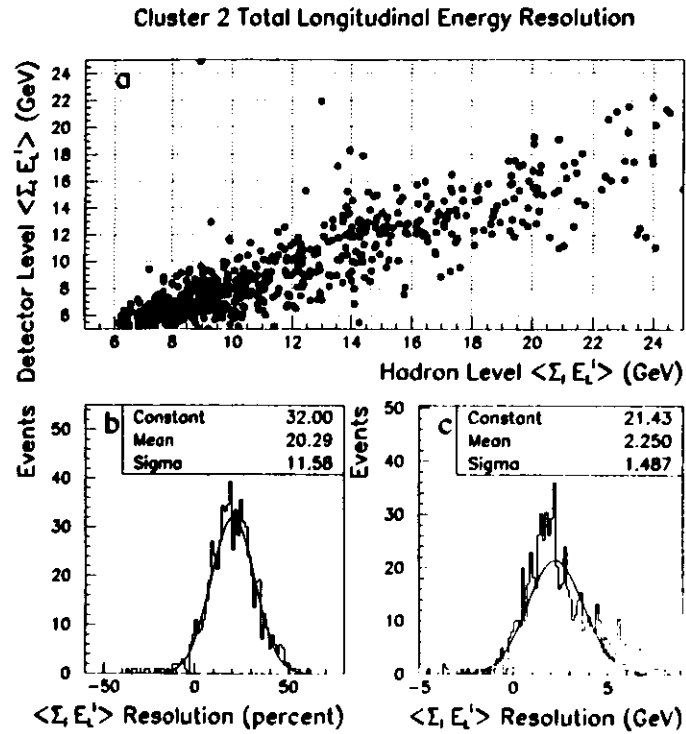


Figure A.20: The $\Sigma_i E_L^i$ resolution of the second highest p_T cluster as determined using the PYTHIA Monte Carlo simulation. (a) Correlation between the detector and hadron level $\Sigma_i E_L^i$. (b) $\Sigma_i E_L^i$ resolution in percent. (c) Absolute $\Sigma_i E_L^i$ resolution in GeV. The constant, mean and sigma in (b) and (c) are determined from the fit.

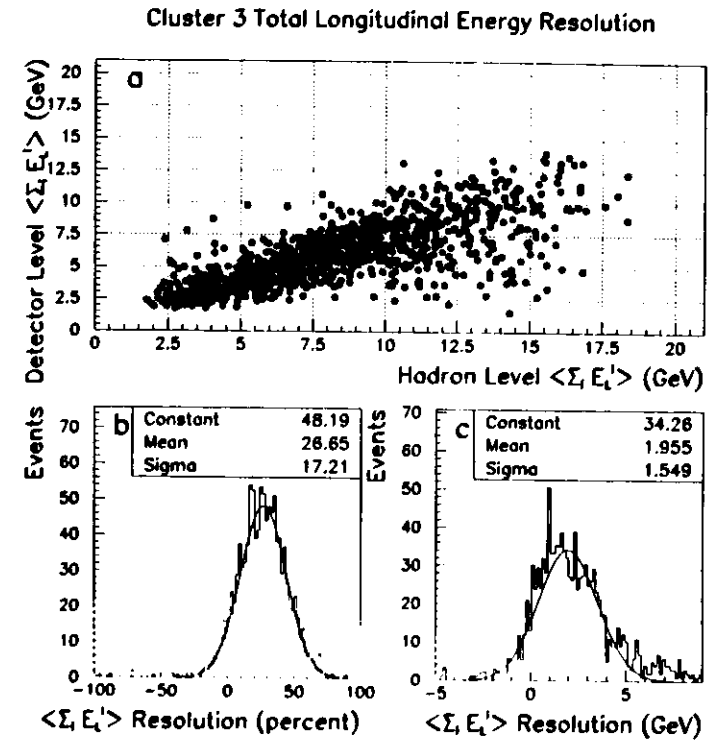


Figure A.21: The $\Sigma_i E_L^i$ resolution of the photon remnant as determined using the PYTHIA Monte Carlo simulation. (a) Correlation between the detector and hadron level $\Sigma_i E_L^i$. (b) $\Sigma_i E_L^i$ resolution in percent. (c) Absolute $\Sigma_i E_L^i$ resolution in GeV. The constant, mean and sigma in (b) and (c) are determined from the fit.

A.2 HERWIG

All of the figures listed above for the PYTHIA Monte Carlo simulation have been reproduced using the HERWIG Monte Carlo generator (Figs. A.22-A.43). All of the measurement resolutions and shifts are comparable to the results obtained using the PYTHIA Monte Carlo simulation.

Figures A.22-A.24 show the resolution of the pseudorapidity measurement. The pseudorapidity resolution is excellent for the two high p_T clusters. For the photon remnant, the pseudorapidity resolution is best near $\eta_3 = -1$, and becomes worse as the jet axis of the photon remnant gets closer and closer to the RCAL beam pipe. This behavior is the same as was observed for the PYTHIA Monte Carlo simulation.

Figures A.25-A.27 show the resolution of the transverse momentum measurement for all three clusters. The correlation between the detector level and hadron level transverse momentum is good, although not as good as for the pseudorapidity. In Fig. A.6b, a long tail toward negative values was shown. This behavior is also reproduced in the HERWIG Monte Carlo simulation (Fig. A.27b).

The energy resolutions for clusters 1, 2 and 3 are shown in Figs. A.28, A.29 and A.30 respectively. The resolution in $y_{J,B}$ is given in Fig. A.31. The resolution and systematic shifts for these figures is also compatible with the results which were obtained using the PYTHIA Monte Carlo simulation.

Figures A.32, A.33 and A.34 show the correlation between the transverse energy per island and the transverse energy per particle. As for PYTHIA, the resolution is rather poor, but the systematic shift from the detector to

the hadron level is small. Figures. A.35, A.36 and A.37 show the correlation between the transverse energy per cell and the transverse energy per particle. These results are also consistent with those obtained using PYTHIA.

Figures A.38, A.39 and A.40 show the measurement resolution of the total transverse energy with respect to the cluster axis, and Figs. A.41, A.42 and A.43 show the measurement resolution of the total longitudinal energy with respect to the cluster axis. Again, the results are consistent with PYTHIA.

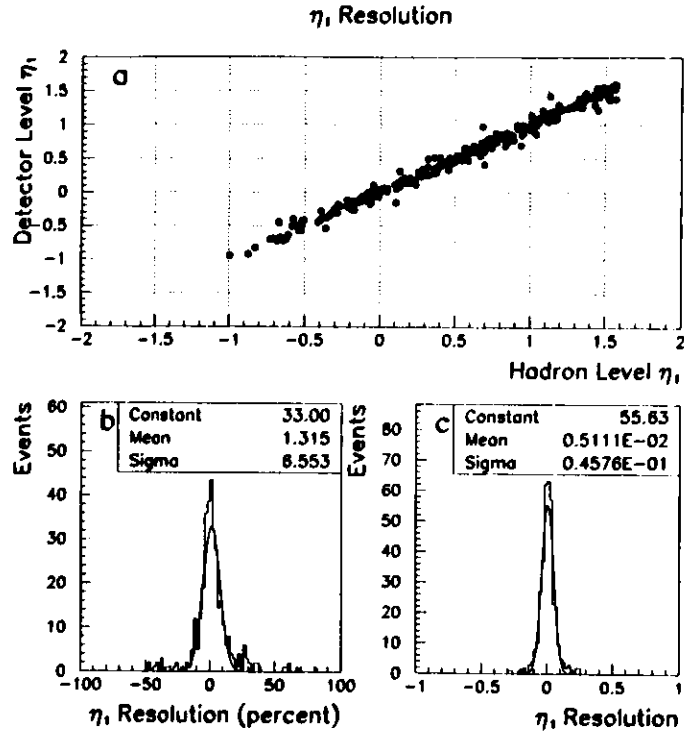


Figure A.22: Pseudorapidity resolution of the highest p_T cluster as determined using the HERWIG Monte Carlo simulation. (a) Correlation between the detector and hadron level pseudorapidity. (b) Pseudorapidity resolution in percent. (c) Absolute pseudorapidity resolution. The constant, mean and sigma in (b) and (c) are determined from the fit.

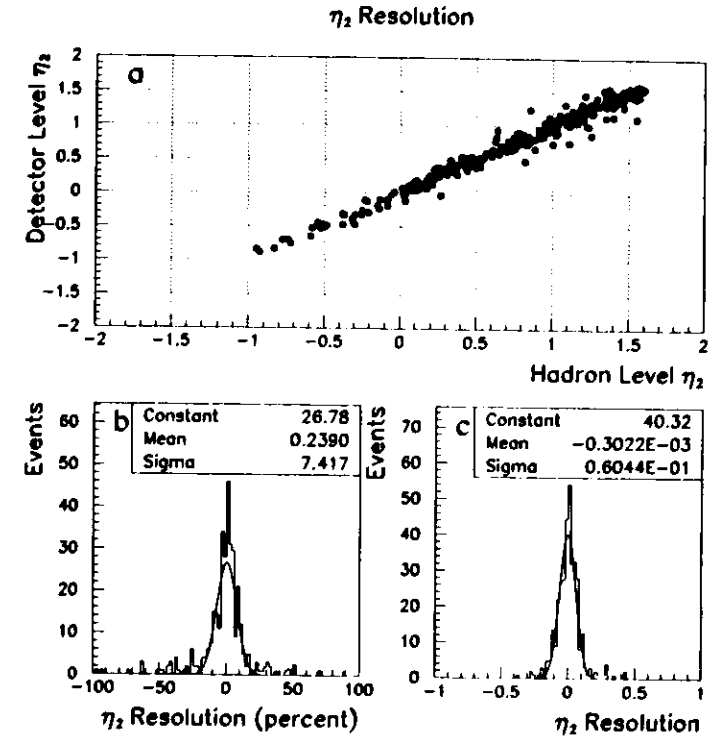


Figure A.23: Pseudorapidity resolution of the second highest p_T cluster as determined using the HERWIG Monte Carlo simulation. (a) Correlation between the detector and hadron level pseudorapidity. (b) Pseudorapidity resolution in percent. (c) Absolute pseudorapidity resolution. The constant, mean and sigma in (b) and (c) are determined from the fit.

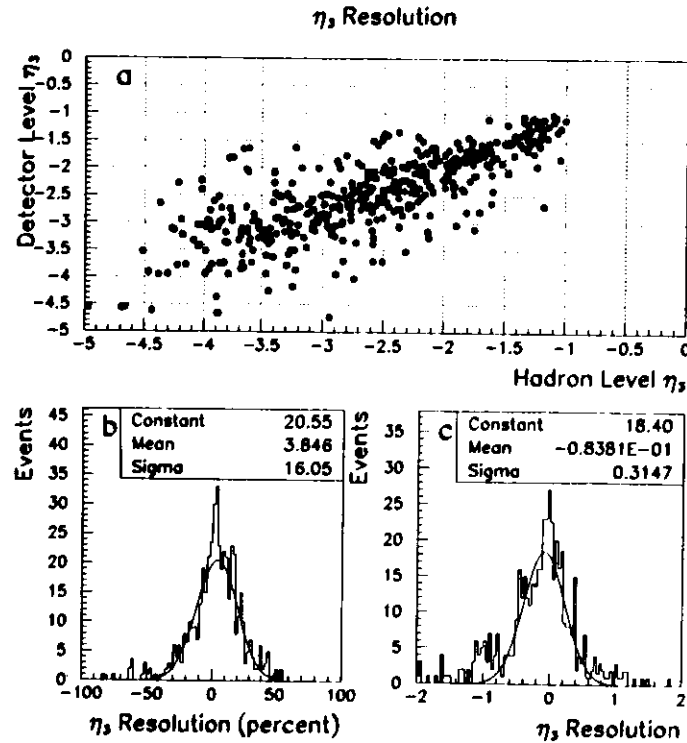


Figure A.21: Pseudorapidity resolution of the photon remnant as determined using the HERWIG Monte Carlo simulation. (a) Correlation between the detector and hadron level pseudorapidity. (b) Pseudorapidity resolution in percent. (c) Absolute pseudorapidity resolution. The constant, mean and sigma in (b) and (c) are determined from the fit.

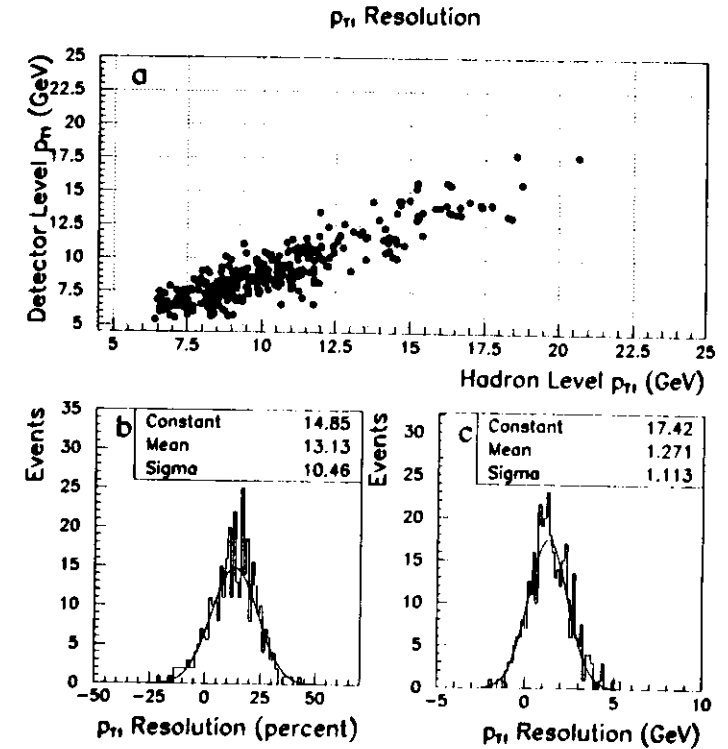


Figure A.25: Transverse momentum resolution of the highest p_T cluster as determined using the HERWIG Monte Carlo simulation. (a) Correlation between the detector and hadron level transverse momentum. (b) Transverse momentum resolution in percent. (c) Absolute transverse momentum resolution in GeV. The constant, mean and sigma in (b) and (c) are determined from the fit.

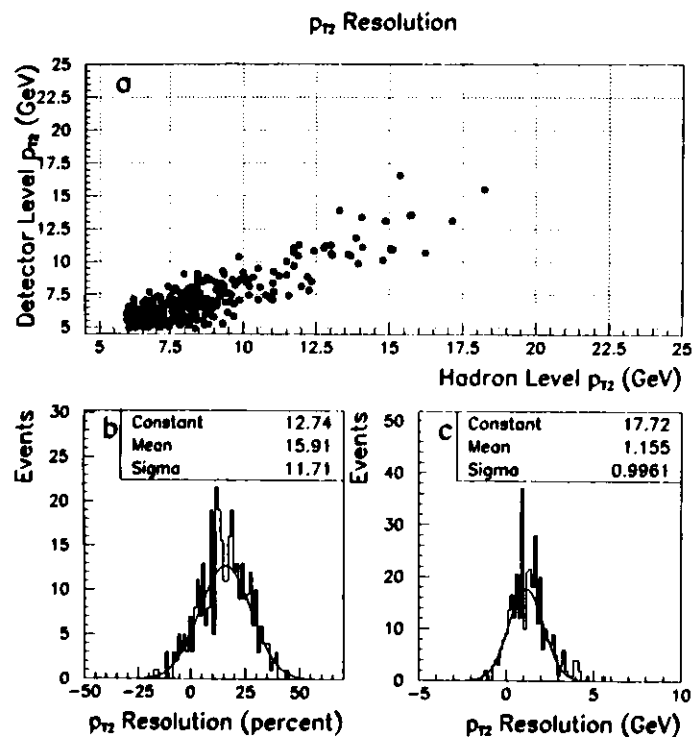


Figure A.26: Transverse momentum resolution of the second highest p_T cluster as determined using the HERWIG Monte Carlo simulation. (a) Correlation between the detector and hadron level transverse momentum. (b) Transverse momentum resolution in percent. (c) Absolute transverse momentum resolution in GeV. The constant, mean and sigma in (b) and (c) are determined from the fit.

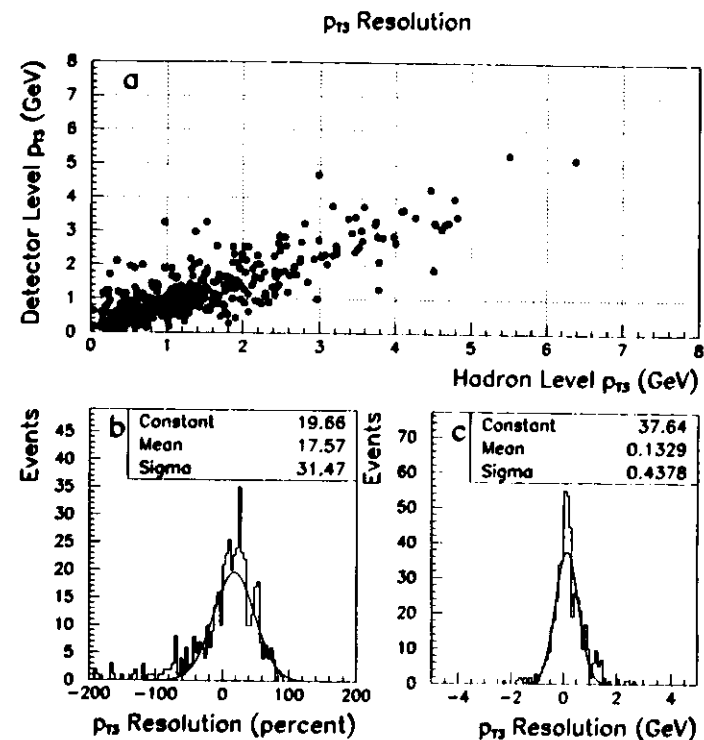


Figure A.27: Transverse momentum resolution of the photon remnant as determined using the HERWIG Monte Carlo simulation. (a) Correlation between the detector and hadron level transverse momentum. (b) Transverse momentum resolution in percent. (c) Absolute transverse momentum resolution in GeV. The constant, mean and sigma in (b) and (c) are determined from the fit.

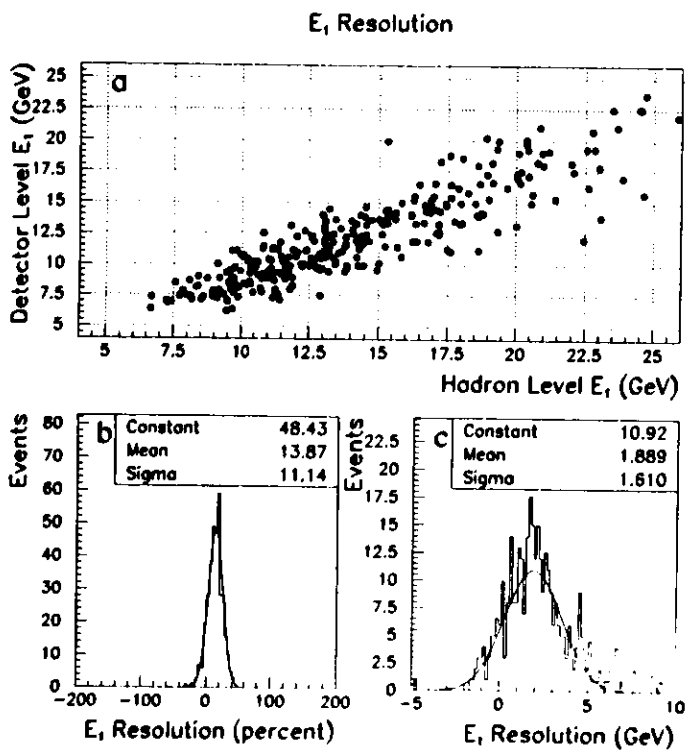


Figure A.28: Energy resolution of the highest p_T cluster as determined using the HERWIG Monte Carlo simulation. (a) Correlation between the detector and hadron level energy. (b) Energy resolution in percent. (c) Absolute energy resolution in GeV. The constant, mean and sigma in (b) and (c) are determined from the fit.

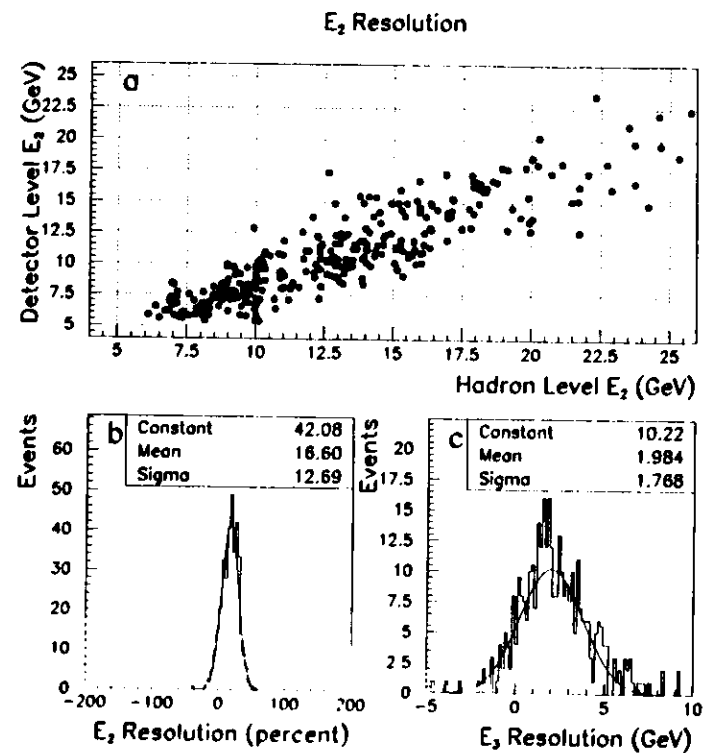


Figure A.29: Energy resolution of the second highest p_T cluster as determined using the HERWIG Monte Carlo simulation. (a) Correlation between the detector and hadron level energy. (b) Energy resolution in percent. (c) Absolute energy resolution in GeV. The constant, mean and sigma in (b) and (c) are determined from the fit.

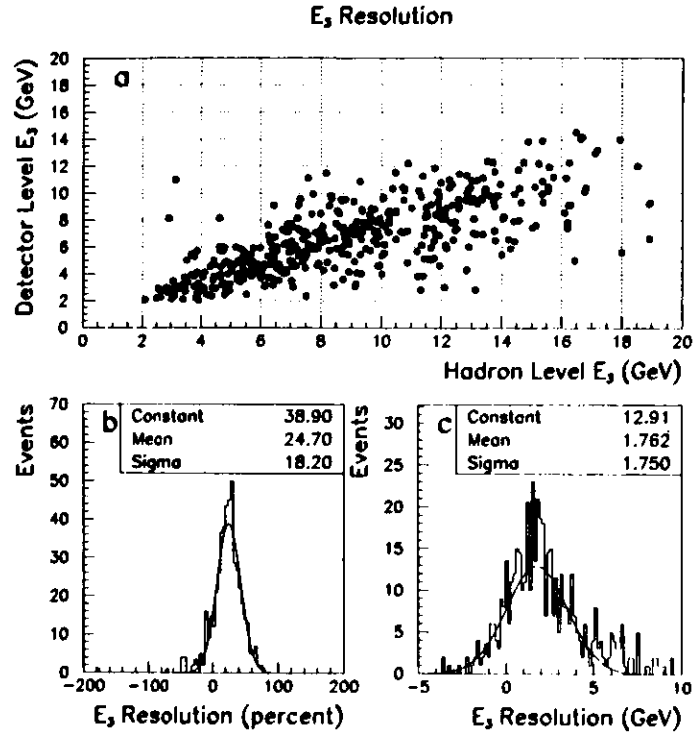


Figure A.30: Energy resolution of the photon remnant as determined using the HERWIG Monte Carlo simulation. (a) Correlation between the detector and hadron level energy. (b) Energy resolution in percent. (c) Absolute energy resolution in GeV. The constant, mean and sigma in (b) and (c) are determined from the fit.

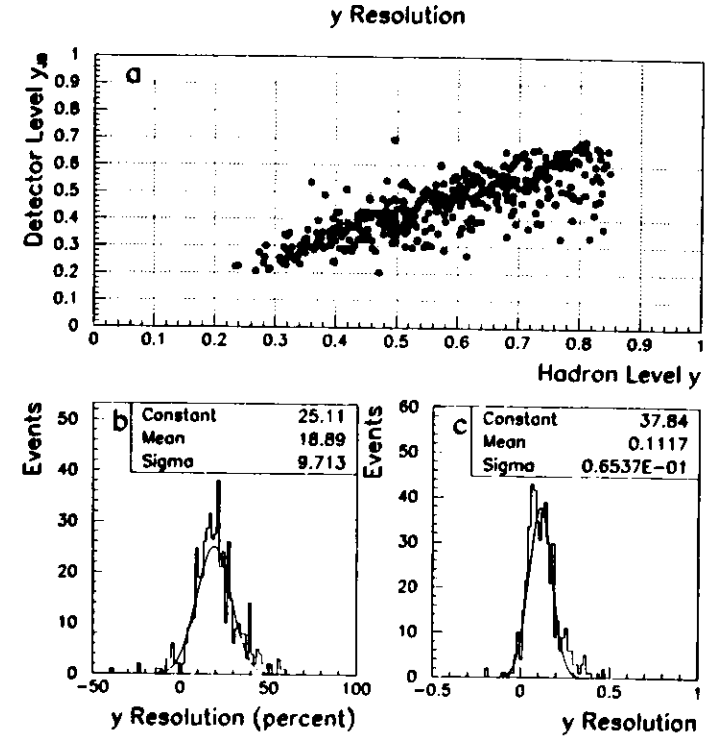


Figure A.31: The y resolution as determined using the HERWIG Monte Carlo simulation. (a) Correlation between the detector and hadron level y . (b) y resolution in percent. (c) Absolute y resolution. The constant, mean and sigma in (b) and (c) are determined from the fit.

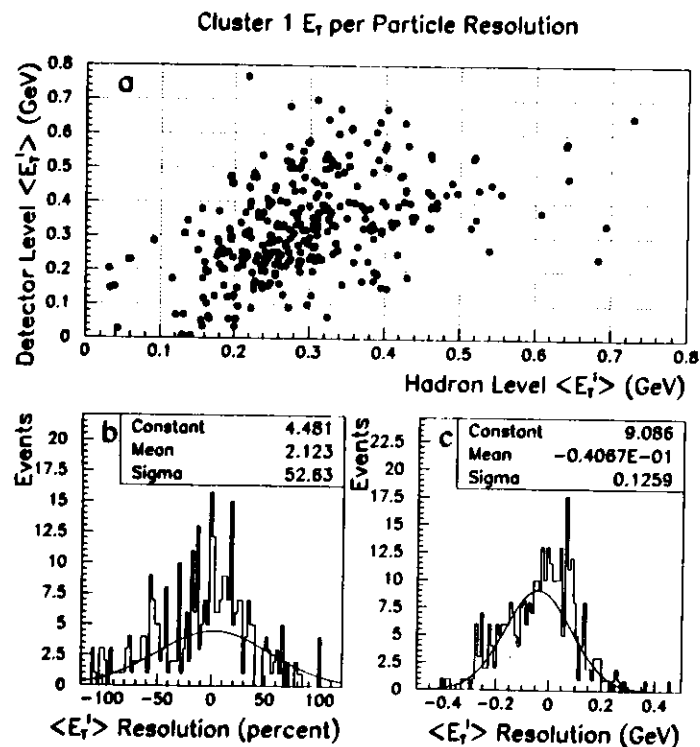


Figure A.32: The $\langle E_T \rangle$ resolution (calculated using calorimeter islands) of the highest p_T cluster as determined using the HERWIG Monte Carlo simulation. (a) Correlation between the detector and hadron level $\langle E_T \rangle$. (b) $\langle E_T \rangle$ resolution in percent. (c) Absolute $\langle E_T \rangle$ resolution in GeV. The constant, mean and sigma in (b) and (c) are determined from the fit.

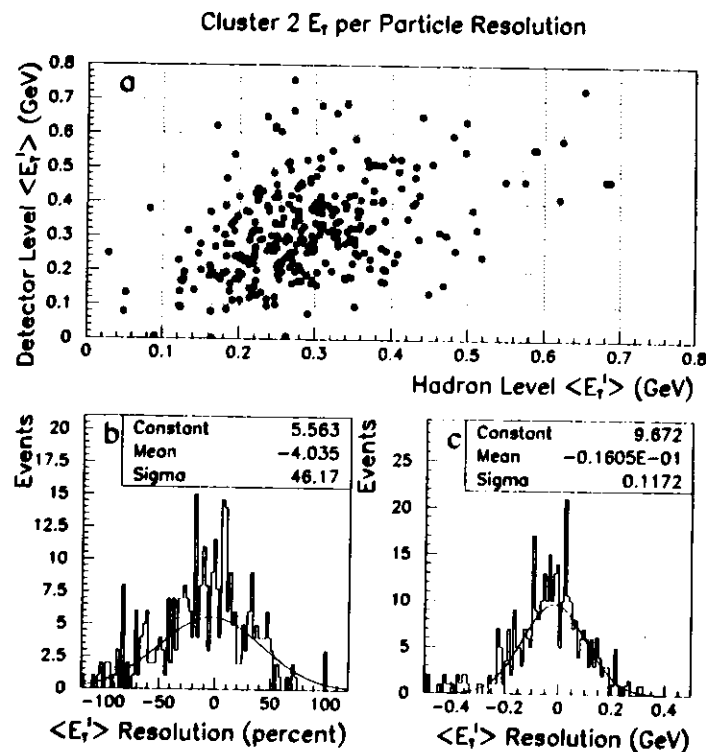


Figure A.33: The $\langle E_T \rangle$ resolution (calculated using calorimeter islands) of the second highest p_T cluster as determined using the HERWIG Monte Carlo simulation. (a) Correlation between the detector and hadron level $\langle E_T \rangle$. (b) $\langle E_T \rangle$ resolution in percent. (c) Absolute $\langle E_T \rangle$ resolution in GeV. The constant, mean and sigma in (b) and (c) are determined from the fit.

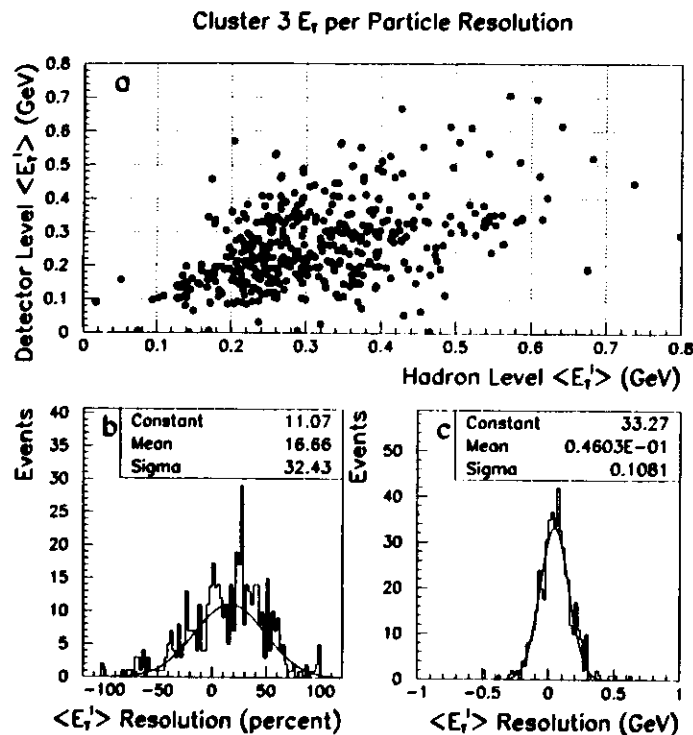


Figure A.34: The $\langle E_T \rangle$ resolution (calculated using calorimeter islands) of the photon remnant as determined using the HERWIG Monte Carlo simulation. (a) Correlation between the detector and hadron level $\langle E_T \rangle$. (b) $\langle E_T \rangle$ resolution in percent. (c) Absolute $\langle E_T \rangle$ resolution in GeV. The constant, mean and sigma in (b) and (c) are determined from the fit.

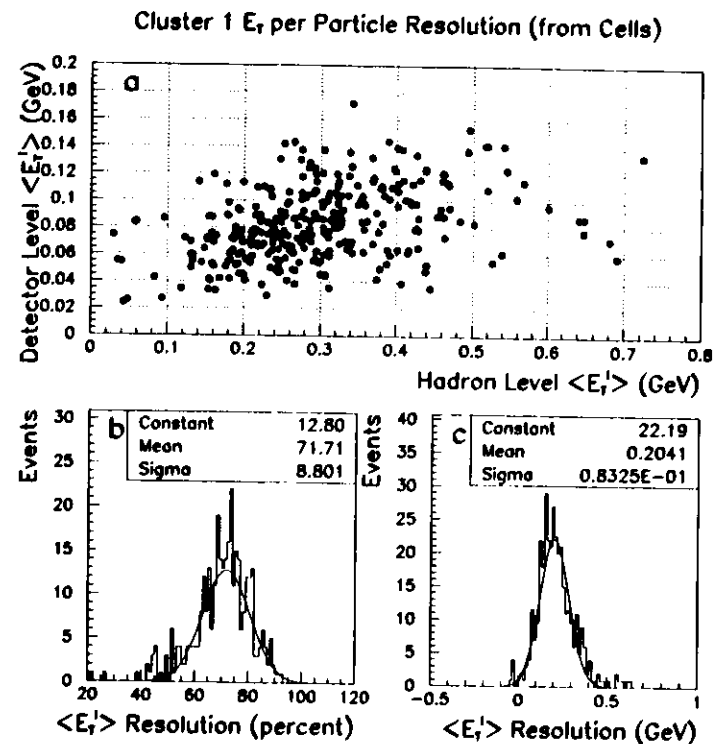


Figure A.35: The $\langle E_T \rangle$ resolution (calculated using calorimeter cells) of the highest p_T cluster as determined using the HERWIG Monte Carlo simulation. (a) Correlation between the detector and hadron level $\langle E_T \rangle$. (b) $\langle E_T \rangle$ resolution in percent. (c) Absolute $\langle E_T \rangle$ resolution in GeV. The constant, mean and sigma in (b) and (c) are determined from the fit.

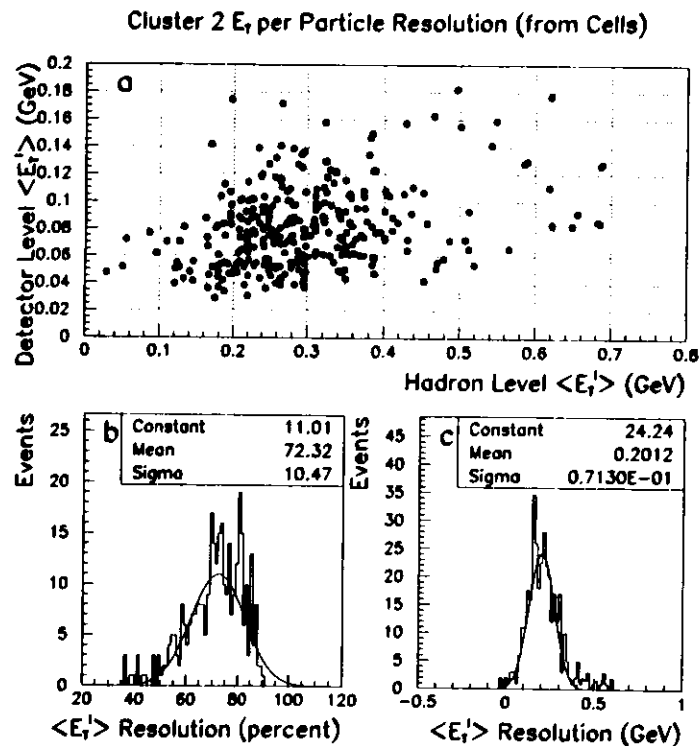


Figure A.36: The $\langle E_T^i \rangle$ resolution (calculated using calorimeter cells) of the second highest p_T cluster as determined using the HERWIG Monte Carlo simulation. (a) Correlation between the detector and hadron level $\langle E_T^i \rangle$. (b) $\langle E_T^i \rangle$ resolution in percent. (c) Absolute $\langle E_T^i \rangle$ resolution in GeV. The constant, mean and sigma in (b) and (c) are determined from the fit.

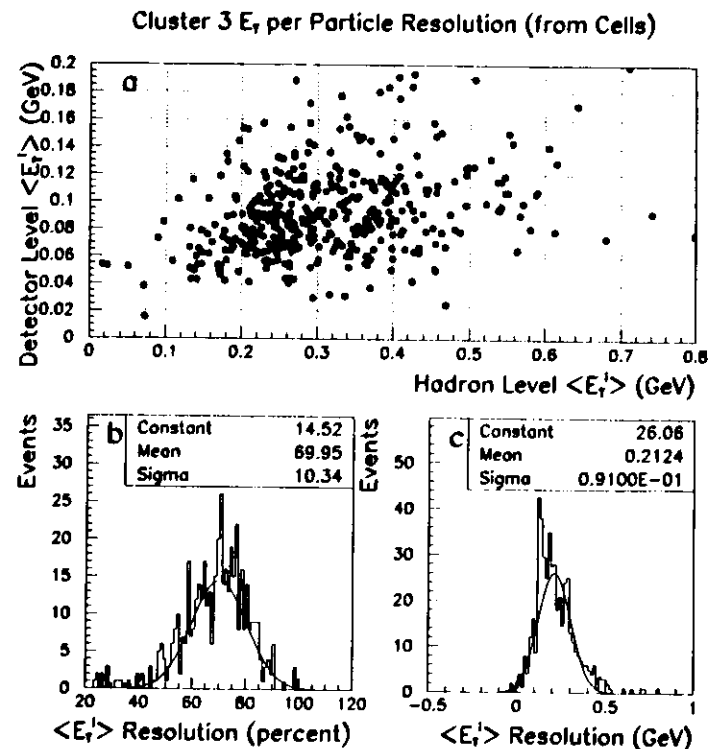


Figure A.37: The $\langle E_T^i \rangle$ resolution (calculated using calorimeter cells) of the photon remnant as determined using the HERWIG Monte Carlo simulation. (a) Correlation between the detector and hadron level $\langle E_T^i \rangle$. (b) $\langle E_T^i \rangle$ resolution in percent. (c) Absolute $\langle E_T^i \rangle$ resolution in GeV. The constant, mean and sigma in (b) and (c) are determined from the fit.

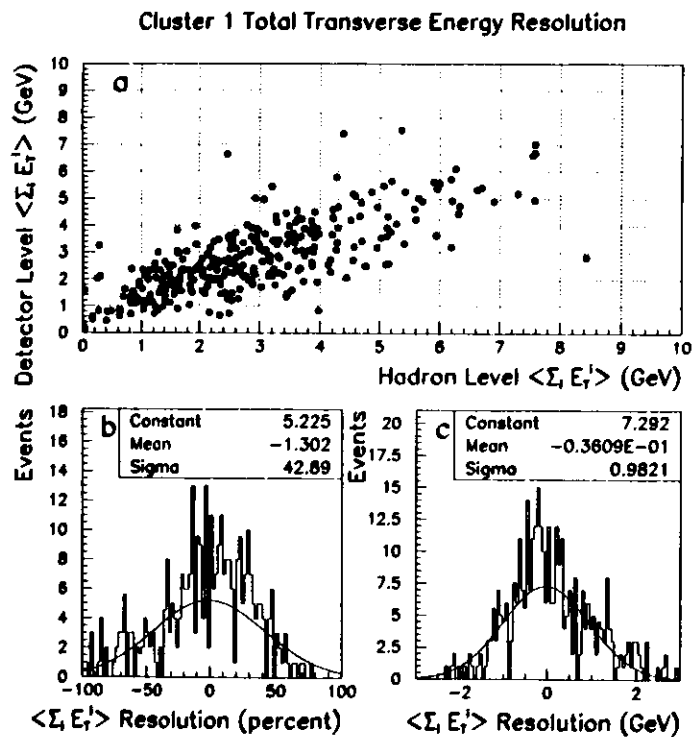


Figure A.38: The $\Sigma_i E_T^i$ resolution of the highest p_T cluster as determined using the HERWIG Monte Carlo simulation. (a) Correlation between the detector and hadron level $\Sigma_i E_T^i$. (b) $\Sigma_i E_T^i$ resolution in percent. (c) Absolute $\Sigma_i E_T^i$ resolution in GeV. The constant, mean and sigma in (b) and (c) are determined from the fit.

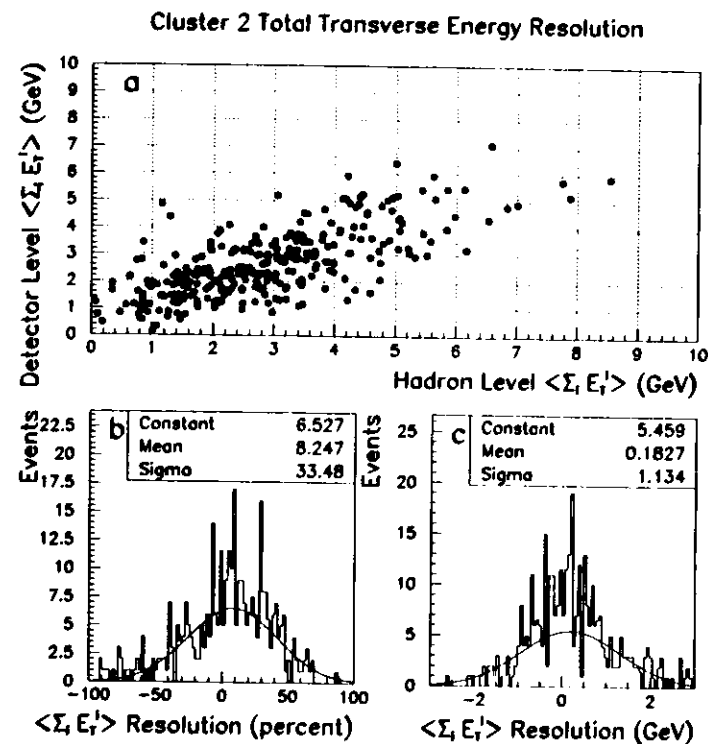


Figure A.39: The $\Sigma_i E_T^i$ resolution of the second highest p_T cluster as determined using the HERWIG Monte Carlo simulation. (a) Correlation between the detector and hadron level $\Sigma_i E_T^i$. (b) $\Sigma_i E_T^i$ resolution in percent. (c) Absolute $\Sigma_i E_T^i$ resolution in GeV. The constant, mean and sigma in (b) and (c) are determined from the fit.

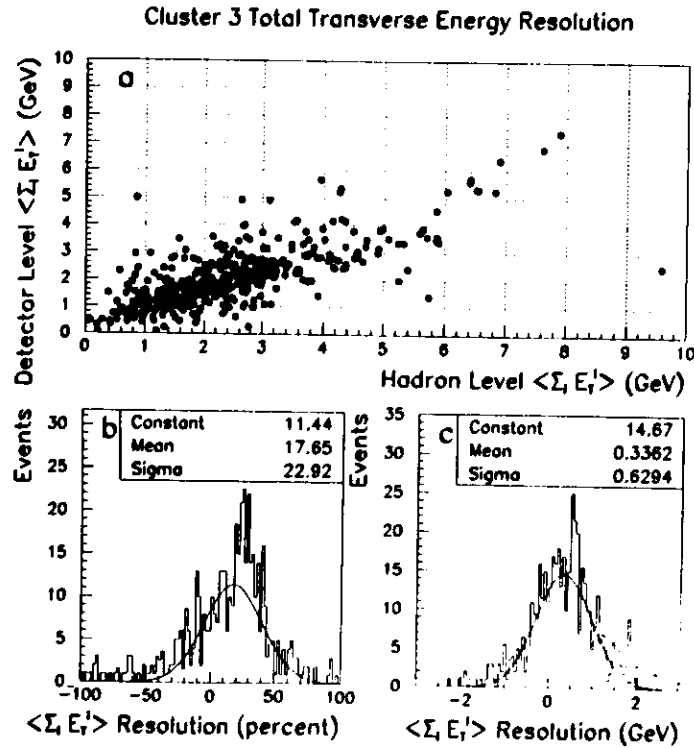


Figure A.10: The $\Sigma_T E_T'$ resolution of the photon remnant as determined using the HERWIG Monte Carlo simulation. (a) Correlation between the detector and hadron level $\Sigma_T E_T'$. (b) $\Sigma_T E_T'$ resolution in percent. (c) Absolute $\Sigma_T E_T'$ resolution in GeV. The constant, mean and sigma in (b) and (c) are determined from the fit.

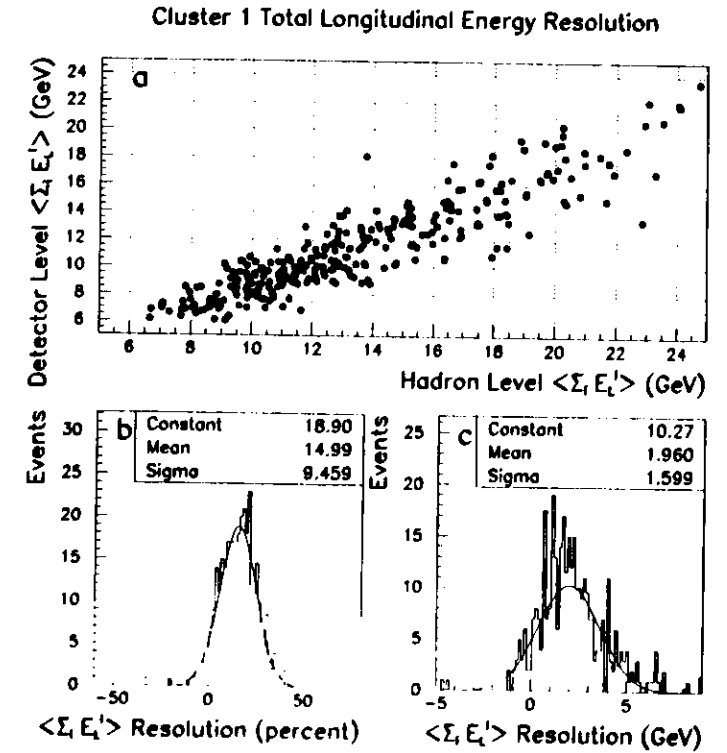


Figure A.11: The $\Sigma_L E_L'$ resolution of the highest p_T cluster as determined using the HERWIG Monte Carlo simulation. (a) Correlation between the detector and hadron level $\Sigma_L E_L'$. (b) $\Sigma_L E_L'$ resolution in percent. (c) Absolute $\Sigma_L E_L'$ resolution in GeV. The constant, mean and sigma in (b) and (c) are determined from the fit.

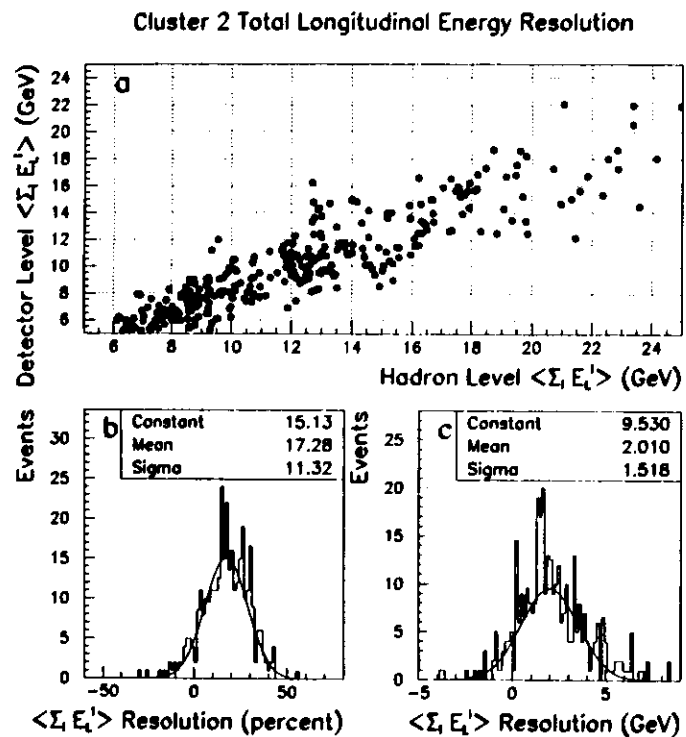


Figure A.42: The $\Sigma_i E_L^i$ resolution of the second highest p_T cluster as determined using the HERWIG Monte Carlo simulation. (a) Correlation between the detector and hadron level $\Sigma_i E_L^i$. (b) $\Sigma_i E_L^i$ resolution in percent. (c) Absolute $\Sigma_i E_L^i$ resolution in GeV. The constant, mean and sigma in (b) and (c) are determined from the fit.

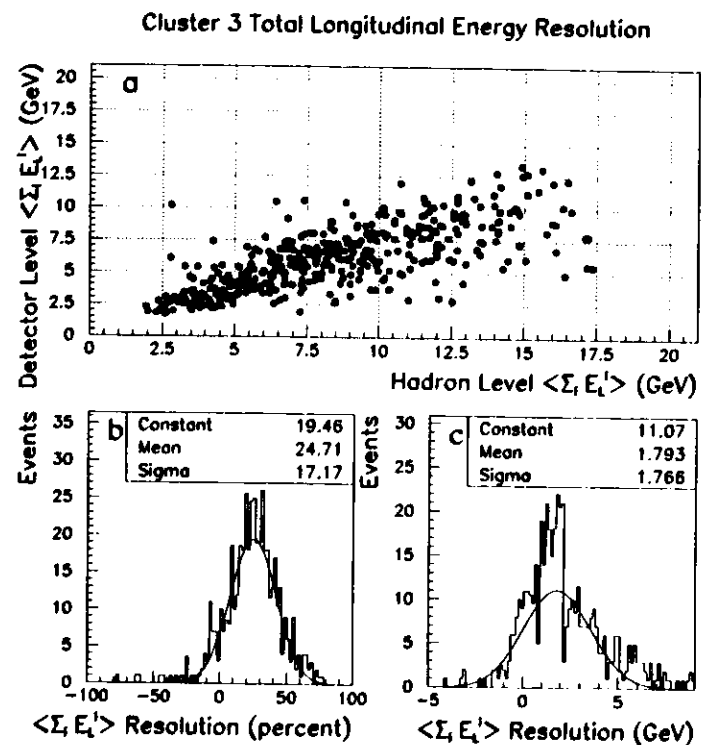


Figure A.43: The $\Sigma_i E_L^i$ resolution of the photon remnant as determined using the HERWIG Monte Carlo simulation. (a) Correlation between the detector and hadron level $\Sigma_i E_L^i$. (b) $\Sigma_i E_L^i$ resolution in percent. (c) Absolute $\Sigma_i E_L^i$ resolution in GeV. The constant, mean and sigma in (b) and (c) are determined from the fit.

References

1. ZEUS Collab., M. Derrick et al., DESY 95-083, Submitted to *Phys. Lett. B* (1995).
2. F. Halzen and A. D. Martin, *Quarks and Leptons: An introductory course in modern particle physics*, John Wiley & Sons, Inc., New York (1984).
3. J. F. Owens, *Phys. Rev. D* 21 (1980) 54;
M. Drees and F. Halzen, *Phys. Rev. Lett.* 61 (1988) 275;
M. Drees and R. M. Godbole, *Phys. Rev. D* 39 (1989) 169;
G. A. Schuler and T. Sjöstrand, *Phys. Lett. B* 300 (1993) 169.
4. J. J. Sakurai, *Phys. Rev. Lett.* 22 (1969) 981.
5. E. Witten, *Nucl. Phys. B* 120 (1977) 189.
6. ZEUS Collab., M. Derrick et al., *Phys. Lett. B* 297 (1992) 401.
7. H1 Collab., T. Ahmed et al., *Phys. Lett. B* 297 (1992) 205.
8. ZEUS Collab., M. Derrick et al., *Phys. Lett. B* 322 (1994) 287.
9. ZEUS Collab., M. Derrick et al., *Phys. Lett. B* 318 (1995) 665.
10. AMY Collab., T. Sasaki et al., *Phys. Lett. B* 252 (1990) 191;
PLUTO Collab., C. Berger et al., *Z. Phys. C* 26 (1984) 353;
PLUTO Collab., C. Berger et al., *Phys. Lett. B* 112 (1984) 111;
PLUTO Collab., C. Berger et al., *Phys. Lett. B* 119 (1984) 121;
PLUTO Collab., C. Berger et al., *Nucl. Phys. B* 281 (1987) 365;
- TASSO Collab., H. Althoff et al., *Z. Phys. C* 31 (1986) 527;
- JADE Collab., W. Bartel et al., *Z. Phys. C* 21 (1984) 231;
- TPC/2 γ Collab., D. Bintiger et al., *Phys. Rev. Lett.* 54 (1985) 763;
- TPC/2 γ Collab., H. Aihara et al., *Phys. Rev. Lett.* 58 (1987) 97;
- TPC/2 γ Collab., H. Aihara et al., *Z. Phys. C* 31 (1987) 1.
11. ZEUS Collab., The ZEUS Detector, Status Report (1993).
12. R. Brinkmann, HERA. DESY-HERA 88-03 (1988);
B. H. Wilk, HERA Status, Proceedings of the DESY Workshop 'Physics at HERA'. Ed. W. Buckmüller and G. Ingelman. Hamburg (1991) 1.
13. M. Derrick et al., *Nucl. Instr. Meth. A* 309 (1991) 77;
A. Andresen et al., *Nucl. Instr. Meth. A* 309 (1991) 101;
A. Bernstein et al., *Nucl. Instr. Meth. A* 336 (1993) 23.
14. H. Brückmann et al., *Nucl. Instr. Meth. A* 263 (1988) 136.
15. W. H. Smith et al., *Nucl. Instr. Meth. A* 355 (1995) 278.
16. C. Alvisi et al., *Nucl. Instr. Meth. A* 305 (1991) 30.
17. B. Foster et al., *Nucl. Phys. B, Proc. Suppl.* B32 (1993) 181.
18. J. Andruszków et al., DESY 92-066 (1992).
19. ZEUS Note 92-072 (1992).
20. W. Schott et al., ZEUS Note 93-002 (1993).
21. L. Wiggers, DESY 92-150.

22. H. U. Bengtsson and T. Sjöstrand, *Comp. Phys. Comm.*, 16 (1987) 43; T. Sjöstrand, CERN-TH 6488/92.
23. C. F. v. Wiizäcker, *Z. Phys.* 88 (1939) 612;
E. J. Williams, *Phys. Rev.* 45 (1934) 729.
24. B. Andersson, G. Gustafson, G. Ingelman and T. Sjöstrand, *Comp. Phys. Rep.*, 97 (1983) 31.
25. M. Glück, E. Reya and A. Vogt, *Phys. Rev. D* 46 (1992) 1973.
26. A. D. Martin, W. J. Stirling and R. G. Roberts, *Phys. Rev. D* 47 (1993) 867.
27. H. Abramowicz, K. Charchula and A. Levy, *Phys. Lett.* B269 (1991) 458.
28. G. Marchesini et al., *Comp. Phys. Comm.* 67 (1992) 465.
29. L. Köpke, ZEUS Note 93-006 (1993).
P. de Jong, ZEUS Note 92-019 (1992).
30. R. Brun et al., GEANT3.13, CERN DD/EE/84-1 (1987)
31. H. Uijterwaal and R. van De Woulenberg, ZGANA 1.7, Analysis code for the ZG31311 Monte Carlo. Documentation.
32. G. A. Schuler and T. Sjöstrand, preprint CERN-TH 7193/91.
33. J. Chýla, *Phys. Lett.* B320 (1991) 186.
34. M. Drees, Proceedings of the Aspen conference on Multiparticle Dynamics, Aspen, Colorado 1993 p. 110 and preprint MAD/PH/797.

35. ZEUS Collab., M. Derrick et al., *Phys. Lett.* B342 (1995) 417.
36. ZEUS Collab., M. Derrick et al., EPS 0380, Int. Europhys. Conf. on HEP, Brussels, July 27 - Aug. 2, (1995).
37. ZEUS Collab., M. Derrick et al., *Phys. Lett.* B316 (1993) 412.
38. F. Jacquet and A. Blondel, Proc. of the Study for an *ep* Facility for Europe, ed. U. Amaldi, DESY 79/48 (1979) 391.
39. S. Catani et al., *Nucl. Phys.* B406 (1993) 187;
S. Catani, Yu.L. Dokshitzer and B. R. Webber, *Phys. Lett.* B285 (1992) 291.
40. UA1 Collab., G. Arnison et al., *Phys. Lett.* B123 (1983) 115;
J. E. Huth et al., FERMILAB-Conf-90-249-E.
41. G. D'Agostini, DESY 94-099 (1994).
42. L. Lyons, *Statistics for Nuclear and Particle Physicists*, Cambridge University Press, Cambridge, (1986).
43. B. Behrens et al. ZEUS Note 95-091 (1995).
44. ZEUS Collab., PHANTOM - Physics Analysis Techniques, Operations and Methods - Collection of Subroutines for Data Analysis.
45. A. Caldwell et al., ZEUS Note 94-051 (1994).
46. J. Ng, ZEUS Note 95-037 (1995).
47. J. M. Butterworth et al., ZEUS Note 95-010 (1995).